A microstructural and micromechanical investigation into shear dynamics during volcanic edifice collapse on Ascension Island: An experimental approach

HONOR ELIZABETH JAMES

A microstructural and micromechanical investigation into shear dynamics during volcanic edifice collapse on Ascension Island: An experimental approach

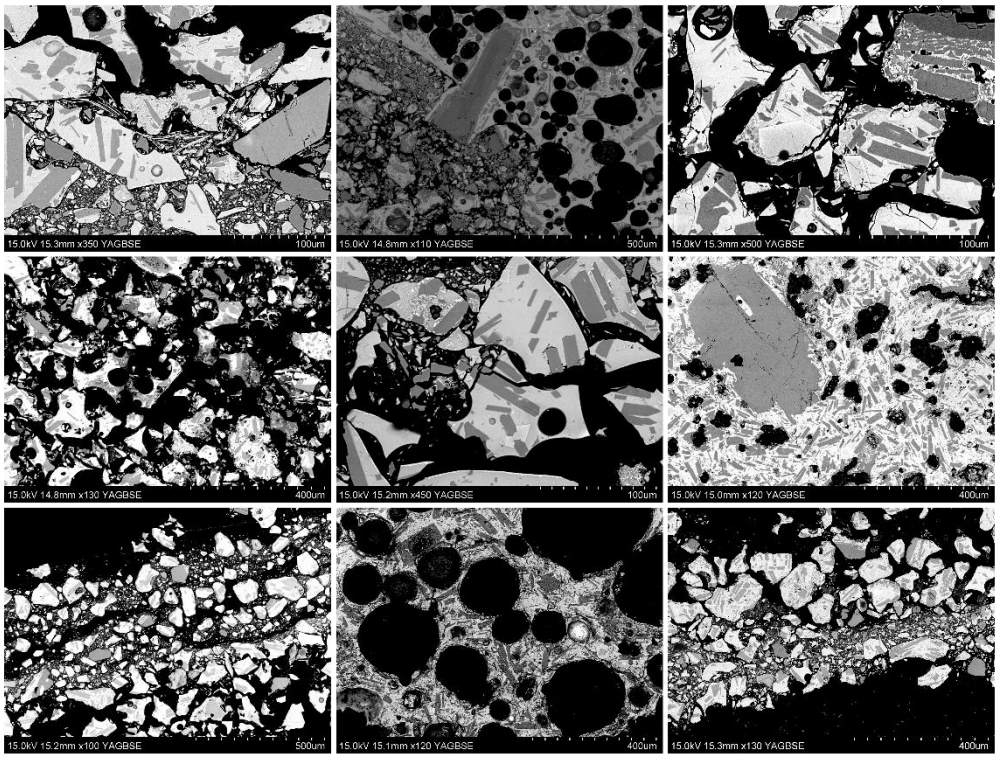

Honor E. James

Thesis submitted in fulfilment of the degree of MSc by Research (MScR) in Earth Science

Department of Earth Science

Durham University

2021-22

Abstract

During gravitational collapse flows, shear forces are expressed through localised or diffuse, brittle or ductile strain. Understanding material responses to shear within gravitational collapse flows can be achieved through microstructural and micromechanical investigation using established experimental techniques. This thesis investigates a shear zone generated during a volcanic debris avalanche following the collapse of a scoria cone on Green Mountain, Ascension Island through (1) quantitative data on microstructural evolution within the shear zone through Scanning Electron Microscope imaging, and (2) experimental work using rotary shear apparatus to constrain the mechanical behaviour of the material under stress, and its influence on internal microstructure. Microstructural analysis of the Green Mountain shear zone reveals a decrease in grain size and porosity, as well as clast morphology evolution toward the principal slip zone in the centremost region. Such observations are mirrored in experimental shear zones presented herein. Mechanical data provide evidence that material saturation promotes dynamic velocity weakening behaviour at seismic velocities. Based on observations and evidence presented in this thesis, a model for shear dynamics during the Green Mountain volcanic debris advance is proposed. It is suggested that (1) a brittle cataclastic regime dominated within the shear zone, resulting in the microstructural characteristics observed and (2) processes to facilitate velocity weakening behaviour may include pore pressure fluidisation and nanoparticle lubrication. Overall, this work contributes to the understanding of shear localisation, internal microstructure, and facilitators of mechanical behaviour within the Green Mountain volcanic debris avalanche deposit. Application of these findings to other deposits and associated shear zones may help to better constrain collapse behaviour and to mitigate associated risks.

Contents

List of Tables

List of Figures

List of Abbreviations

PSZ *Principal Slip Zone*

30,32,38,44,55,64,68,73,75,76,82,83,84,85, 86,92,94,95,96,98,99,100,103,104,108

GMSZ *Green Mountain Shear Zone*

38,39,44,55,57,80,86,94,95,96,101, 103,104,105,106,108,109,110

LHVR *Low to High Velocity Rotary shearing equipment*

38, 43,45,46,51,53,95,108

LG *Laser Granulometer*

52,53,54,95,96

Statement of Copyright

Acknowledgements

My greatest thanks go to Dr Richard Brown for supervising this project and offering guidance, support, and humour along the way. Thanks also to Prof. Nic De Paola and Dr Katie Preece for co-supervising this project and making sure I had all the information and resources I needed. Thank you to Dr Fabian Wadsworth and Dr Kevin Burton for reviewing this project and offering support and constructive criticism.

Thank you to Mr Fadul Dawood for assistance with running experiments and processing data, to Mr Leon Bowen for training on the SEM, to Mr Neil Tunstall for help with using the Laser Granulometer, and to Mr Ian Chaplain in the Rock Sectioning lab for processing my samples.

Thank you to Gus Semanchik, Janina Gilliies, Bex Robertson and Ally Sweeney for solution-orientated thinking, geological input, friendship and fantastic craic throughout the year. Thank you also to Jeremy Teale, Lucy Jackson, Sean Ruffell, Silas Welch, Ipshita Chatterji & all the PGRs along the way.

I would like to extend my sincere gratitude to the donors of the Stephen Mills Scholarship for funding this degree. This has been a significant financial help and is deeply appreciated.

Thank you lastly to my parents, friends, the rest of the Durham University Earth Science Department and my network at Ustinov College. This would all have been significantly less fun without you.

Chapter I: Introduction

This thesis examines a shear zone situated within a volcanic debris avalanche deposit on Ascension Island. Detailed examination of the shear zone using Scanning Electron Microscope imagery and image analysis tools provide quantitative evidence of microstructural variation with depth through the shear zone. The facilitators of these microstructural changes are investigated through experimental work designed to constrain the mechanical behaviour of the collapsed volcanic material. Mechanical and microstructural data from these experiments are applied to the natural shear zone and the consequences for volcanic debris avalanche dynamics. Ultimately, this is to better understand the influence of shear dynamics acting within the Ascension Island debris avalanche.

1.1 Volcanic Collapse Deposits

1.1.1 Hazards

Volcanic edifice collapses pose significant risk to life, property and infrastructure. Recent lateral collapses such as that of Kilauea, US (Chen et al. 2019) and Etna, Italy (Bonforte et al., 2018) have resulted in loss of life and destruction. Several major cities are situated at the foot of volcanoes; Tokyo sits near the foot of Mount Fuji, Seattle by Mount Rainier, and Naples by Mount Vesuvius, for instance. As urban bases continue to expand, the number of people exposed to the risk of volcanic edifice collapse related disasters will continue to rise (Chester et al., 2000). Secondary hazards posed by volcanic edifice collapse include tsunamis, especially on volcanic islands (Aucker et al., 2013; van Wyk de Vries, 2015), such as the 2018 tsunamigenic collapse of Anak Krakatau, Indonesia (Williams et al, 2019).

Following the lateral collapse of Mt. St. Helens in 1980, which displaced 2.5km^3 of material during a volcanic debris avalanche (Glicken, 1996) and highlighted the dangers of such collapses, research into volcanic edifice failure has surged (e.g. Moore et al; 1989; Scott et al., 2001; Mitchell, 2003; Sosio et al., 2012; Perinotto et al., 2015; Roverato et al., 2015 Dufresne et al., 2020). To build resilience, and to mitigate and manage associated risks, we must first understand the dynamics and mechanics driving volcanic collapse (Capra, 2006).

1.1.2 Types of Volcanic Collapse Deposits

Volcanic edifice collapses are defined herein as the gravity-driven failure of pre-existing volcanic flank material, and therefore does not incorporate flows such as pyroclastic density currents, which are composed of new erupted material.

Stratovolcano flank terranes are often composed of layers of unconsolidated tephra deposits which can be readily mobilised, making flanks prone to collapse (Scott et al., 2001). These collapses can occur over a range of scales, from small landslides, volcanic debris flows and lahars, to massive rock avalanches (Calder et al, 2002; Pollet & Schneider, 2004; Cecchi et al, 2004; Hermanns, 2013).

Rock avalanches, or sturzstroms, are defined as very large-scale collapses of unconsolidated granular material (Pollet & Schneider, 2004; Hermanns, 2013), which can travel up to 20-30 times their vertical drop (Schneider et al., 2004; Hermanns, 2013), exceed speeds of 100km/hr and are driven by brittle dynamic disintegration processes (Sørensen & Bauer, 2003; Pollet & Schneider, 2004). Lahars are defined as flowing muddy slurries composed of water and volcanic material (Waitt, 2016). Volcanic debris avalanches (VDAs) are rapid mass movements of unconsolidated material, often on a smaller scale than sturzstorms (Giardino, 2013). VDAs are the collapse deposit at the focus of this study.

1.1.3 Volcanic Debris Avalanches and Their Deposits

VDAs are gravity-driven, granular mass movements of collapsed volcanic edifice material (Perinotto et al., 2015). They are preserved in the geological record as volcanic debris avalanche deposits (VDADs). 75% of all VDADs worldwide occur on composite volcanoes, or ocean island volcanoes (Dufresne et al., 2020). Sonar imaging of the submerged flanks of volcanic islands reveals that these flows can travel tens of kilometres underwater (Varnes, 1978; Moore et al, 1989; Mitchell, 2003).

In subaerial settings, VDAs can involve volumes up to two orders of magnitude larger than most non-volcanic rock and debris avalanches, reach speeds of up to 150m/s and can travel tens of kilometres, often exploiting existing depressions in topography, or overcoming topographic barriers, leaving deposits up to hundreds of metres thick (Siebert et al 1987; Crandell 1989; Scott et al., 2001; Sosio et al., 2012; Roverato et al., 2015). Large scale VDAs can result in deep-seated slips that can decompress magmatic systems, in some cases triggering eruptions (Hunt et al., 2018).

1.1.4 Volcanic Debris Avalanche Macrostructure

The structure of VDADs varies between proximal, medial and distal regions of the deposit, as well as vertically through the deposit.

Characteristic features that can be recognised in the field include an irregular, hummocky topography comprising mounds where megablocks lie below the surface, longitudinal and transverse ridges, shattered and jigsaw-fit clasts, shear structures, rip-up clasts, and incomplete mixing of lithologies including megaclasts of the original volcano which can preserve original structures (Ui, 1983; Siebert, 1984; Ui et al, 1986; van Wyk de Vries et al., 2001; Zernack et al., 2009; Roverato & Capra, 2013; Roverato et al., 2015). The source of VDADs lies in the detachment surface on flank of the volcanic edifice and is commonly marked by a horseshoe-shaped amphitheatre (Siebert, 1984; Bernard et al., 2019). Toreva blocks are detached blocks of volcanic edifice which exhibit a characteristic backwards-rotation towards the source area, and remain proximal to the detachment site (van Wyk de Vries et al., 2001; Dufresne et al., 2021). See Figure 1.1.

The internal lithofacies of VDADs are characterised by megaclasts (>1m in diameter), clasts (<1m in diameter) and a fine-grained matrix (Palmer et al., 1991; Glicken, 1996; Alloway et al, 2005; Bernard et al., 2019). Both clasts and matrix can comprise collapsed edifice material and material entrained during flow (Roverato et al., 2015; Dufresne et al., 2021). The abundance of entrained clasts is greatest near the base of the deposit and in more distal regions (Palmer et al., 1991). With distance from the detachment surface, matrix material becomes more dominant while the size and frequency of megaclasts decreases (Neall, 1976). Megaclasts are generally in-tact fragments of the source volcanic edifice and commonly exhibit jigsaw-fit clasts, where clasts are mechanically pulled apart but have not disaggregated completely, characterised by clasts with irregular cracks that fit together (Ui, 1963; Shreve, 1968; Ui & Glicken, 1986; Glicken, 1996; Ui et al., 2000). Clasts become more disaggregated and cracks become infilled with matrix material further form the source (Brideau & Procter, 2005).

At the base of VDADs, a mixed zone is common. Basal zones can be millimetres to several metres thick and are in contact with underlying strata, consisting of a mix of original and entrained avalanche material (Dufresne et al., 2021). Abrasive structures

are common along the base, for example striae and channels (Schneider & Fisher, 1998) as well as deformation structures such as boudinage, folding and shearing of the substrate, vortex structures, impact features from rock collisions, hackly textures and ramp structures similar to thrust faults (Clavero et al., 2004; Bernard et al., 2021). Shearing at the base of VDAs can be sufficient to produce frictionite or pseudotachylite (Legros et al., 2000; Dufresne et al., 2021). Conversely, some basal contacts are flat with no observable structures (Clavero et al., 2002).

Fluid-like injections of finer material within VDADs are common and resemble flame structures, indicating that finer material can behave in a mobile or viscous manner, as a granular fluidised mass (Schneider& Fisher, 1998; Bernard & van Wyk de Vries, 2010; van Wyk de Vries & Davies, 2015; Siebert et al., 2017; Dufresne et al., 2021). Injections of VDA material into the substratum are less common but have been observed (e.g., Schneider & Fisher, 1998).

The sedimentary architecture of VDADs can be used to determine the triggering mechanism. For example, dry, granular deposits such as that of Mt. St. Helens are typically produced during magmatic eruptions and are rich in juvenile components and interstratified with pyroclastic density currents and lahars (Siebert et al., 1987; Belousov et al.,1999). Conversely, VDADs produced during phreatomagmatic events are typically more cohesive with a higher proportion of matrix due to higher water saturation and greater pore pressures (Siebert, 1984; Dufresne, 2021) and VDADs produced during seismic or gravitational events are often more angular and chaotic breccias (e.g. Siebert, 1984).

VDAs occur over very short geological timescales and become quickly obscured by erosion and new volcanic deposits. This presents a challenge in identifying historic collapses which may have been eroded, therefore no longer closely resembling original geometries and macrostructure.

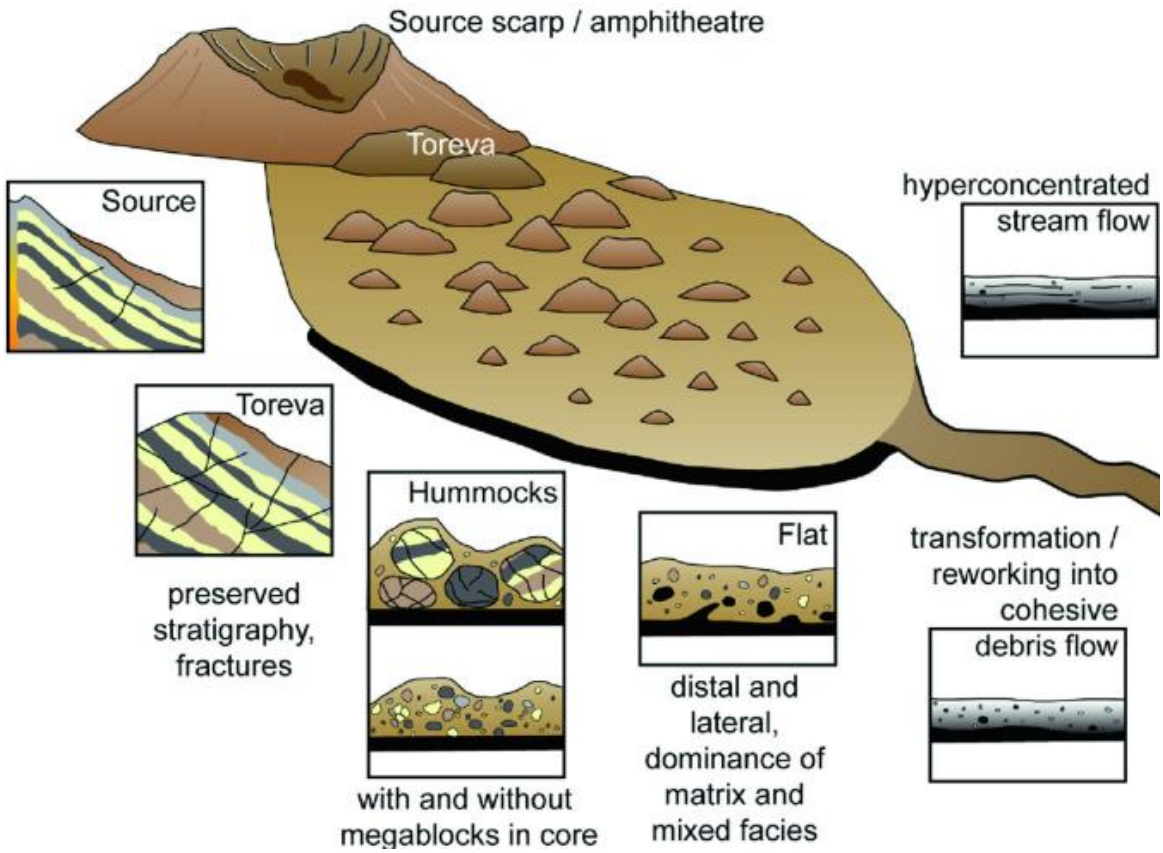

Figure 1.1 Proximal to distal variation of a VDAD showing source scarp, toreva blocks, origin of hummocks, increase in matrix with distance from source and post-deposition reworking (Dufresne et al., 2020).

1.1.5 Volcanic Debris Avalanche Microstructure

Microstructural observations within VDADs include microcracks on sand-sized particles, which may exhibit small-scale displacements and hackly morphology, shown by highly irregular surface textures at micron scale (Figure 1.2). Such textures have been observed in Mt. St. Helens VDAD samples (Komorowski et al., 1991) and those from Shiveluch volcano in Kamchatka (Belousov et al., 1999).

Other common textures observed at micron-scale include parallel grooves and scratches, percussion marks, staircase geometry and broken crystals (Roverato et al., 2015; Dufresne et al., 2021). Microfractures, often with minor displacement or pull-apart features, are also common, some grains may exhibit multiple phases of breakage where fractures crosscut one another (Figure 1.2) (Roverato et al., 2015; Dufresne et al., 2021).

Caballero and Capra (2011) categorise these microtextures into either the ‘basal group’ or the ‘upper group’. The basal group describes microtextures formed by ongoing particle-particle interaction such as parallel ridges and grooves, scratches and lips while the upper group comprises microtextures formed by rapid particle-particle interactions such as microfractures, percussion marks and broken or ground crystals. The basal group microtextures suggest that a VDA was moving in a way that allowed for longer particle-particle interactions whereas the characteristics of the upper group suggest that particles could move freely, interacting predominantly by collision (Cabellero & Capra, 2011).

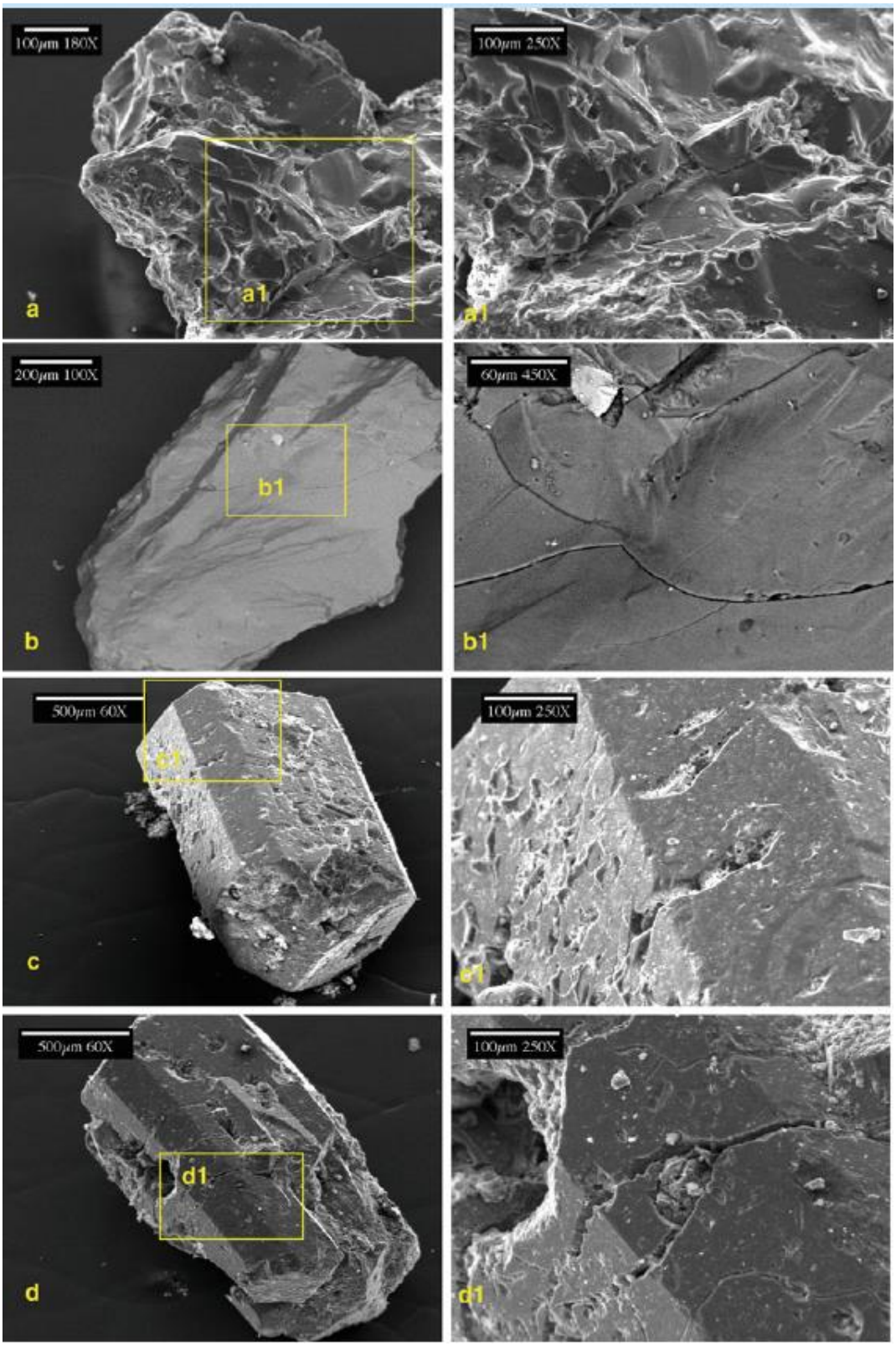

Figure 1.2 a) collision surfaces and fracturing, close up shown in a1, b) conchoidal fracturing, close up in b1, c) impact marks with rounding of edges and fracturing, close up in c1, d) fracturing, close up in d1 (Procter et al., 2021).

1.1.6 Transport and Emplacement

VDAs accelerate due to a rapid loss of resistance at the base of the collapsing rock mass. Collapse propagates through normal faulting of volcanic edifice material (Figure 1.3). This results in a fast moving, highly mobile, gravity-driven, deforming mass that travels downslope up to tens of kilometres (Sigurdsson et al., 2015).

VDAs are gravitational granular flows, whereby particle-particle interactions occur within a collisional or frictional regime (Roverato et al., 2021). Transport dynamics can be affected by the presence of water and clay minerals, whether these originate from the edifice or are entrained during runout, by changing flow behaviour and reducing particle contact (Palmer et al., 1991; Bernard et al., 2009; Roverato et al., 2015). The addition of water allows VDAs to have characteristically long run-out distances in terrestrial environments and upon entry to submarine environments where they can travel tens of kilometres through pre-existing canyons (Scott et al., 2001; Brunet et al., 2017). The high mobility of VDAs can be further explained by elastic energy release during dynamic disintegration. Dynamic disintegration describes the fragmentation of rock particles during flow which results in a reduction in clast size by interparticle collisions and breakage by continuous energy release (Schneider & Fisher, 1998; Davies & McSaveney, 2006). This leads to a reduction of friction within the matrix due to interactions between finer particles (Perinotto et al., 2015). This may maintain the dilatancy - the expansion of material from its original, in-situ density - of the granular mass, contributing to high mobility (Glicken, 1991).

Larger volume VDAs travel greater distances (Hughes et al., 2020). This supports the importance of a mechanism to lower frictional coefficients to facilitate mobility (Shea & van Wyk de Vries, 2008). This behaviour has been observed in all rock types (Legros, 2002) and proposed mechanisms aside from dynamic disintegration include mechanical fluidisation (Campbell et al., 1995), the role of groundwater as a lubricant (De Blasio, 2011; Hu et al., 2019), air as a lubricant (Shreve, 1968), acoustic fluidisation (Johnson et al., 2016), mechanical and fluid pressurisation (Ferri et al., 2011), and the formation of a lubricating melt layer (Wang et al., 2017).

Inter-particle collisions within the VDA lead to progressive grain size reduction and an increase in matrix relative to blocks with distance travelled (Perinotto et al., 2015). Provided that topographic confinement remains sufficient to maintain high enough

frictional or shear stress, syn-transport fragmentation, collisional fracturing and crushing continue, and the proportion of matrix material increases towards more distal regions (Paguican et al, 2020).

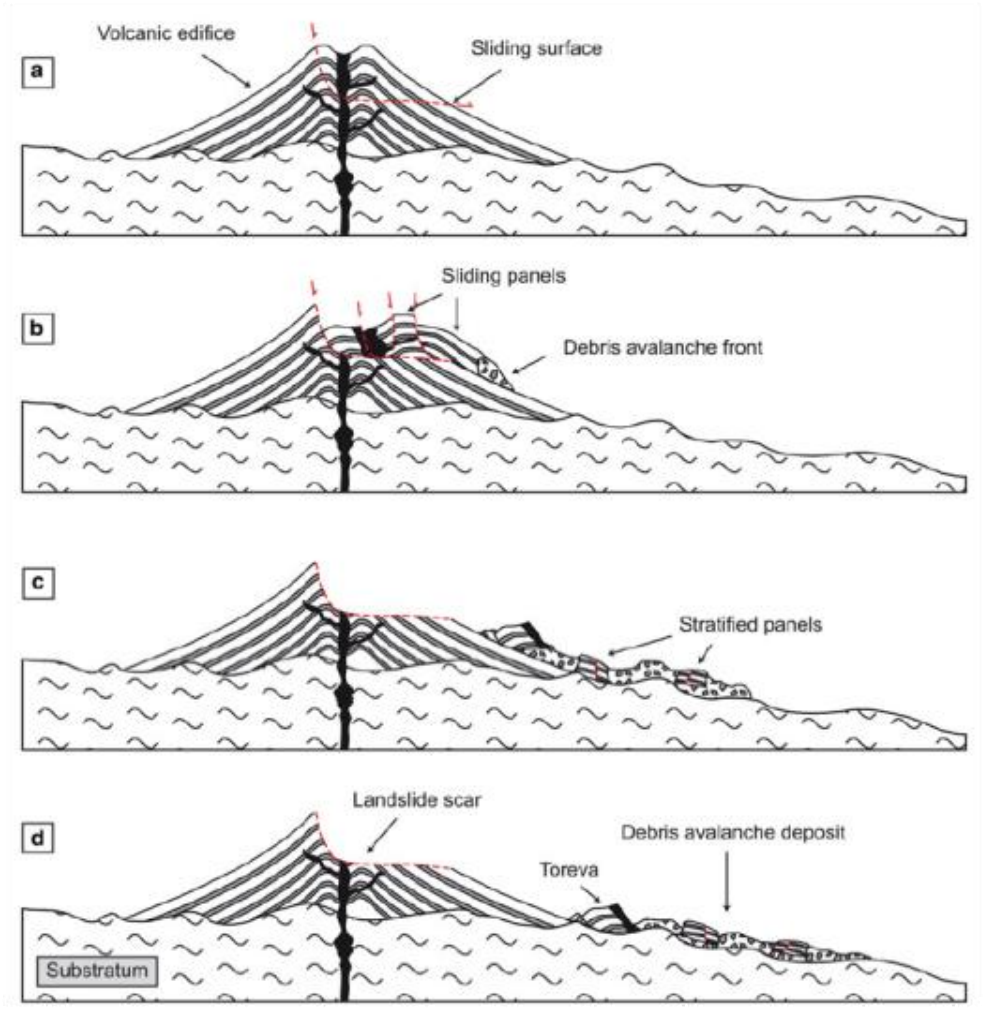

Figure 1.3 Volcanic debris avalanche propagation showing a) starting state, b) initial sliding, c) transport and d) final state (Bernard, 2021).

1.1.7 Triggers and Instability

Volcanic edifices are inherently unstable, being formed over short geological timescales by the layering of volcanic material (Voight, 2000; Acocella & Puglisi, 2010). The stability of a volcanic edifice relies on multiple factors, but primarily on the outer slope angle; when a critical angle is reached, instability leads to collapse (Roverato et al., 2021). Factors that can lead to destabilisation of the edifice do so by changing this configuration, causing an approach towards the critical angle. This

instability typically leads to structural failure and subsequent lateral collapse when driving forces overcome resistive forces (Sigurdsson et al., 2015).

Instability of the volcanic edifice can be caused by tectonic or volcanic factors such as magmatic intrusions, hydrothermal processes, sub-volcanic basement behaviour and seismic activity, or exogenous processes including weathering and climatic events (Vallance & Scott 1997; Kerle & van Wyk de Vries, 2001; van Wyk de Vries et al., 2001; Mitchell, 2003; Norini et al., 2020; Roverato et al., 2021). Destabilising factors can also include increased pore fluid pressures due to changes in hydrothermal systems or the addition of meteoric water, magma intrusions and resulting microseismicity, hydrothermal alteration, basement deformation and eruptions (Roverato et al., 2021; Sigurdsson, 2015). Some data suggest that landsliding shows no observable relationship to rainfall as landslides occur equally in wet and dry climates (Mitchell, 2003), however it is widely observed that water can act as a weakening mechanism for volcanic edifice failure (Alparone et al., 2013; Denlinger & Morgan, 2014; Azzaro et al., 2017).

Instability can follow short-lived destabilisation, for example the cryptodome intrusion at Mt St Helens which occurred a few months prior to collapse, or long-lived destabilisation, such as long-term hydrothermal alteration or cumulative destabilisation following many smaller-scale events. In the case of the 1980 Mt. St. Helens collapse, cryptodome failure probably resulted from a combination of factors including, but not limited to, shallow seismicity, intrusion resulting in changes in pore fluid pressure and slab failure along pre-existing fault planes (Donnadieu et al., 2001).

1.2 Shear Zones of Collapse Deposits

1.2.1 Localised and Diffuse Strain Accommodation

Strain in mass movements can be localised along one or more sliding surfaces (e.g. Jiang & White, 1995; Belousov, 1999; Wang et al., 2010; Chen et al., 2014; Hughes et al., 2020), or diffuse, dissipating strain over a wider region (e.g. Wang, 2017; Dufresne et al., 2017; Zhang & McSaveney, 2017). Sliding surfaces, or shear zones, within mass movements are subjected to extreme shear conditions localised along a narrow layer (Erismann & Abele, 2001; De Blasio & Elverhøi, 2008). These can be basal or intra-deposit. Brittle processes tend to dominate within localised shear zones, and ductile deformation is more common in systems where strain is more diffuse.

1.2.2 Brittle and Ductile Strain Accommodation

Investigation into sheared rocks commonly focusses on fault rocks. Fault rocks present varying levels of strain as a result of shear. Exogenous factors e.g. normal pressure, shear stress and temperature, and endogenous factors e.g. rock composition and water content, all affect how strain is accommodated (Ramsay, 1980). Changes in these variables determine whether strain is accommodated in a brittle or ductile manner (Figure 1.4) and resultingly whether sheared rocks are foliated, non-foliated, cohesive, or non-cohesive (Figure 1.5). Brittle failure occurs when fracture happens at low strain, whereas ductile behaviour allows for plastic deformation under higher strain before failure.

Brittle shear zones tend to be highly localised (see Section 1.2.1) and strain is accommodated by cataclastic processes such as grain fracturing and dynamic disintegration (Ramsay, 1980) as fracture occurs at low strain (Figure 1.4). Brittle processes commonly occur at low temperatures. This results in non-foliated rocks which can be non-cohesive e.g. breccia and unconsolidated gouge (Figure 1.5, A,B), cohesive e.g. cataclasites (Figure 1.5, D-F), or cohesive and glassy e.g. pseudotachylite (Figure 1.5, C). Cataclasis describes the friction-dependent process of brittle grain size reduction by fracturing, granulation, and crushing of grains to produce finer material (Engelder, 1987; Anthony & Marone, 2005; Billi, 2005). In gravitational collapse flows, the localisation of shear along a sliding surface often results in the formation of a cataclasite (e.g Wang et al., 2010) and sometimes the formation of a pseudotachylite, where grains have melted (e.g. Hughes et al., 2020). This is because, unlike fault zones, temperatures and pressures are not high enough to produce foliated rocks.

Ductile shear is often more diffuse (see Section 1.2.1) and strain is accommodated by ductile flow and reorganisation of minerals under plastic behaviour (Ramsay, 1980). Ductile shear requires higher temperatures and results in foliated rocks which may be non-cohesive e.g. foliated gouge (Figure 1.5, G), or cohesive e.g. mylonites (Figure 1.5, H-J), or blastomylonites (Figure 1.5, K), which involve the recrystallisation of minerals.

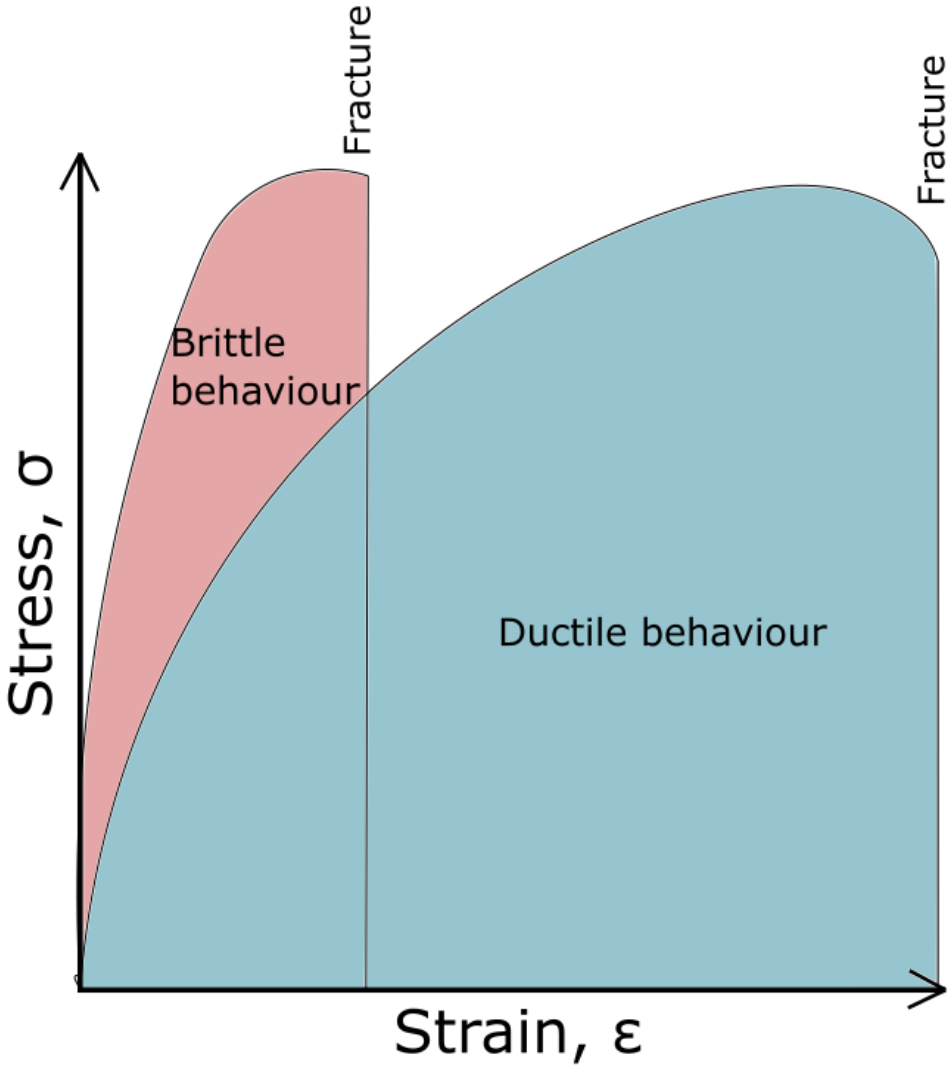

Figure 1.4 Stress-strain curve for brittle vs ductile materials showing that brittle fracture occurs at low strain, whereas ductile materials fail after significant plastic strain.

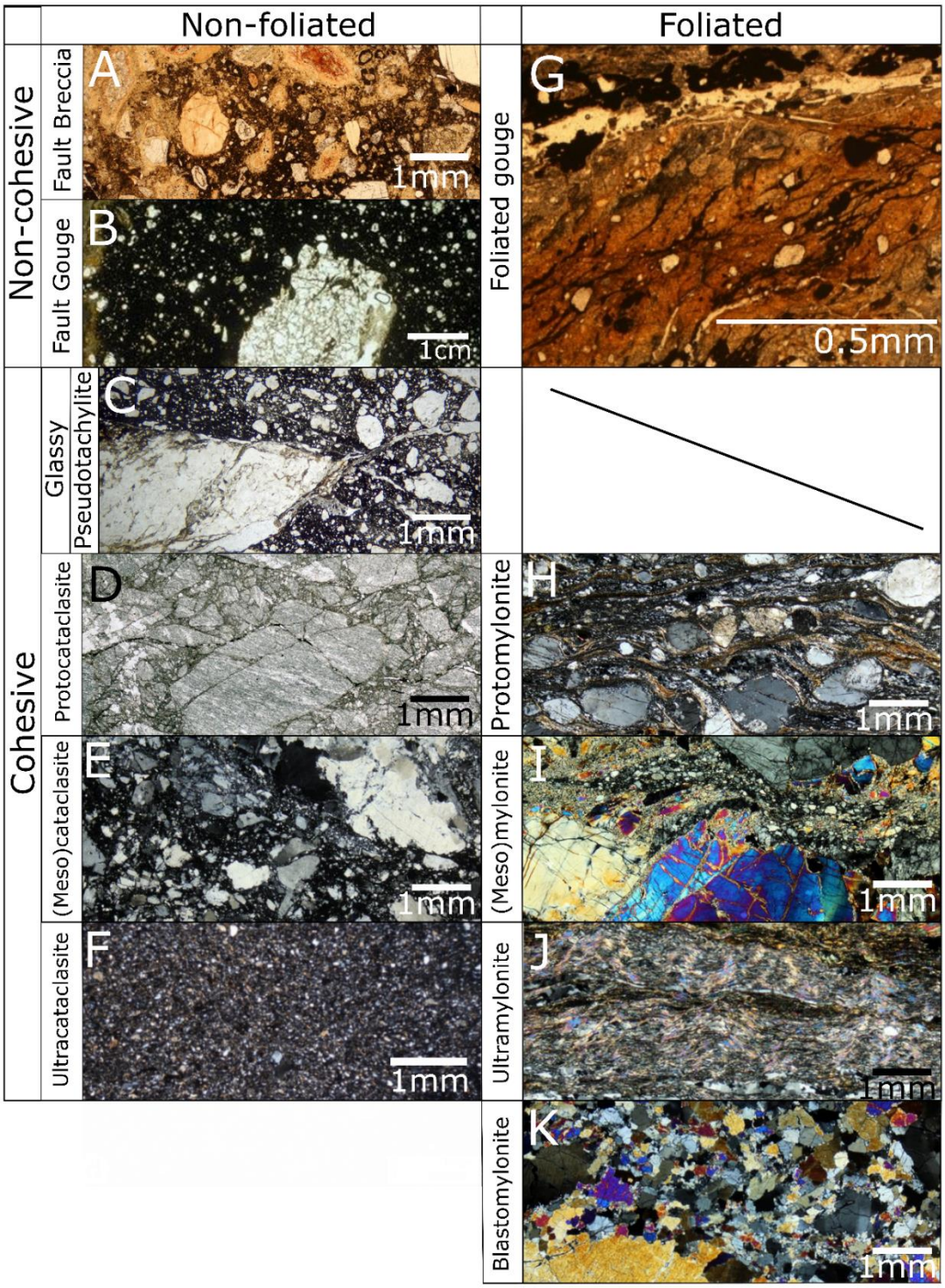

Figure 1.5 Microscope imagery of various classifications of fault rocks showing microstructural variation between cohesive, non-cohesive, foliated and non-foliated rocks. Table adapted from Sibson (1977) and Woodcock (2008). A) Fault breccia (>30% visible matrix) of mafic origin, PPL (Strekeisen, 2020), B) Fault gouge (<30% visible matrix) of carbonate origin, XPL (Innocenzi et al., 2021), C) Pseudotachylite (black = glass), PPL

(Strekeisen, 2020), D) Protocataclasite (0-50% matrix) of carbonate origin, PPL (Strekeisen, 2020), E) Cataclasite (50-90% matrix) of granitic origin, XPL (Strekeisen, 2020), F) Ultracataclasite (90-100% matrix) derived from biotite rich granite, PPL (Kim & Lee, 2016), G) Foliated gouge of mafic origin, PPL (Song et al., 2012), H) Protomylonite (0-50% matrix) with feldspar porphyroclasts, XPL (Strekeisen, 2020) , [I-J Mylonites are formed following mechanical grain size reduction] I) Mylonite (50-90% matrix) in mylonitic dunite, XPL (Strekeisen, 2020), J) Ultramylonite (90-100% matrix) composed of quartz and mica rich bands (Strekeisen, 2020), [K Blastomylonite is formed by grain recrystallisation] K) Blastomylonite containing olivine crystals, XPL (Strekeisen, 2020).

1.3 Experimental Shearing Work

Shear zones generated within faults are well studied in scientific literature and have provided the basis for much experimental investigation. Rotary shear experiments, whereby powdered rock gouge is sheared at a controlled velocity and normal load, are widely used to investigate mechanical behaviour of rocks during fault movement (e.g. Morrow et al., 1984; Marone, 1989; Marone & Raleigh, 1990; Fukoka et al., 2006; Di Toro et al., 2011; Togo & Shiamoto, 2012; Haines et al., 2013; Sawai et al., 2014; De Paola et al., 2015; Verberne & Niemeijer, 2015; Scuderi et al., 2017; Pozzi et al., 2021). These techniques have been more recently applied to investigate shear surfaces during gravitational collapses, as many of the same concepts and experimental methods can be applied (e.g. Wang et al., 2010; Ferri et al., 2011; Smeraglia et al., 2017; Hughes et al., 2020). This is a growing area of research and concepts are being continually developed.

Shearing experiments provide two useful outputs, these are: (1) Mechanical data, and (2) Microstructural data.

1.3.1 Mechanical Data

Experiments conducted on high velocity rotary shear apparatus are used to determine, among other parameters, frictional relationships to shearing (Di Toro et al., 2011). Determining rock friction at a given slip rate is important to understand strengthening and weakening behaviour and resulting microstructures and the formation of a principal slip zone (PSZ), the narrow area along which shear is localised (Verberne et al., 2019). Key processes controlling slip behaviour occur in the PSZ and these are dependent on physical properties, such as grain size and porosity.

The frictional response to a change in slip rate is described in terms of *rate and state* laws (Marone, 1998; Scholz, 1998). With a step increase in velocity, there is a brief increase in friction, called the direct effect, denoted as *a*. This is followed by a gradual decrease in friction, the evolution effect, denoted as *b*. This frictional reaction to velocity change is observed in rock gouges of a wide range of mineral compositions (Pozzi et al., 2021, Figure 1.6). Friction rate dependence, which is a material property corresponding to velocity weakening or velocity strengthening behaviour, is given as *a-b* (Marone, 1998; Mair & Marone, 1999). Velocity weakening describes a process by which friction decreases with increasing velocity, whereas velocity strengthening occurs when frictional resistance increases with increasing sliding velocity (Scholz & Engelder, 1976; Bar-Sinai et al., 2015). A negative *a-b* value corresponds to velocity weakening behaviour, which is inherently unstable, whereas a positive *a-b* value corresponds to velocity strengthening behaviour, which is inherently stable.

Velocity stepping experiments are used to investigate material behaviour during slip nucleation by examining the frictional response to a change in slip rate, in order to discern velocity weakening or strengthening behaviour. Slip rate is periodically increased and decreased, or stepped up and down, while normal load remains constant. Generally, velocity stepping experiments run for the order of minutes and often use slip rates from µm/s to mm/s.

To investigate slip propagation, short (in the order of seconds), higher velocity (often m/s) shear is applied to rock gouges. Similarly, the friction coefficients from such experiments can provide insight into mechanical behaviour (Di Toro et al., 2004; Ma et al., 2014). Specifically, data from these experiments can be used to define peak friction, immediately following velocity increase, and steady state friction, after the friction gradually drops following this peak. The slip weakening distance is the difference between the displacement distance at peak friction and the displacement distance at steady state friction. These parameters are useful to compare between experimental runs when variables such as velocity, normal load and the addition of fluids have been changed.

Several factors can influence friction coefficients and resulting velocity strengthening or weakening behaviours. These include normal load, the presence of fluids, and material composition (Lucas et al., 2014; Perinotto et al., 2015). Additionally, heat

generation during shearing can aid transition from brittle to ductile shearing regimes by the production of melt and pseudotachylite (Ramsay, 1980).

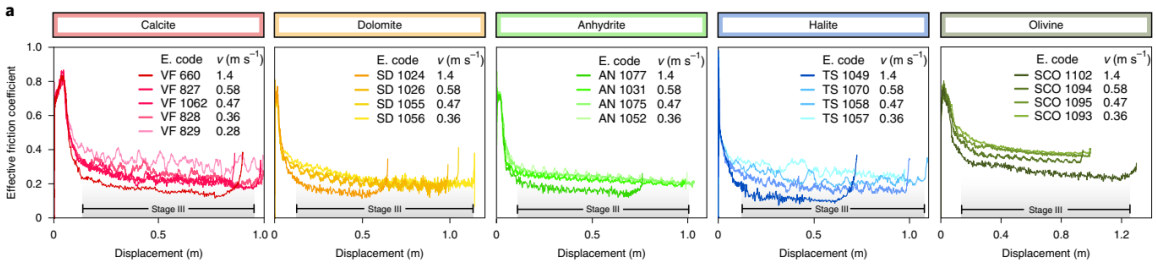

Figure 1.6 Increase in velocity leads to a brief increase in friction, followed by a gradual decrease in friction observed in a range of powdered materials (Pozzi et al., 2021).

1.3.2 Microstructural Data

Examination of experimental shear zones, commonly done using SEM imagery, can provide information on the development and distribution of strain along the PSZ. PSZs show markedly different characteristics to the unsheared starting material, and those developed during rotary shear experiments are generally a few tens of microns thick with very low porosity, quasi-homogeneous fine grain size distribution, and sometimes show oblique foliation, although usually only at high normal pressures >25MPa (Mair et al., 2002; Pozzi et al., 2021).

Examination of shear zones can help to determine whether brittle or ductile regimes dominated during shear accommodation. For example, by the development of foliation for ductile flow, or evidence of cataclasis for brittle grain comminution, as described above.

The investigation of shear zones generated by mass movement explores brittle cataclastic processes. The development of microstructural features such as grain size reduction, porosity reduction, and grain geometry evolution along the PSZ are evidence for cataclasis (Sibson, 1977; Borradaile, 1981; Tullis & Yund, 1987; Blenkinsop, 1991). Grain size decreases with shearing, which in turn drives a decrease in porosity along the PSZ (Kimura et al., 2018), and grains become better rounded with increasing shear (Mair & Abe, 2011).

1.4 Geological Setting: Ascension Island

Ascension Island is a large (~98km^2) ocean island volcano located in the South Atlantic Ocean (Figure 1.7). The highest point of the island is Green Mountain, 770m above sea level (Figure 1.8). The island lies 110km west of the Mid Atlantic Ridge on 7 Ma seafloor (Minshull & Brozena, 1997). The volcanic geology of the island defines a transitional to mildly alkaline sequence that spans a wide range of eruptive styles (Preece et al., 2018). The central to eastern regions of the island are predominantly composed of trachyte and rhyolite pyroclastic deposits, lava flows and domes, and the northern, southern and western regions comprise scoria cones and mafic lava flows (Weaver, 1996; Preece et al., 2018). Ascension Island is considered an active volcano, insofar as it is proven to have erupted during the Holocene (Venzke, 2013; Siebert et al., 2015; Preece et al., 2018).

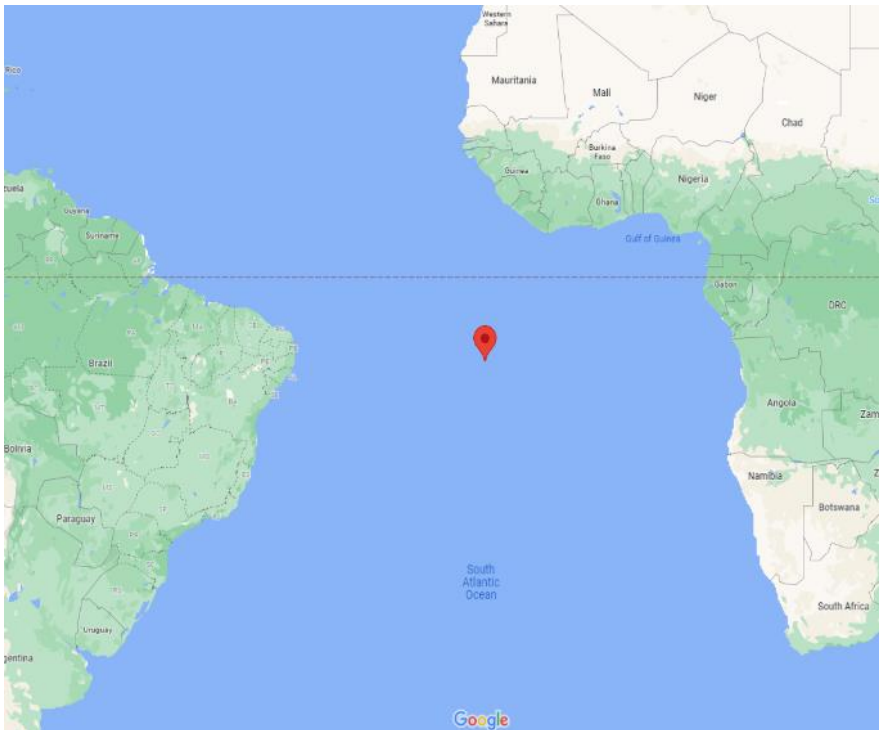

Figure 1.7 Location of Ascension Island (Google Maps, 2021).

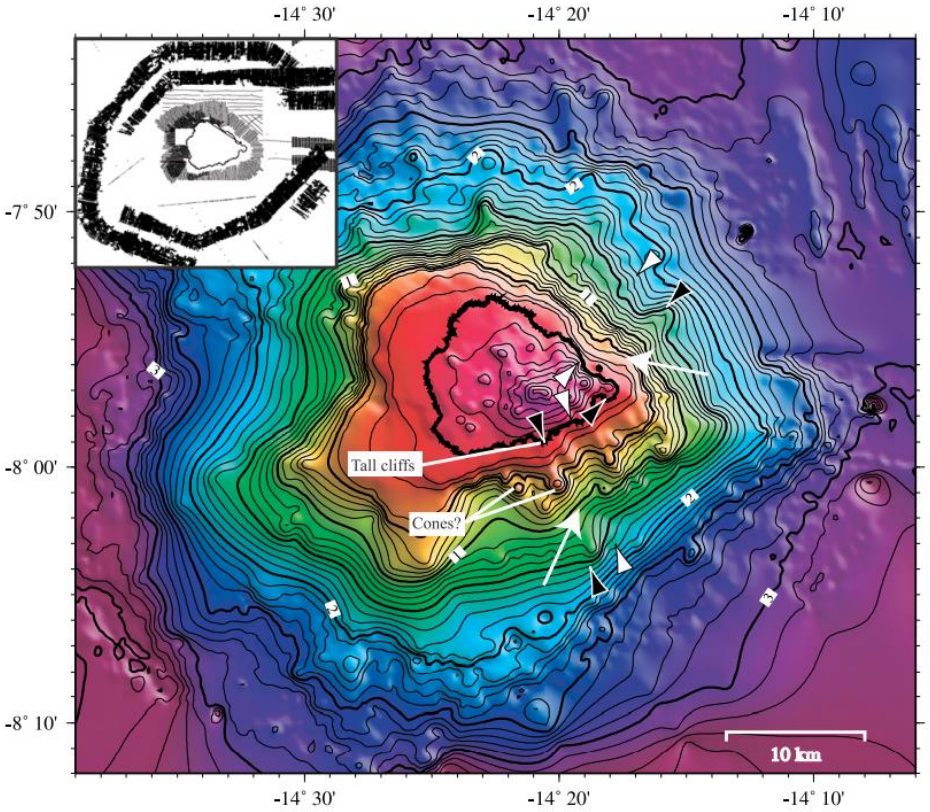

Figure 1.8 Topographic map of Ascension Island, showing location of Green Mountain, the highest point (Mitchell, 2003).

1.4.1 Green Mountain VDAD

A small-volume (~4 x 10^6 m^3) VDAD covering 2km^2 originated from the partial collapse of the northern flank of the Green Mountain scoria cone, which sits at 550 metres above sea level (Figure 1.9). The eruption that produced the scoria deposit is dated at 300Ka (Preece et al., 2021). The avalanche travelled 2 km down a ~10° slope, before stopping in a small basin against a lava dome at 190m above sea level. Over most of its length the VDAD overlies in-situ Green Mountain scoria that was dispersed north during the eruption. The bulk of the VDAD is composed of semi-coherent, metre scale blocks of scoria with a poorly sorted volcaniclastic matrix composed of a hetereolithic clast population including randomly orientated clasts of basaltic scoria, pumice and lavas. Within the VDAD, the scoria is interspersed with a heterolithic geology, composed of clasts of black scoria, pumice, and oxidised lava randomly orientated in a fine brown matrix, with abundant flame structures (Figure 1.10).

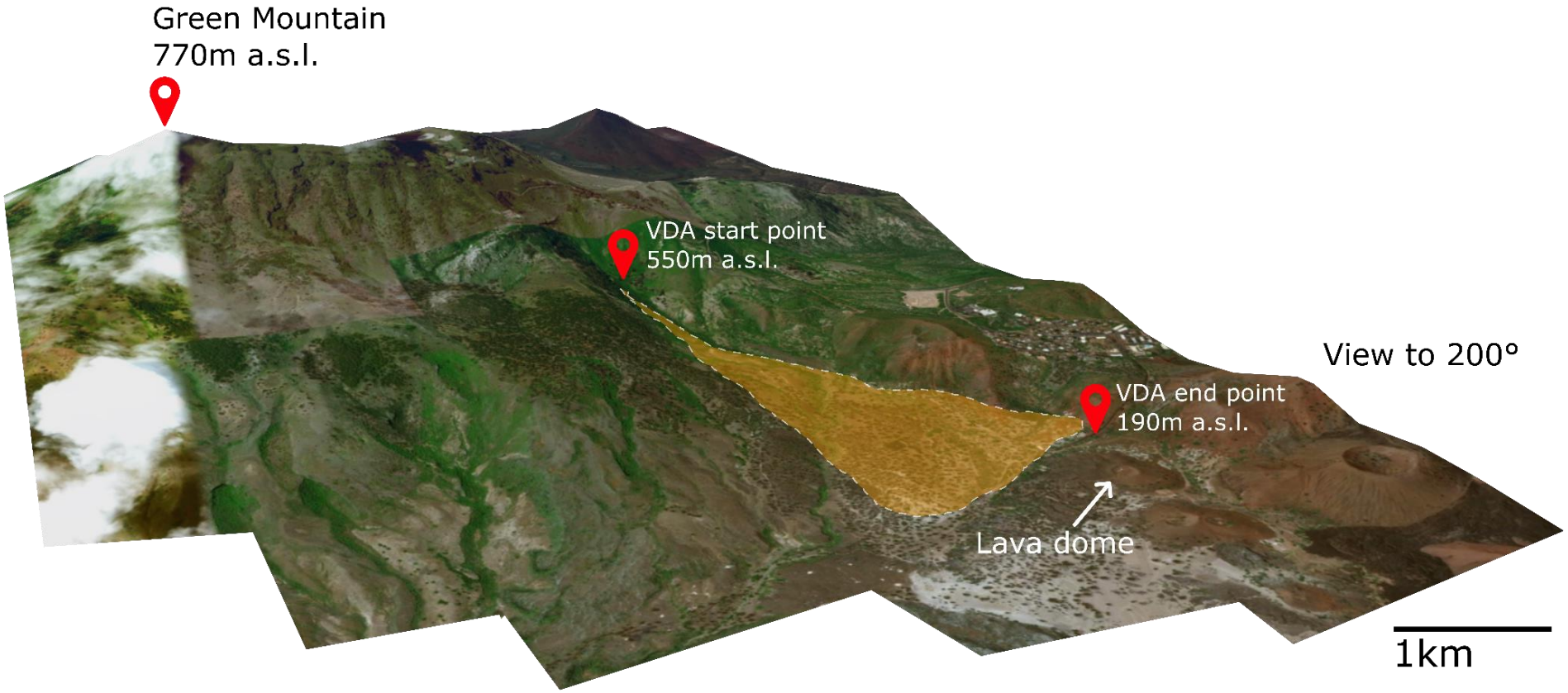

Figure 1.9 Approximate extend of the Green Mountain VDAD, shown in orange. The highest elevation of Green Mountain and the approximate start and end points of the VDAD are given in metres above sea level (a.s.l.). The lava dome against which the VDAD terminates is indicated.

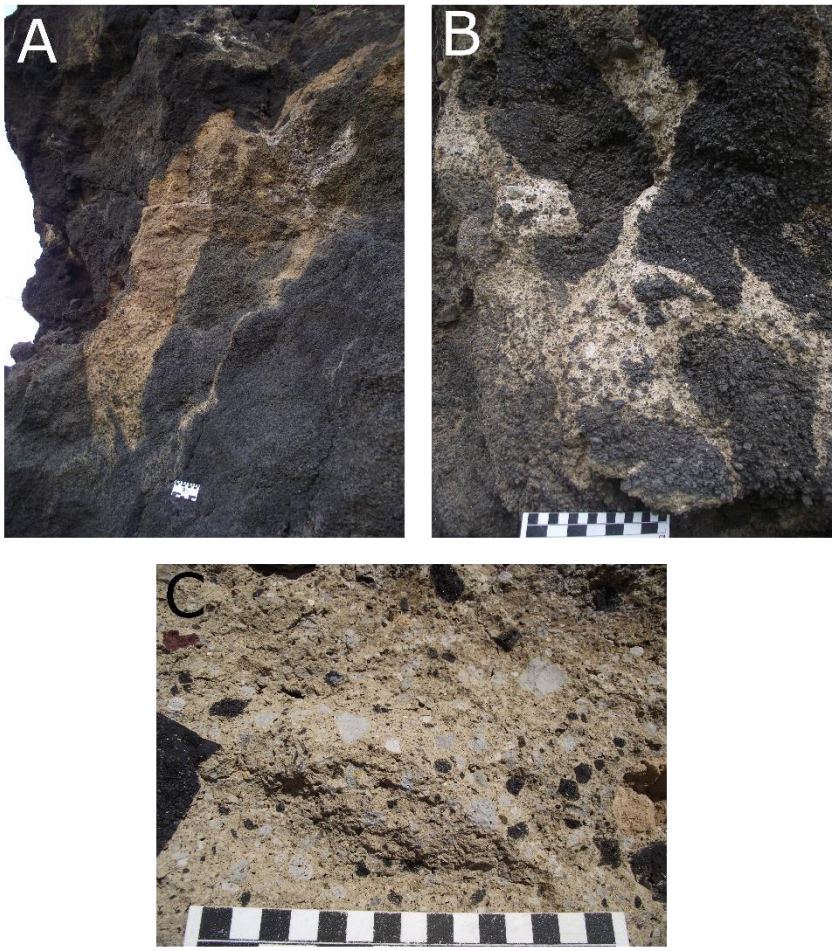

Figure 1.10 A-B) Mixing of heterolithic lithology and flame structures within Green Mountain scoria, within which the shear zone is situated, C) Close up of heterolithic lithology. 15cm grain size card for scale in all photos. Photos from Preece (2015).

1.4.2 Green Mountain VDAD and Accompanying Shear Zone

The VDA originating from collapse of the Green Mountain scoria cone generated a lithified, fine-grained, 1-2 cm-thick shear zone, which is the primary investigation of this thesis. The shear zone overlies Green Mountain scoria, which appears in-situ. Thus, it appears that the shear zone is basal. This is distinguishable in the field and in hand specimen from the rest of the deposit by being finer grained, lighter and indurated (Figure 1.11). The shear zone is structurally different from the scoria fall deposit from which the material originated, and there is also microtextural and microstructural variation from the peripheries of the shear zone to the centre. All field photos and samples within this thesis were collected by Dr Katie Preece (Swansea University) during a field campaign to Ascension Island in April and May 2015.

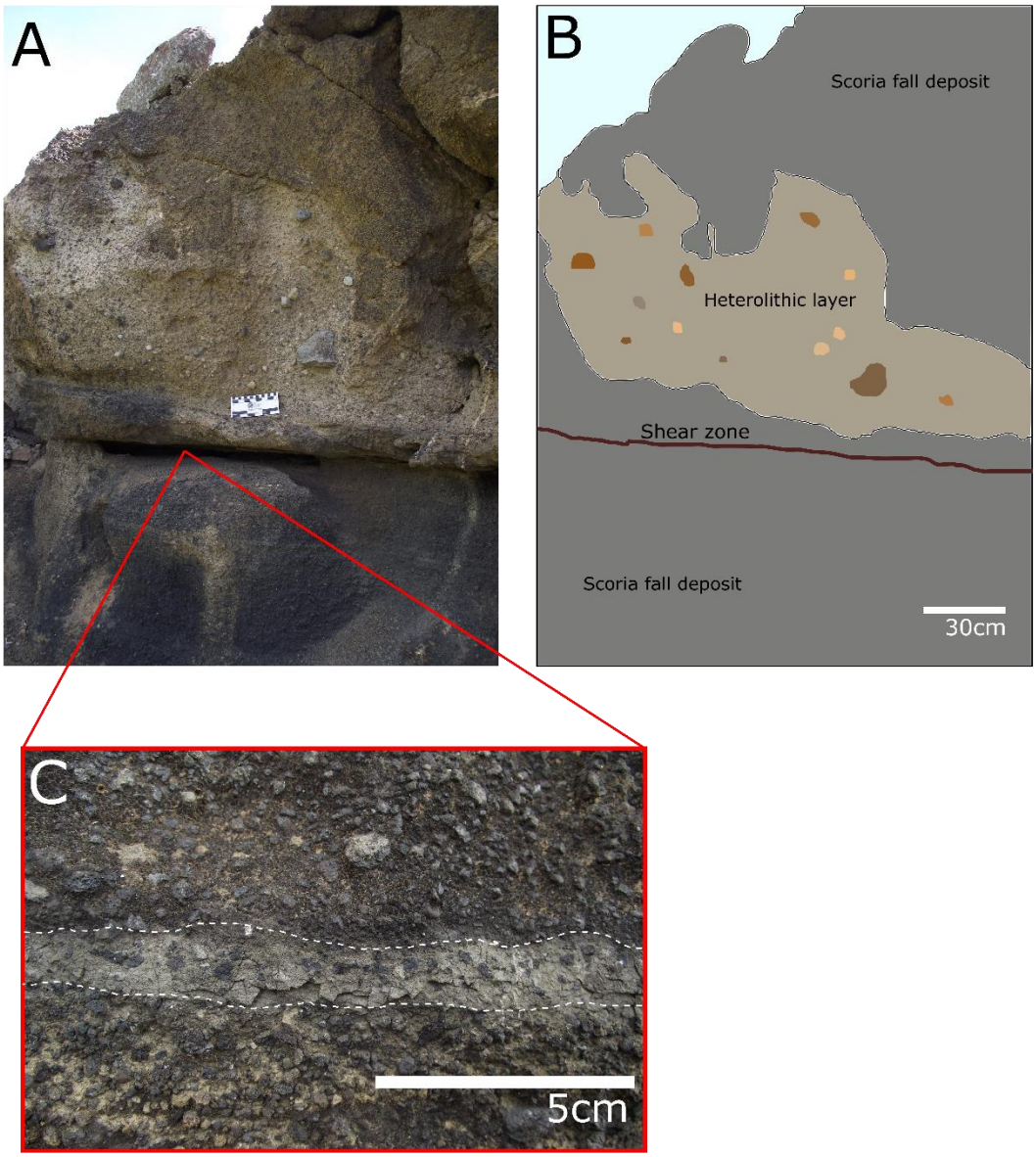

Figure 1.11 A) Green Mountain shear zone and scoria fall deposit which makes up the bulk of the VDAD, interspersed with heterolithic layer, highlighted in B, C) close up of shear zone. Photos from Preece (2015).

This thesis investigates the microstructures of this shear zone and presents experimental work, on order to investigate the mechanical behaviour of the Green Mountain scoria under stress. This provides evidence of the mechanisms which may have occurred during volcanic collapse. Understanding these small-scale dynamics and mechanisms is crucial to explaining the behaviour of large-scale volcanic collapses to mitigate the risks posed by these flows.

1.5 Aims and Objectives

This thesis aims to investigate the (1) microstructural, and (2) micromechanical signatures, properties and processes which occurred during the formation of the Green Mountain Shear Zone (GMSZ). These aims were investigated primarily through experimental work conducted on Green Mountain scoria using a Low to High Velocity Rotary Shearing apparatus (LHVR) to create lab-generated shear zones, and through Scanning Electron Microscope imagery and subsequent image analysis on GMSZ and experimental run products.

The primary aims addressed, and the objectives designed to investigate these aims, are as follows:

1) To identify microstructures and physical characteristics present in the GMSZ, and how porosity, clast size and clast geometry change with depth through the shear zone. This was achieved through SEM imaging of a series of slides and conducting qualitative and quantitative analysis on the images.
2) To understand the mechanical and frictional behaviour of Green Mountain scoria during slip nucleation and propagation and to constrain velocity weakening or strengthening behaviour. Experiments were designed to test the mechanical response of the scoria to varying physical parameters during shearing, including saturation, velocity and normal load. Data were compared between experiments.
3) To understand the translation of mechanical stressors into microstructures and the generation of a PSZ. This was achieved by conducting qualitative and quantitative analysis on SEM images of experimental run products.

Chapter II: Methodology

Image analysis was conducted on SEM images of the GMSZ to investigate microstructural variations with depth. To further investigate microstructural and mechanical behaviour of Green Mountain scoria, experiments on rotary shearing apparatus were conducted on powdered Green Mountain scoria. The outputs from these experiments included (1) the experimental run products, which were impregnated with resin and examined under the SEM to investigate microstructures and, (2) mechanical data which was processed and manipulated to investigate material behaviour. Additional work was conducted using a laser granulometer to investigate the effect of shearing on grain size distribution.

2.1 Microscopy

Ten thin sections were cut perpendicular to the GMSZ. These were examined using Zeiss and Leica optical microscopes and a Hitachi SU-70 high-resolution analytical Scanning Electron Microscope (SEM) equipped with an Oxford Instruments Xmax silicon drift 50mm crystal size liquid nitrogen free detector, in the G.J Russell Electron Microscopy Facility located in the Ogden Institute of Physics, Durham University. The SEM used a voltage of 15.0kV and a working distance between 14.7-15.2mm. 2D images were taken using backscatter and 3D images taken using secondary electrons without backscatter. SEM images of the experimental run products were later taken under the same conditions.

2.2 Quantitative Image Analysis

Image analysis was conducted on the SEM images of the GMSZ to produce quantitative measurements of grain size, porosity, solidity and circularity. This was done using Fiji (Fiji (imagej.net)), an open-source scientific image processing package distribution of ImageJ. See Figure 2.1.

The GMSZ was classified into Zones based on microstructural characteristics (explained further in Chapter III) and vertical location within the shear zone. These are Zones A, B, B', C, C', D, D', E and E' (See Chapter III, Figure 3.1). With distance from Zone A, the centre of the shear zone, towards the basal contact, zones are labelled B' to E' and toward the upper contact are labelled Zones B-E. Zones D and D', the material on the periphery of the shear zone, and Zones E and E' represent the clasts

immediately outside of the shear zone where the clasts were too large to be observed by SEM methods and were measured by hand. Image analysis was conducted on SEM images from all zones to investigate grain size analysis (Section 2.2.1), porosity analysis (Section 2.2.2), and solidity and circularity analysis (Section 2.2.3). Figure 2.1 demonstrates the procedure for image analysis.

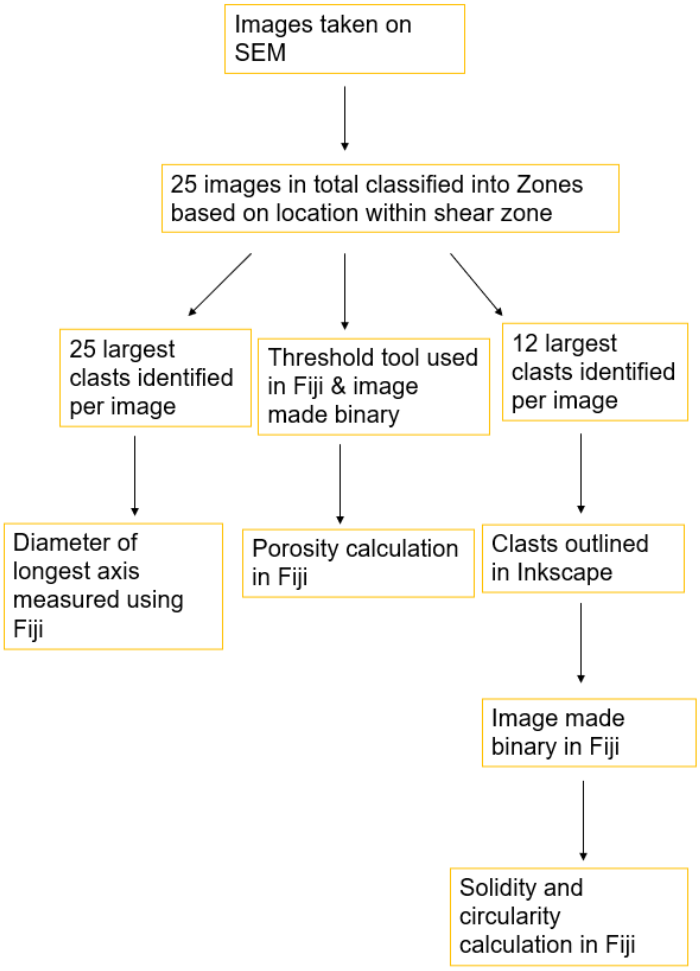

Figure 2.1 Flow chart of image analysis methodology

2.2.1 Grain Size Analysis

For all zones excluding E and E', images from each zone were selected and grain size analysis was done by measuring the long axis of the 25 largest clasts within each image. These were measured using the line distance tool in Fiji. These 25 values were then averaged and plotted. For Zones E and E', the 6 largest clasts were measured by hand from 4 thin section slides; this number was chosen to keep accuracy high.

2.2.2 Porosity Analysis

The colour threshold of SEM images was adjusted in Fiji to accurately identify pore space. These images were then processed as binary (Figure 2.2) to allow for accurate identification between clasts and pore space. The total amount of pore space is calculated and given as a percentage in Fiji. As above, this was conducted on 25 images across the zones and plotted against depth through the shear zone.

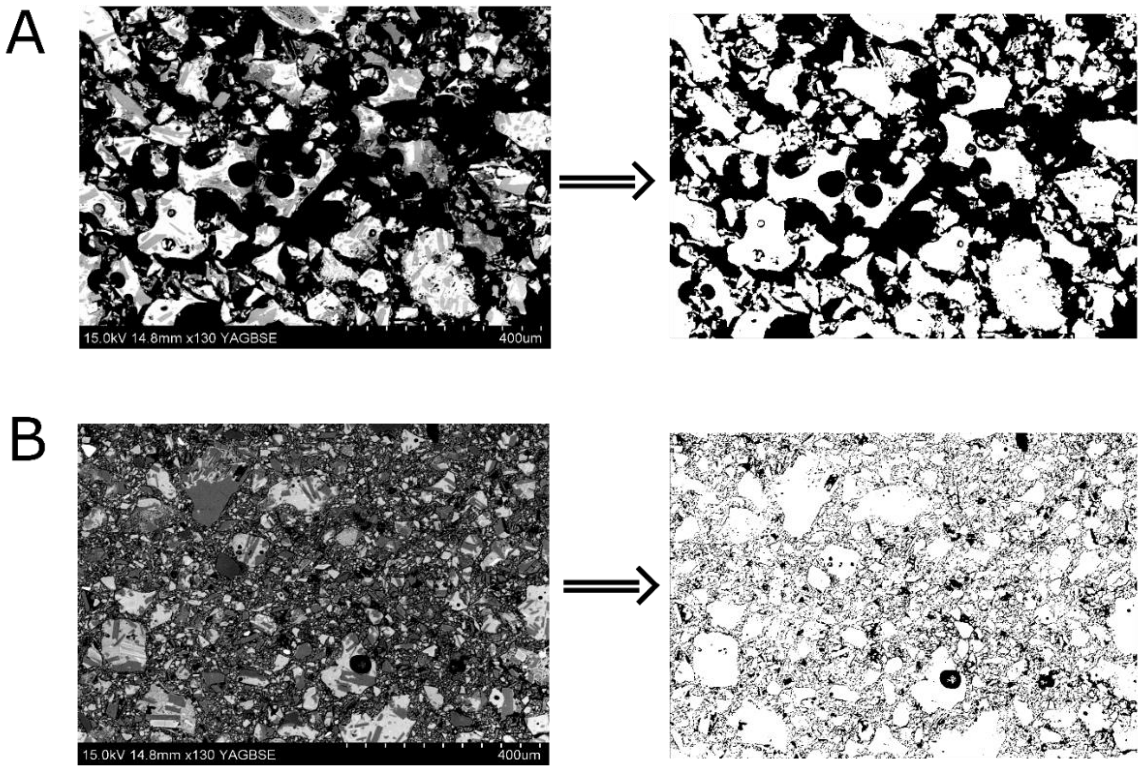

Figure 2.2 Both left hand side images show unprocessed raw SEM images, left hand images show the same images when processed into binary in Fiji to distinguish between pore space (black) and clasts (white). A) Image from Zone D, B) Image from Zone B'

2.2.3 Solidity and Circularity Analysis

Solidity and circularity are both geometric calculations which require the input into Fiji to be a series of discreet shapes. Therefore, the 12 largest clasts from each SEM image were identified and traced out on Inkscape, a vector graphics software, using a Huion Kamvas graphics tablet. These were then input into Fiji and processed as binary. These outlines increased accuracy as clasts that are in contact are counted as one in Fiji. This number was chosen as 12 clasts were generally representative of the clast population, and a tracing around more than 12 clasts for 25 images was limited by time constraints. The outputs of this process are demonstrated in Figure 2.3.

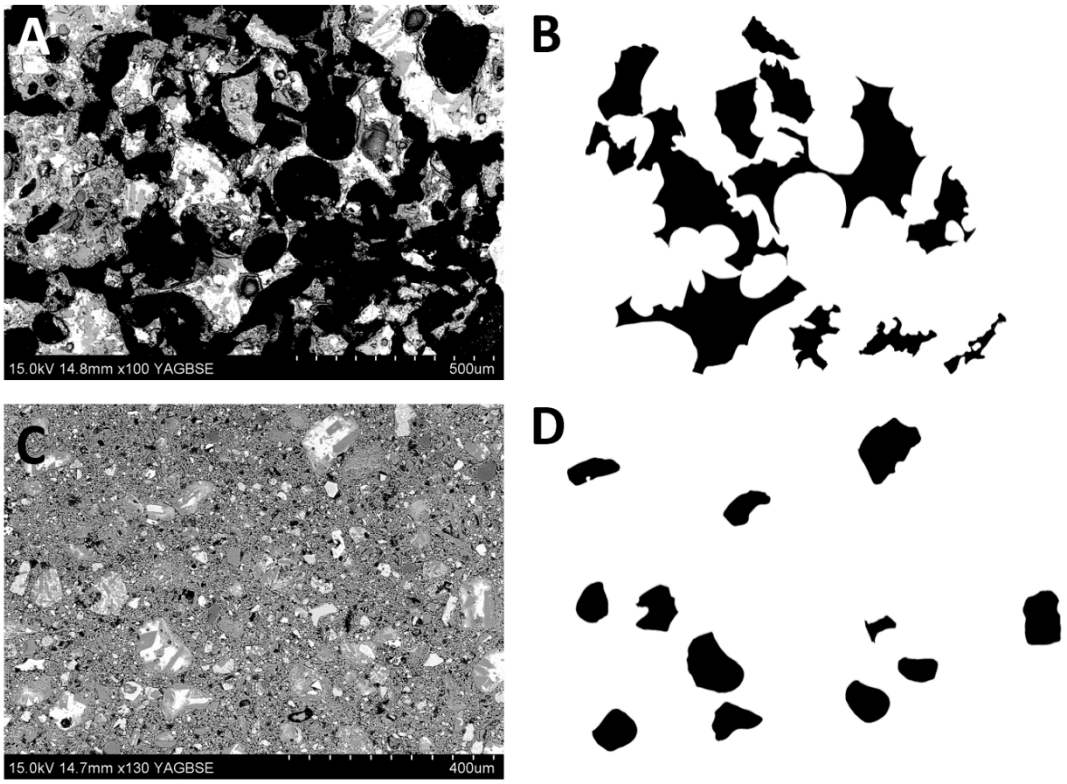

Figure 2.3 Left hand side images show raw SEM image and right hand side images show outlines of clasts that are inputted into Fiji. Image A is from Zone D, image B shows the outlines of the twelve largest clasts. Image C is from Zone A and Image D shows the outlines of the twelve largest clasts. Images B and D were inputted into Fiji for grain geometry analysis for solidity and sphericity.

Solidity is computed in Fiji as the ratio of the area of the grain to the area of the convex hull area fitted around the grain (Kandel et al., 2017) and is given as a value between 0-1. Convex hull area is defined in geometry as the intersection of all convex sets of shape containing a subsection of physical space and can be visualised as the area around which a rubber band would fit a set of points. In this instance, those points are the edges of the clasts. Thus, highly angular clasts with spines and jagged edges have a larger convex hull area than well-rounded clasts (Figure 2.4). Here, a lower solidity value correlates to more angular clasts.

Circularity defines a spheroid's closeness to a spherical geometry (Unak et al., 2021). In Fiji, this is calculated with the formula:

$$circularity = 4\pi\left[\frac{\text{area}}{\text{perimeter}^2}\right]$$

A value of 1 indicates a perfect circle.

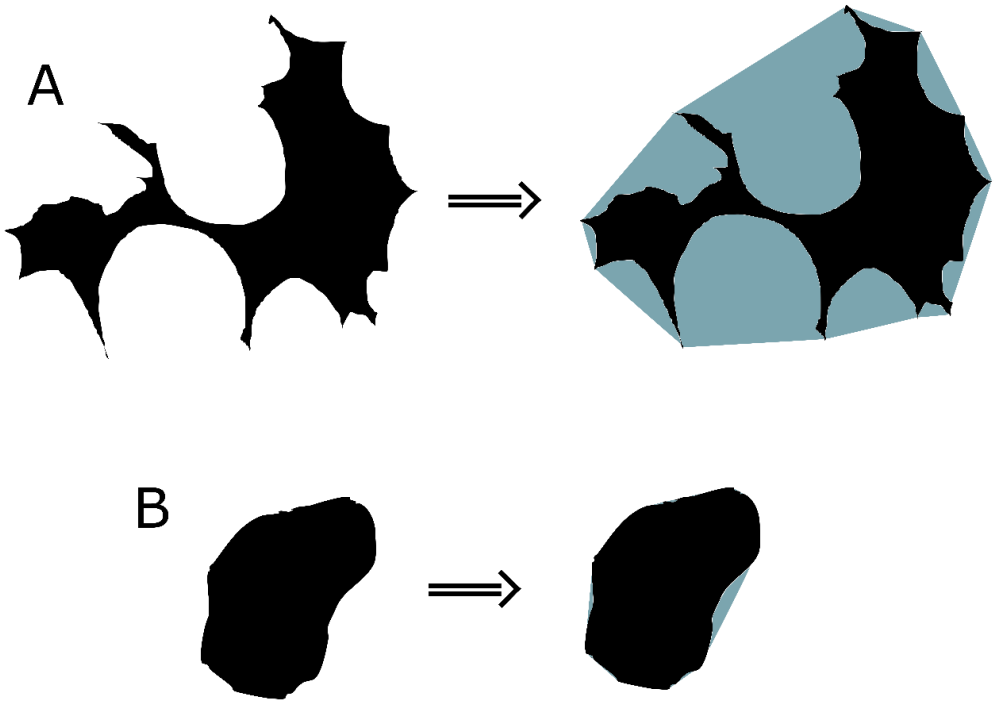

-

Figure 2.4 Left hand side images represent clast outlines for A) Zone D material and B) Zone A material, right hand images represent the convex hull area (shown in blue) for both geometries. The highly angular Zone D material has a greater convex hull area than the well-rounded Zone A material.

2.3 Experimental Work

2.3.1 Experimental Aims

Experiments were designed to constrain material responses to stress in terms of micromechanics and microstructure. Experiments were run using a LHVR to shear powdered Green Mountain basaltic scoria. Material composition, powder size and weight were kept constant. Experimental variables were velocity (m/s), powder saturation (saturated or room dry), and normal load (MPa).

Raw data from the experimental apparatus were used to determine velocity strengthening or weakening behaviour; these are key mechanical properties which indicate frictional response to velocity change. Experiments were run at low and high velocity configurations to mimic slip nucleation and propagation respectively.

Therefore, by changing the variables, velocity strengthening or weakening behaviour can be constrained and the effect of saturation, normal pressure and velocity on this behaviour can be determined.

The experimental run products were used to investigate microstructures, which were observed later through SEM imaging. The formation of a PSZ, and other microstructural differences from the unsheared powder act as evidence for shear localisation and represent the physical accommodation of mechanical stress.

The mechanical processes replicated in the experiments represent the processes which may have occurred during the formation of the GMSZ. Ultimately, investigating these processes can help to build a more robust approximation of collapse-scale dynamics during the Green Mountain collapse.

2.3.2 Experimental Method

Samples of Green Mountain Scoria were oven dried at 120°C for two hours and were hand-crushed for use in experiments. Smaller fragments were then ground in a pestle and mortar. The material was sieved and the 90-125 µm fraction was separated into 1g samples (Figure 2.5).

The optimum particle diameter size for use in the experiments is 90-125µm gouge. Coarser grained would damage the machinery and finer grained material would be less representative of the natural material. One gram of the powder was spread evenly across in a hollow, 2.5 cm diameter cylinder made of a titanium-aluminium-vanadium alloy ($Ti_{90}Al_6V_4$) with Teflon confinement seals to reduce material expulsion during shearing (Figure 2.6).

Figure 2.5 1g of sieved, unsheared powdered Green Mountain scoria before shearing.

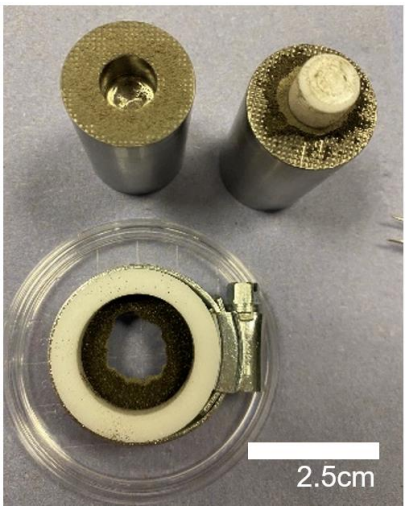

Figure 2.6 Titanium-aluminium-vanadium alloy confinement cylinder and Teflon ring which powder is sheared in.

Experiments were conducted on the LHVR in the Rock Mechanics Laboratory at Durham University. The LHVR is encased in steel housing and consists of two vertical shafts that meet in the middle, where the sample is placed (Figures 2.7, 2.8). The top shaft rotates at a given velocity and the lower shaft remains stationary. In the experiments presented herein, the revolving speed of the shaft ranges from 1.3µm/s to 1.3m/s (as measured from the centre of the sample ring). Vertical axial displacement is measured by a transducer at the base of the lower shaft and axial load is applied to the bottom shaft via a pneumatic piston. Torque values are obtained by two compression load cells which are fixed to the lower shaft, axial displacement values are measured using a high sensitivity displacement gauge, and revolution speed and cumulative number of revolutions are measured by a tachometer and pulse counter. Before each experiment, the alignment of the upper shaft was checked using a mechanical shaft alignment tool to ensure that during rotation, pressure would be evenly applied to the sample holder.

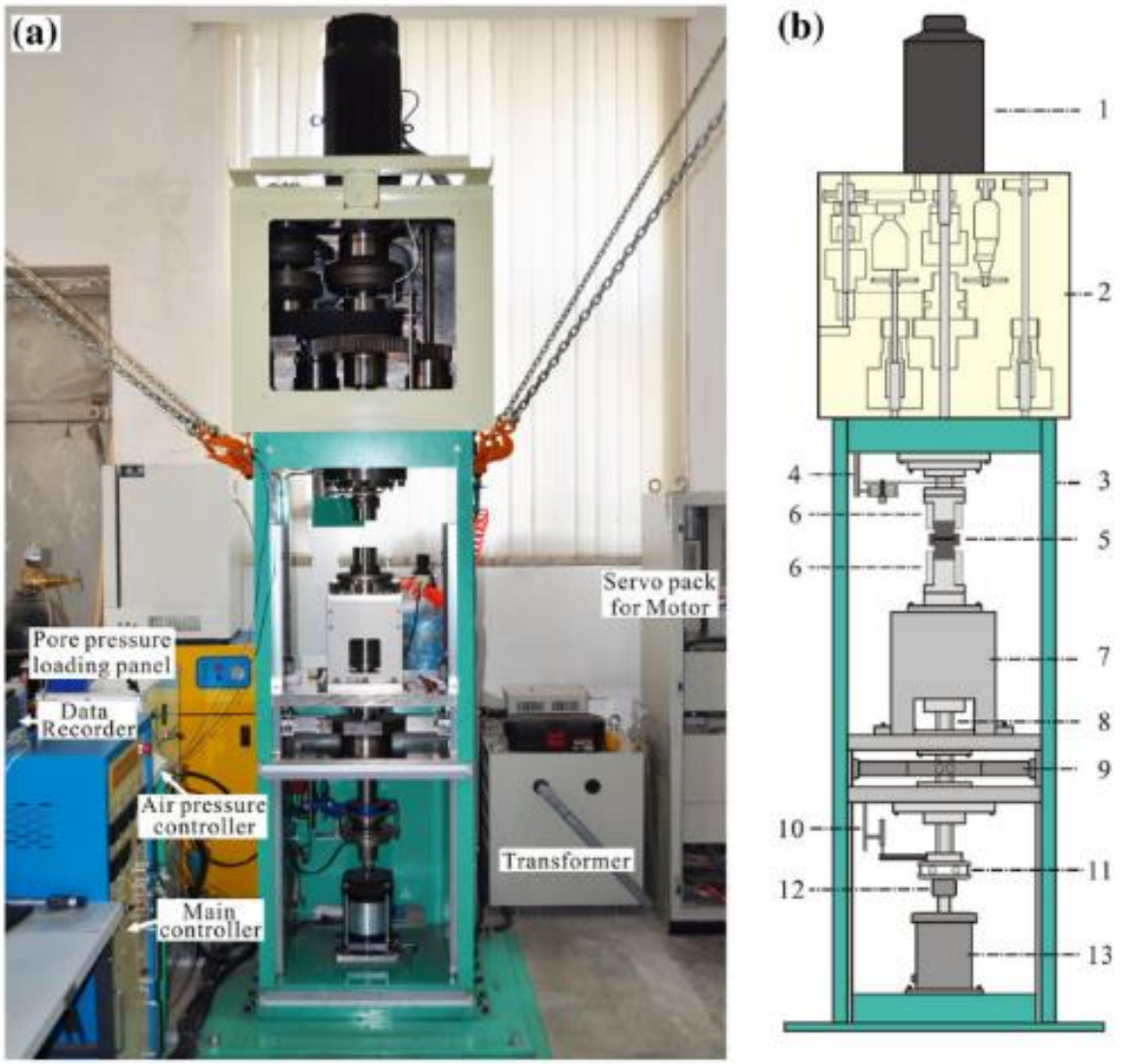

Figure 2.7 a) Photograph of low to high velocity rotary shear frictional testing machine (LHVR) at Institute of Geology, China Earthquake Administration, b) A schematic diagram of the main components of the apparatus: 1. Servo motor, 2. Gear/belt system for speed change, 3. Loading frame, 4. Rotary encoder, 5. Specimen assembly, 6. Locking devices of specimens, 7. Frame for holding the lower loading column, 8. Axial loading column, 9. Torque gauge, 10. Axial displacement transducer, 11. Thrust bearing, 12. Axial force gauge, 13. Air actuator (Ma et al., 2014).

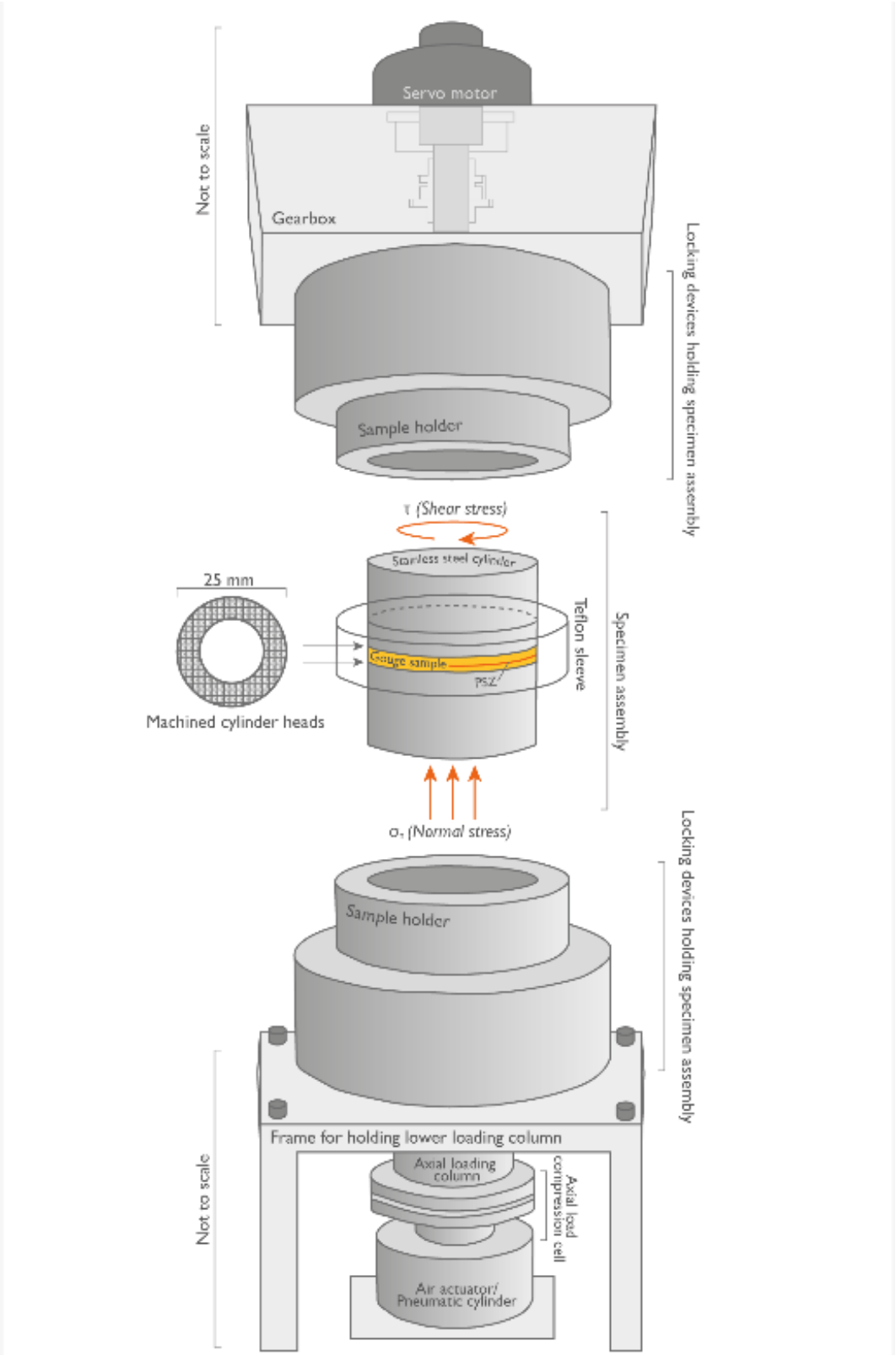

Figure 2.8 Components of the rotating shaft and sample holder inside the low to high velocity rotary shear apparatus (Robertson, 2021).

The constant parameters for the experiments were the material composition (Green Mountain basaltic scoria), the gouge particle diameter (sieved to 90-125µm), and the weight of powder used for each experiment (1g). The variable parameters were whether the experiments were run at seismic (>1m/s) or sub-seismic (<1m/s) velocities, whether the normal load was 1MPa or 2MPa, and whether the experiments were run at room humidity or saturated and drained conditions.

The sub-seismic (low velocity) experiments were designed to simulate slip nucleation. These were based on a nine-step system covering velocities from 1.3µm/s, to 130µm/s, to 1.3mm/s, to allow the material to reach steady state at each step. The sub-seismic experiments ran for 720 seconds with a total slip distance of 81.9mm (See Figure 2.9). The seismic (high velocity) experiments were designed to investigate slip propagation and ran for 2 seconds with a velocity of 1.3m/s and total slip distance of 2.6m (see Figure 2.10).

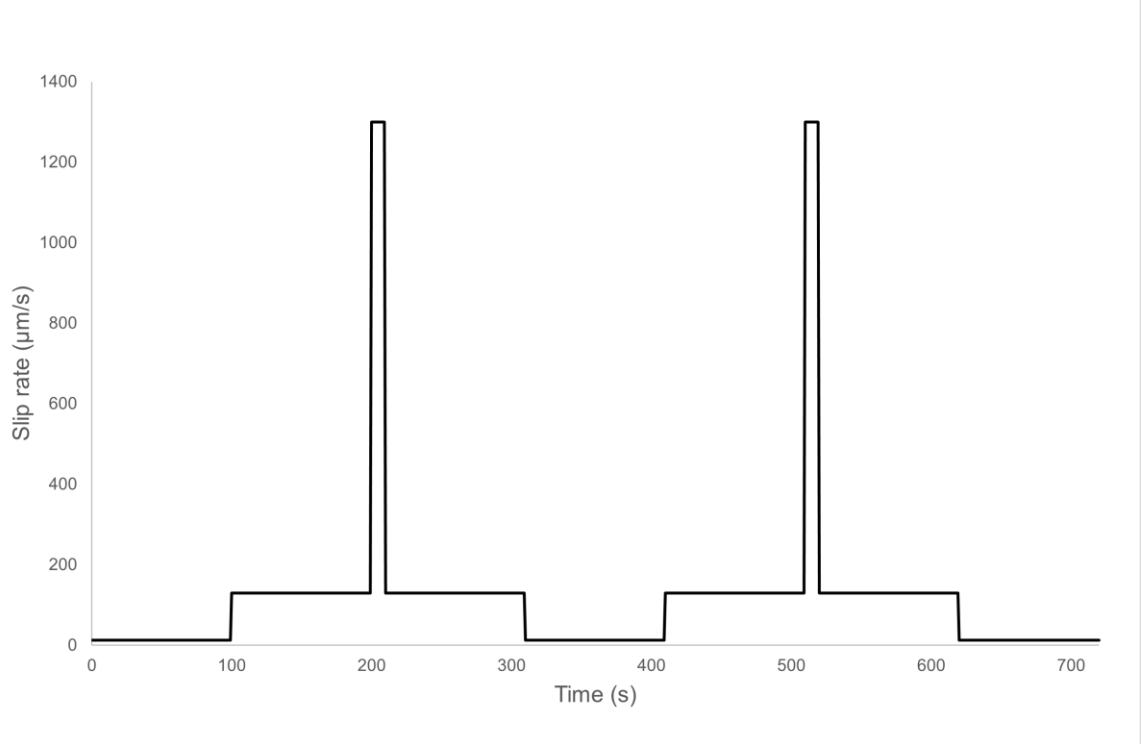

Figure 2.9 Velocity stepping experiment used for sub-seismic experimental runs.

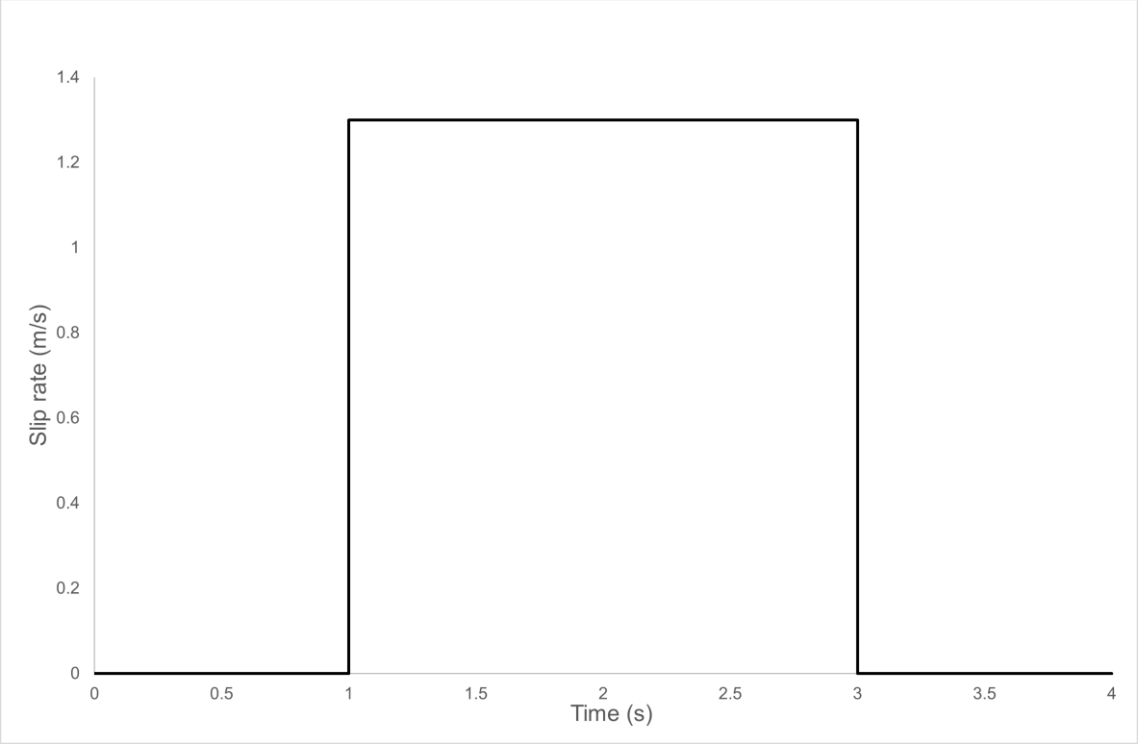

Figure 2.10 Seismic velocity experimental runs were conducted at 1.3m/s slip for 2s.

Experiments were run at both 1MPa and 2MPa normal load. 1MPa is the lowest normal load at which the apparatus can take measurements at a clear resolution. Ideally, the experiments would run below 1MPa to better replicate the normal pressure at the base of a volcanic debris avalanche, which is often calculated to range between 0.3-0.7MPa (Davies et al., 2010). The 2MPa runs were designed to investigate the role of increased normal load on microstructural and mechanical behaviour. For the saturated experiments, four drops of deionised water were added to the top of the powder. Saturated experiments were designed to investigate the role of water and any relation to velocity weakening or velocity strengthening behaviour.

For simplicity, experiments are hereafter referred to in a four-digit code corresponding to seismic (high) velocity or sub-seismic (low) velocity (HV or LV), the normal pressure used (1 or 2MPa) and whether the experimental run was saturated or under room humidity conditions (S or R). For instance, code LV1S refers to the low velocity, 1MPa saturated run. See Table 2.1.

Table 2.1 Code system for experimental runs conducted

	1MPa Saturated	1MPa Room humidity	2MPa Saturated	2MPa Room humidity
Sub-seismic (low velocity) 1.3µm/s -1300µm/s	LV1S	LV1R	LV2S	LV2R
Seismic (high velocity) 1.3m/s	HV1S	HV1R	HV2S	HV2R

2.4 Experimental Outputs

2.4.1 Experimental Run Products

Following shearing, the sample cylinder was carefully dismounted, and the sheared gouges recovered. More consolidated fragments were recovered first and placed in a dish, and then the loose powder was collected. The sheared samples retrieved varied in compaction and competency (see Figure 2.11).

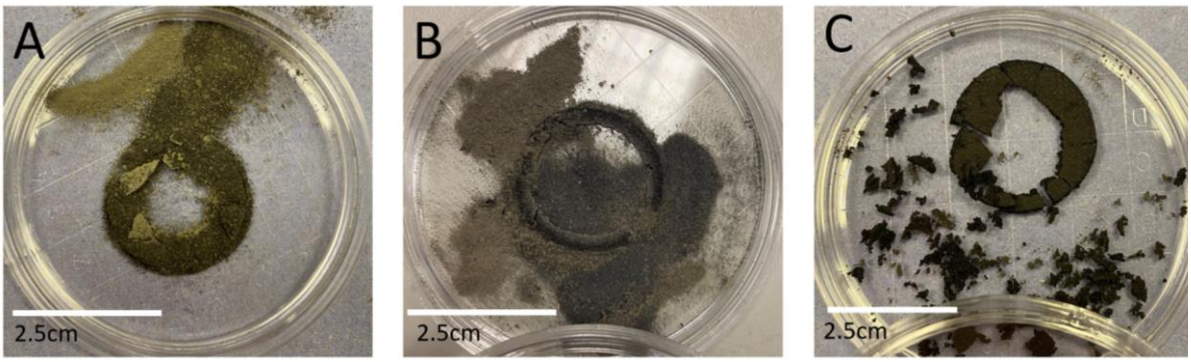

Figure 2.11 Retrieved samples varied in compaction. A is composed of very loose powder and only a few chips of hardened sheared material, B is slightly better consolidated and C is well consolidated, making retrieval easier.

The samples were laid at the bottom of a cylindrical capsule and covered with superglue to impregnate and stabilise the material (Figure 2.8). Epoxy resin was then poured into the capsule and left to solidify. This block of epoxy was then cut at a slightly oblique to perpendicular angle to the shear zone. This was then re-cast in epoxy resin, left to set, and dry polished to mitigate the loss of material.

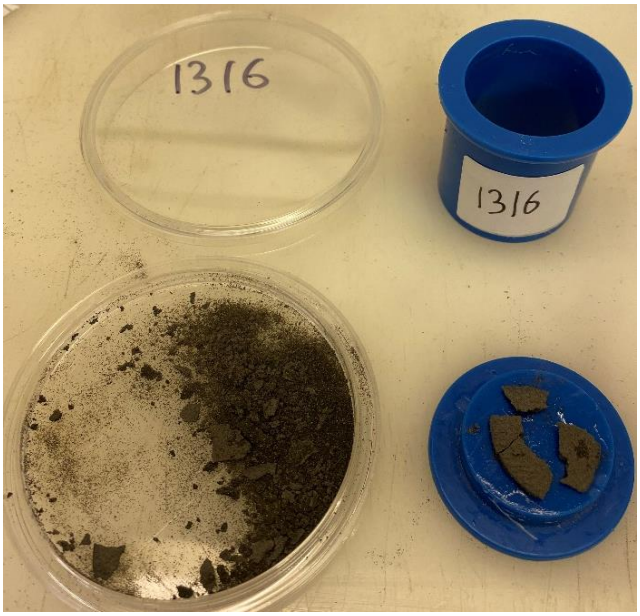

Figure 2.12 The chips of shear zone were taken from the retrieval dish (left) and superglued on to the base of a cylindrical capsule that was then filled with epoxy resin (right).

Due to the fragile nature of the experimental run products , some of the microstructures may have been disturbed with the removal of the normal load, when being recovered from the LHVR or when being impregnated with resin and polished.

2.4.2 Mechanical Data

The raw data outputs from the LHVR, time (s), axial load (kN), axial displacement (mm), torque (Nm), rotation angle (degrees), revolution rate (angular speed) and cumulative rotation, were run through a MatLab script (Dawood, 2021). The outputs of this script are slip rate (m/s), cumulative displacement (m), normal stress (MPa), shear stress (MPa), axial displacement (mm), and friction coefficient. These parameters are used to show relationships between variables for each experimental runs, as described below.

2.4.2.1 Mechanical Data Analysis: Sub-Seismic Velocity Experiments

Rate and state calculations to determine velocity weakening or strengthening behaviour were conducted in accordance with established methodology (i.e. Marone, 1998) using the equation:

$$a\text{-}b = (u2 - u1) / \ln (V2 / V1)$$

Where:

V1 = velocity before step (µm/s)

V2 = velocity after step (µm/s)

u1 = steady state friction at V1

u2 = steady state friction at V2

Note that:

$$u1 = s/sn$$

Where:

s = shear stress (MPa)

sn = normal stress (MPa)

Material is velocity weakening if *a-b* is <0 or velocity strengthening if *a-b* is >0. The *a-b* values for each of the sub-seismic experiments were plotted against one another for comparison.

2.4.2.2 Mechanical Data Analysis: Seismic Velocity Experiments

For analysis of the seismic velocity experimental data, key data were taken from each experimental run and plotted against one another. The data extracted from each experiment were peak friction, steady state friction and the friction at the end of the experiment. From this, the slip weakening distance could be calculated using:

$$\boldsymbol{slip\ weakening\ distance\ (m)} = \boldsymbol{slip\ at\ peak\ friction\ (m) - slip\ at\ steady\ state\ friction\ (m)}$$

2.5 Grain Size Analysis – Laser Granulometer

A 3g sample of 90-125µm Green Mountain scoria gouge was run through a Beckman Coulter LS13 320 Laser Granulometer (LG) using the Fraunhofer optical model to compare grain size distributions before and after shearing at 1MPa, room humidity

conditions for 2 seconds at 1.3m/s (the same experimental set up as HV1R). The optimum mass of scoria to use in the instrument to get the most accurate readings was 3g. The statistics derived from this include the mean, median, mode, mean/median ratio, skewness, kurtosis, standard deviation, variance, coefficient of variation, D_{10} , D_{50} and D_{90} of the dataset.

A challenge presented in this process was deciding how best to process particles in the LG, shear the sample using the LHVR, and then process them again through the LG. The same 3g sample was compared before and after shearing for the most representative results. This was challenging, firstly, because the optimum amount of powder to use in the LG is 3g, and the LHVR can only process 1g at a time. This was overcome by reclaiming the 3g of material after it had been run through the LG, then separate this into three 1g samples for use in the LHVR. This separation was done using the coning and quartering method. The three samples were then recombined post-shearing and processed through the LG again to observe any change in grain size distribution. An important consideration here was when looking at the post-shear grain size distribution results to assess how much of this change may be due to powder loss within the shearing process or powder reclamation process, as opposed to the direct results of the shearing itself. Secondly, this method was challenging because recovering the material from the LG involves retrieving the three grams of powder from ~10 litres of water. To do this, the mixture was left to allow the particles to settle out of suspension, the time required to do this was calculated using Stokes law. After the particles had settled to the bottom of two five-litre beakers, the clear water was siphoned off. This left 3 litres of water containing 3g of powder. This mixture was left to settle and the siphoning process was repeated until a damp powder was left and the remaining water was left to evaporate at room temperature until the powder was completely dry.

Limitations to work done with the LG may have skewed results towards coarser post-shearing particle distributions than is accurate. During the retrieval of the sheared powders from the LHVR, very fine powder was lost to the surrounding atmosphere. Additionally, the shear zones that was generated during the experiments are more consolidated and become indurated. Thus, rather than being recorded in the LG as separate, smaller clasts, in-tact parts of the shear zone were recorded as larger, single clasts. This means the data are slightly misrepresentative, and the true values that

would have incorporated these finer grains would have been skewed towards finer values. Another issue was the loss of powder during the process from measuring pre-shearing sizes, retrieving the powder from the LG, shearing it, and retrieving it again. Although high, retrieval rates were <100%.

Chapter III: Results

3.1 Green Mountain Collapse Deposit: Field Geometry

The Heim's ratio, or height/length (H/L) ratio, of this deposit is 0.18, based on a vertical drop of 360m and runout of 2000m. It must be noted that the error on this calculation is high, ± 200, as the detachment surface of the collapse is unclear, and the deposit was stopped at its base by a lava dome; runout may have been longer had this not been the case. Based on the same measurements, the horizontal runout of this collapse is 5.5x that of the vertical drop height.

3.2 Green Mountain Collapse Shear Zone

The Green Mountain shear zone (GMSZ) is a cohesive, non-foliated 1-2cm thick band at the base of the Green Mountain scoria fall deposit. Several zones have been identified within the GMSZ based on gradational changes in grain size, shape, sorting, angularity, roundness, matrix-to-clast ratio, porosity and interconnectivity, and rock texture (clast or matrix-supported) which are observed with depth perpendicular to the shear zone (see Figure 3.1, 3.2, 3.1 Table 3.1). The zones lie horizontally parallel to one another, and all changes are gradational. These are Zones A, B, B', C, C', D, D', E and E' (Figure 3.1). These zones are mirrored either side of Zone A, the PSZ, in regard to porosity, clast size, clast circularity and solidity. The terms 'jigsaw-fit' and 'jigsaw-crack' hereafter are used in reference to clasts found within the shear zone. The description is the same of those found in VDADs, but these are on a much smaller scale. Jigsaw-fit cracks and the abundance of scoria clasts with large internal vesicles also vary throughout the shear zone.

With distance from Zone A, the PSZ at centre of the shear zone, towards the basal contact, zones are labelled B' to E' and toward the upper contact are labelled Zones B-E. Zones D and D', the material on the periphery of the shear zone (Figures 3.1, 3.3). Zone E and E' represent the clasts immediately outside of the shear zone where the clasts were too large to be observed by SEM methods and were measured by hand. There is minor variability between zones above and below Zone A, but key parameters are well-mirrored. As such, there are no defined tops or bases for each zone. The shear zone varies in thickness between 1-2cm, meaning each zone is ~1.3-3.0mm in depth.

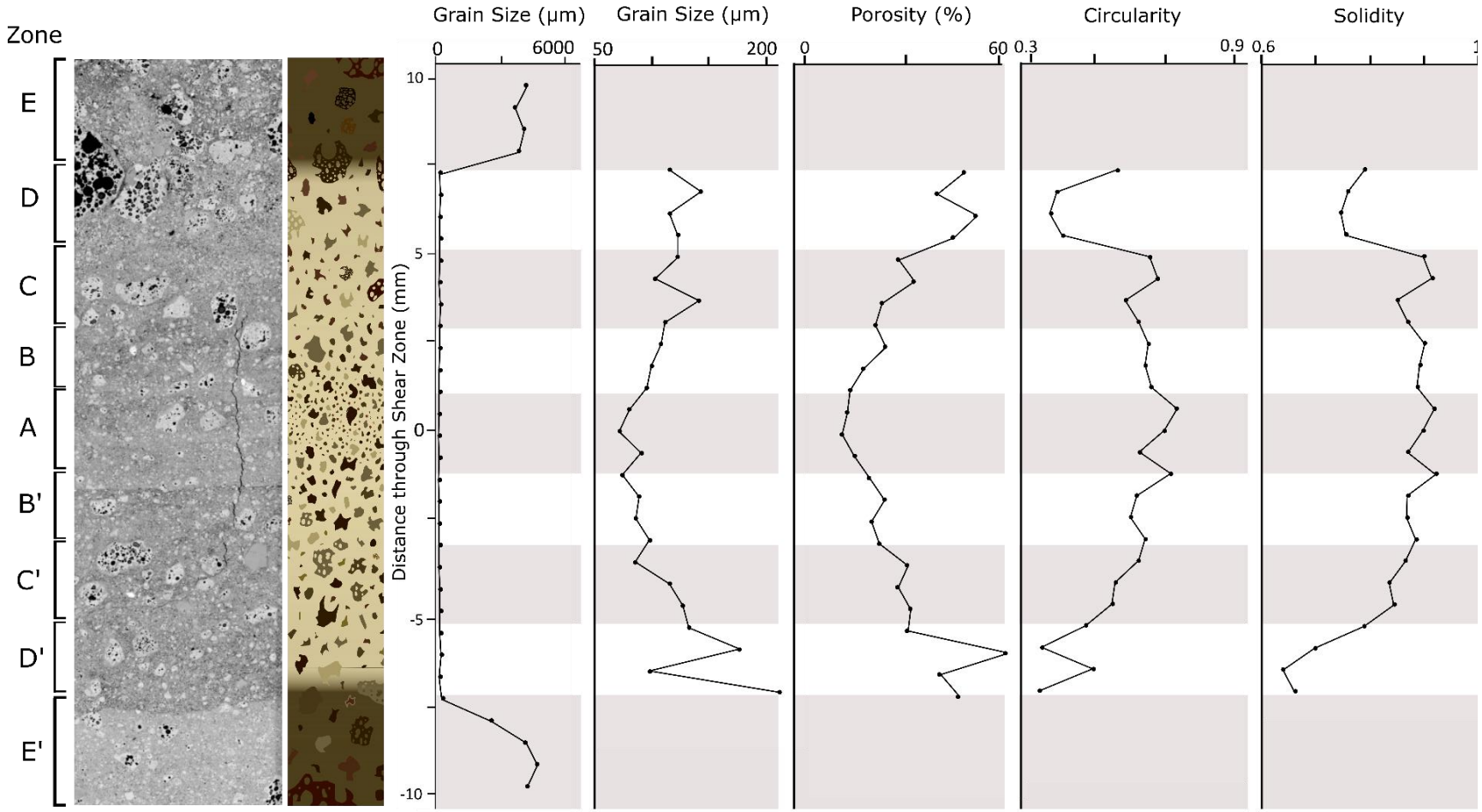

Figure 3.1 SEM image of shear zone (left) and infographic (right) demonstrating locations of zones A-E and A-E' and corresponding changes in average grain size of the 25 largest clasts including zone E and E' (n=33), average grain size of the 25 largest clasts excluding Zone E and E' (n=25), porosity (n=25), clast circularity (n=25) and clast solidity (n=25).

Table 3.1 Key data demonstrating variability with depth throughout the GMSZ

Zone	E'	D'	C'	B'	A	B	C	D	E
Grain size avg. of 25 largest clasts (µm)	3770	154.16	107.08	88.32	79.74	104.15	120.28	122.35	3800
Maximum grain size (µm)	7000	458	336	355	354	535	892	457	4033
Mean porosity (%)		45.28	29.36	20.5	12	19.32	27.03	46.7	
Maximum porosity (%)		63.2	31.04	22.5	17.48	109.4	32.27	52.77	
Miniumum porosity (%)		30.12	26.93	18.19	8.45	97.44	21.67	39.9	
Mean circularity of 12 largest clasts		0.418	0.581	0.626	0.692	0.645	0.645	0.438	
Maximum circularity of 12 largests clasts		0.498	0.629	0.648	0.738	0.657	0.683	0.568	
Minimum circularity of 12 largest clasts		0.344	0.553	0.606	0.631	0.629	0.591	0.376	
Mean solidity of 12 largest clasts		0.699	0.852	0.878	0.903	0.893	0.892	0.766	
Maximum solidity of 12 largest clasts		0.792	0.869	0.889	0.926	0.905	0.919	0.793	
Minimum solidity of 12 largest clasts		0.641	0.839	0.872	0.874	0.874	0.854	0.749	

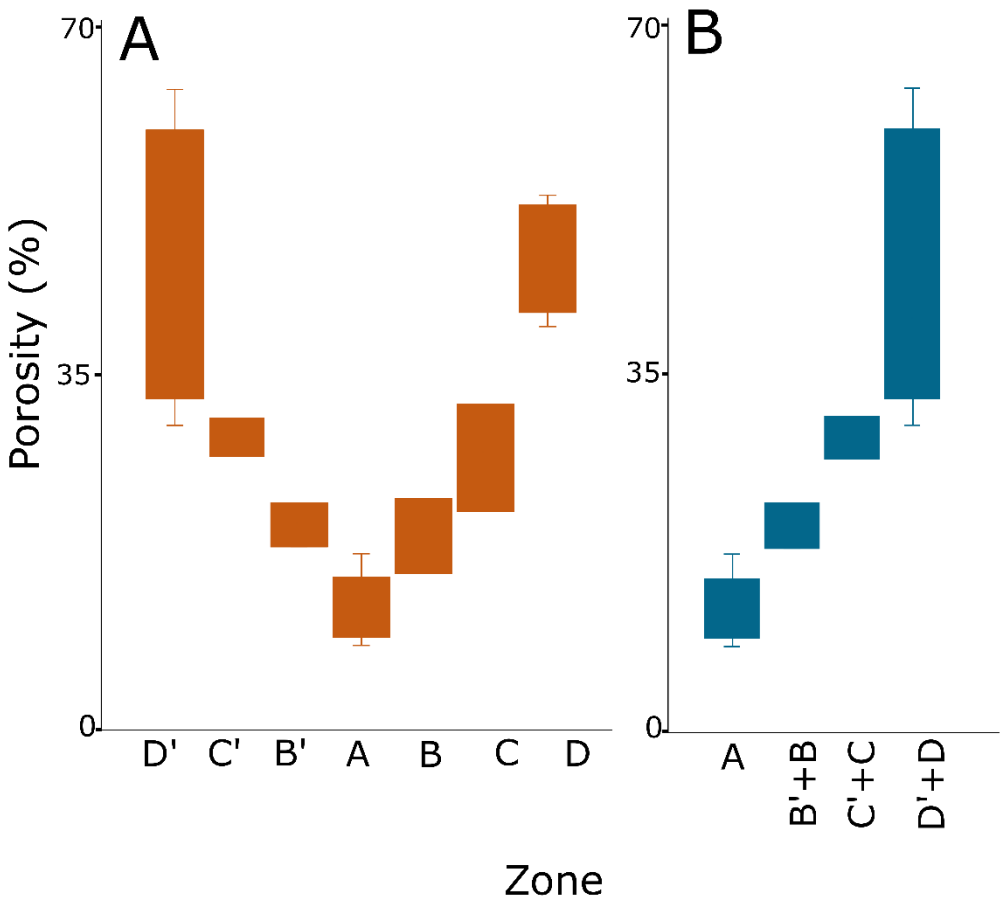

Figure 3.2 A) Box plot of porosity for each zone demonstrating that lowest values are observed in Zone A and porosity increases to ward the perimeter of the shear zone in Zones D and D', B) Box plot of porosity for combined zones mirrored either side of Zone A.

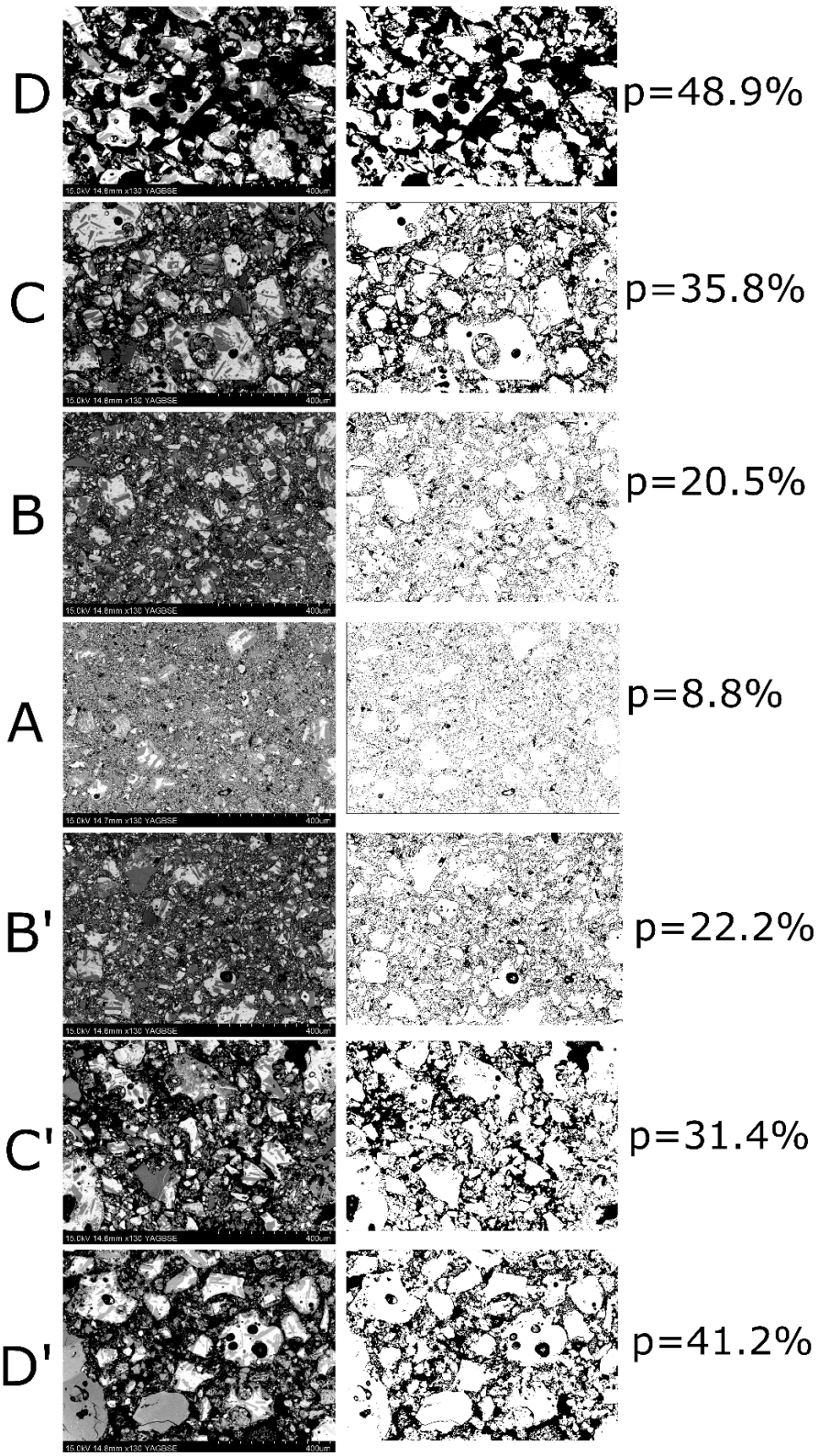

Figure 3.3 (Left) Images representative of each zone of the natural shear zone showing changes in clast size, shape, and porosity, (Right) Binary processing of images on left as used in Fiji with white corresponding to clasts and black to pore space, porosity values for each image are shown on the far right.

3.2.1 Zones E and E': Unsheared large clasts directly outside of shear zone margin

Zone E and E' clasts are observed on slide scale and lie directly outside of the sheared material. The average grain size of the ten largest clasts lies between 2.5-4.5mm with an average of 3.7mm and maximum grain size of 8.7mm. There is a step-change in the size of clast between Zones D and E and D' and E' (Figure 3.1).

3.2.2 Zones D and D': High porosity, clast-supported, vesicular, and angular scoria

Zone D and D' are predominantly comprised of scoria clasts that have undergone weak shearing. These lie on the periphery of the shear zone and the original fabric and texture of the scoria deposit are better preserved (Figure 3.4, A-C). Of the images analysed across Zone D and D', the average size of the 25 largest clasts is 138μm, with a maximum value of 457μm (see Table 3.1). There are scattered free plagioclase crystals, scoria clasts and crystal fragments are clast supported with no matrix material present. Pore interconnectivity is visibly evident as both zones D and D' have a low matrix to clast ratio. Porosity ranges between 30-63% with an average of 45%.

The scoria clasts are angular and there are large, intact, internal vesicles within scoria clasts where the vesicle walls are thin but remain unbroken (Figure 3.4, D-H). Many of these clasts exhibit concave, semi-circular boundaries with thin spines either side, representing vesicle wall fragments, hereafter referred to as 'vesicle-defined boundaries' (Figure 3.4, A-C). Circularity ranges between 0.35-0.57 and solidity between 0.66-0.8 with averages of 0.43 and 0.73 respectively. Jigsaw-crack clasts exhibit thin fractures which have not been offset or infilled by material (Figure 3.4, I).

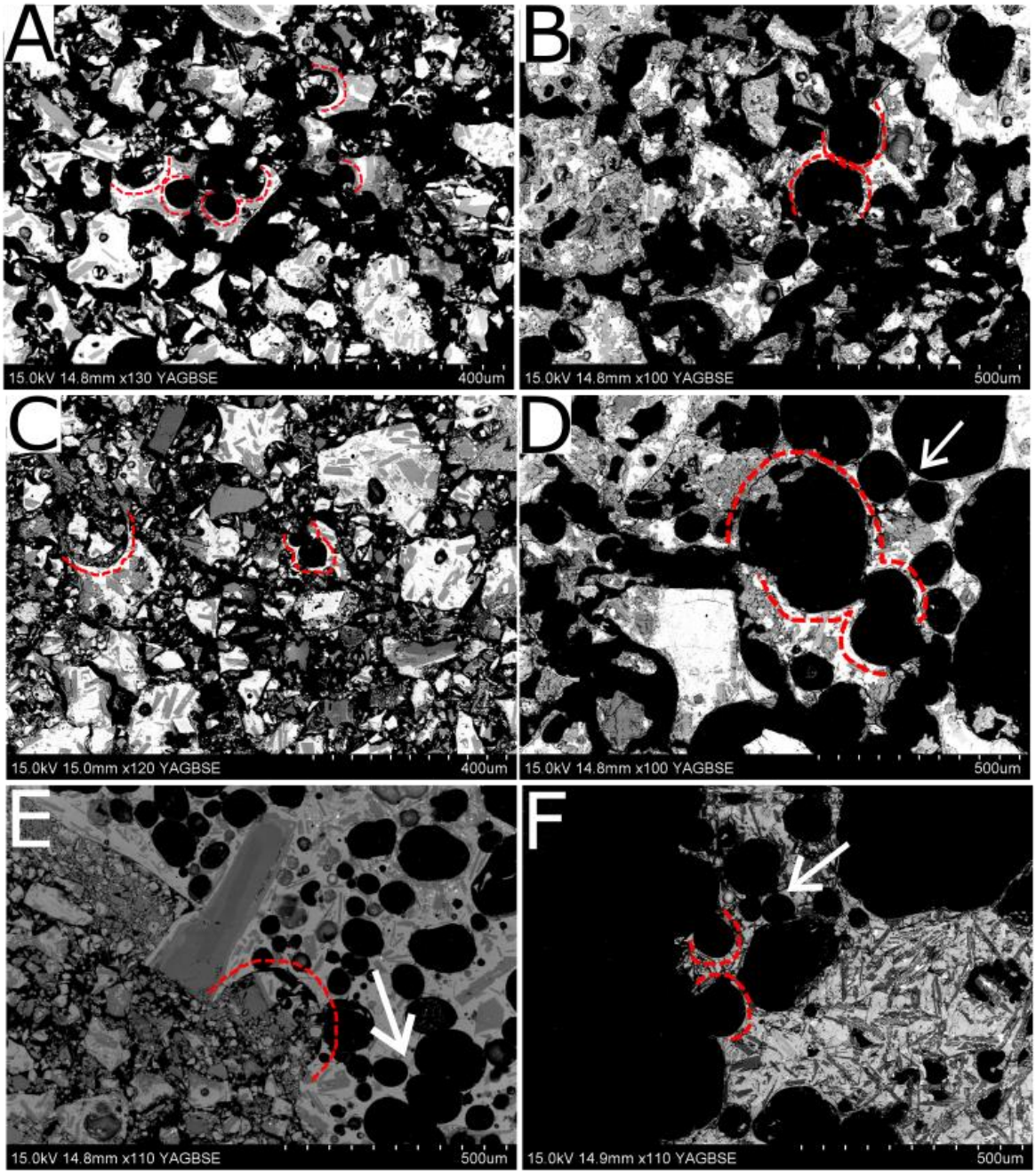

Figure 3.4 [A, B, F, G are from Zone D; C, D, H, G and I are from D'] A-B) Images showing overall microstructure of Zone D including high proportion of pore space, clast supported material, lack of matrix material and highly angular clasts, A-F) Red dashed lines indicate 'vesicle defined boundaries' where clast edges are defined by broken vesicles, often these show thin, delicate spines, D-H) Arrows indicate vesicles with thin vesicle walls which remain preserved and unbroken.

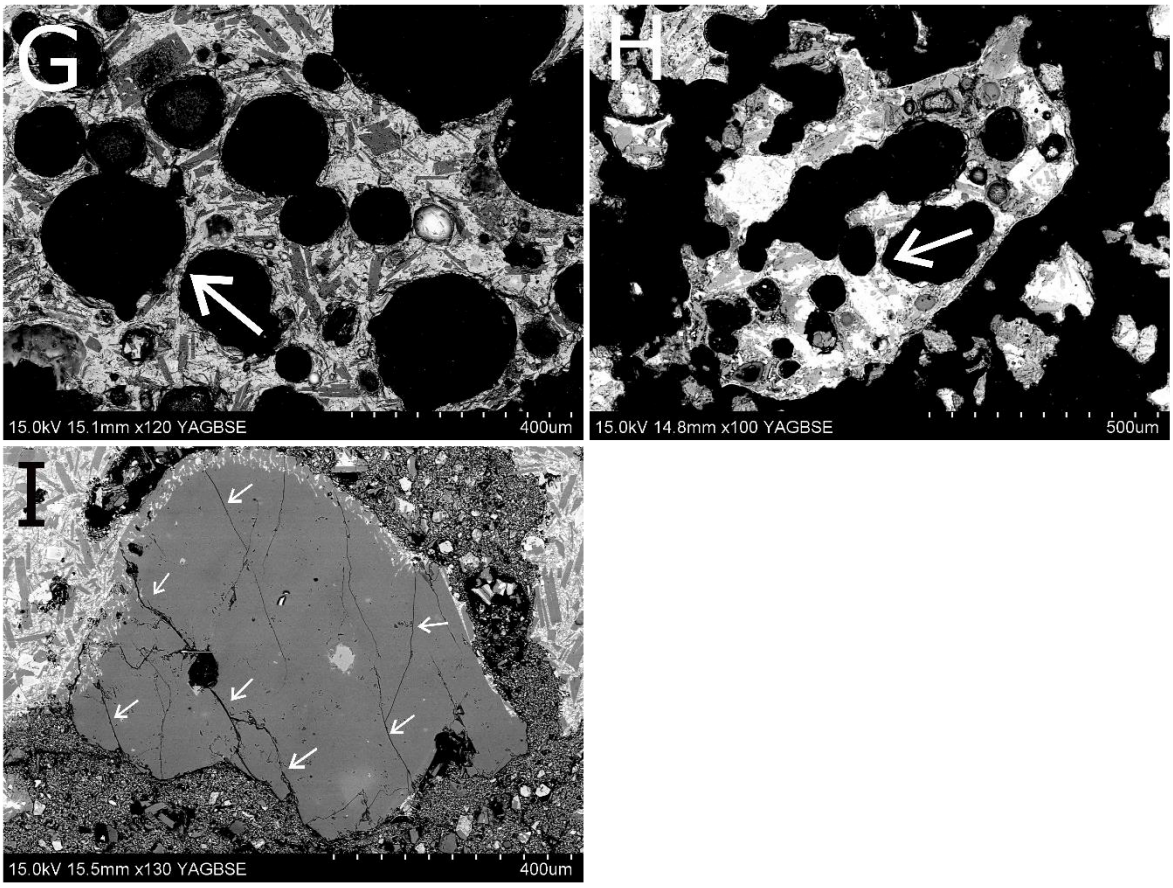

Figure 3.4 I) Arrows indicate jigsaw-cracks on a ~800µm sub angular clast; the clast has not disaggregated, and the cracks are not offset in any direction, note that this clasts is close to Zone C, hence the higher proportion of finer matrix surrounding it.

3.2.3 Zones C and C': Clast-supported, intermediate porosity, angular to sub-angular scoria

Zones C and C' lie between Zones D and D', and B and B'. Subsequently, clasts exhibit stronger evidence of crushing and shearing than Zones D and D'. Matrix material is <5µm and of the images analysed across Zone C and C', the average size of the 25 largest clasts is 113µm, with a maximum value of 892µm (see Table 3.1). Material is poorly sorted and there is a higher proportion of finer matrix material. Overall, clasts and crystal fragments remain clast- rather than matrix-supported (Figure 3.5, A-F). Pore interconnectivity appears markedly reduced as finer material infills space between clasts. Porosity ranges between 21-32% with an average of 28%.

There is a notable decrease in large, highly vesicular scoria clasts, with only a small proportion of clasts >100µm exhibiting intact, internal vesicles. These vesicles all have

thicker vesicle walls and very few of the vesicles are interconnected (Figure 3.5, A-D). Larger clasts remain sub-angular to angular and vesicle-defined boundaries are still present on some clasts but are more dulled with no thin spines (Figure 3.5, A,E,F). Circularity values range between 0.55-0.69 with an average value of 0.61 and solidity values range between 0.83-0.92 with an average value of 0.87. Jigsaw crack clasts are present are there is evidence of clast disintegration as cracks show offset and smaller fragments begin to migrate away from the parent clast (Figure 3.5, B,G,H). In the region of Zone C' which borders Zone B' there are truncated clasts along shear localisations (Figure 3.5, J-L). These are identifiable by a reduction in pore space above the boundary.

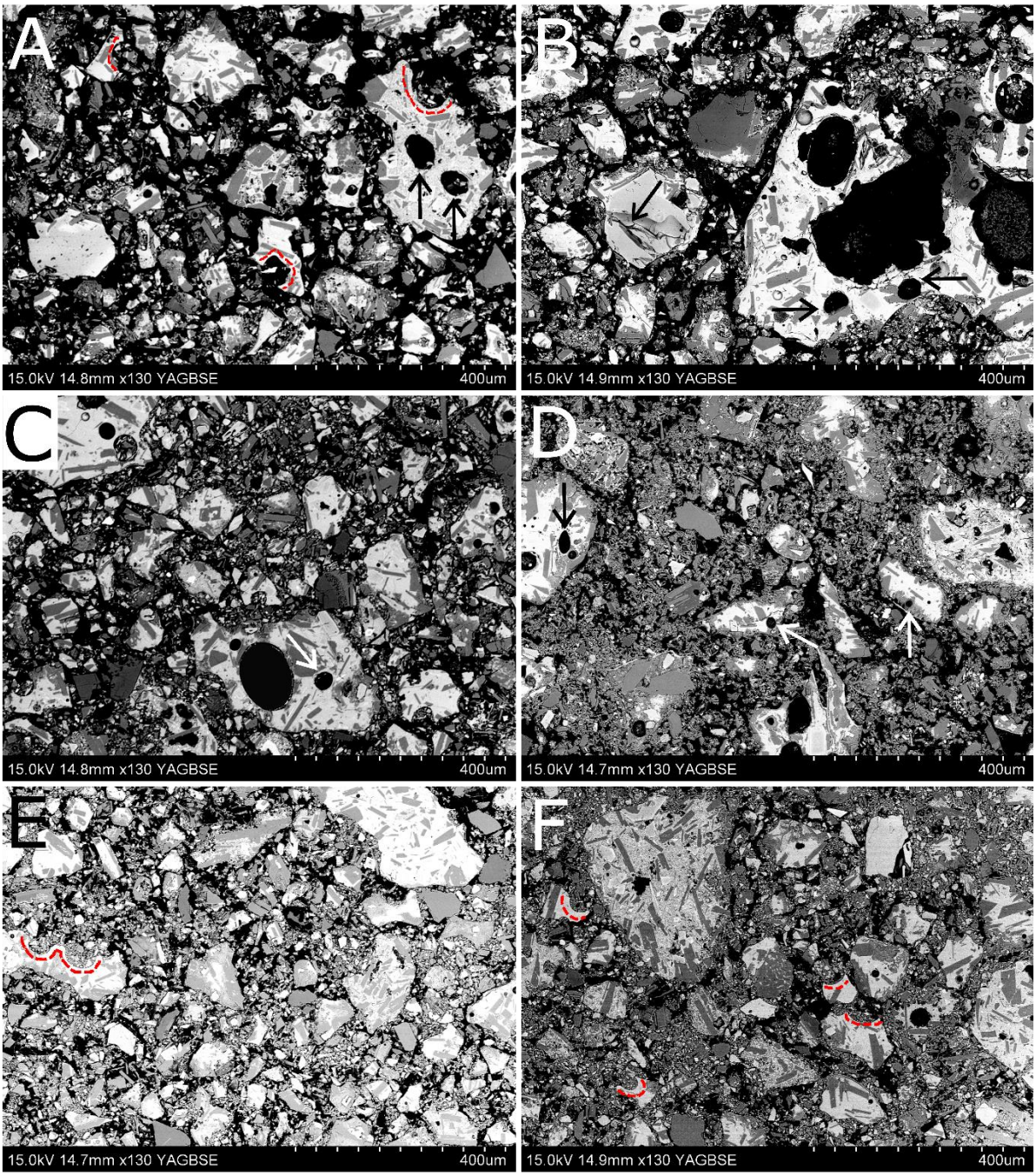

Figure 3.5 [A-C are from Zone C; D-L are from Zone C'] A-F) Images showing overall distinguishing microstructure including a reduction in pore space and grain size and increase in matrix material relative to D and D', A-D) Yellow arrows indicate internal vesicles of scoria clasts, these are smaller on average than in Zone D and have thicker vesicle walls, A, E, F) Red dashed lines indicate vesicle-defined boundaries, which are more dulled and do not have thin spines as observed in Zone D and D'.

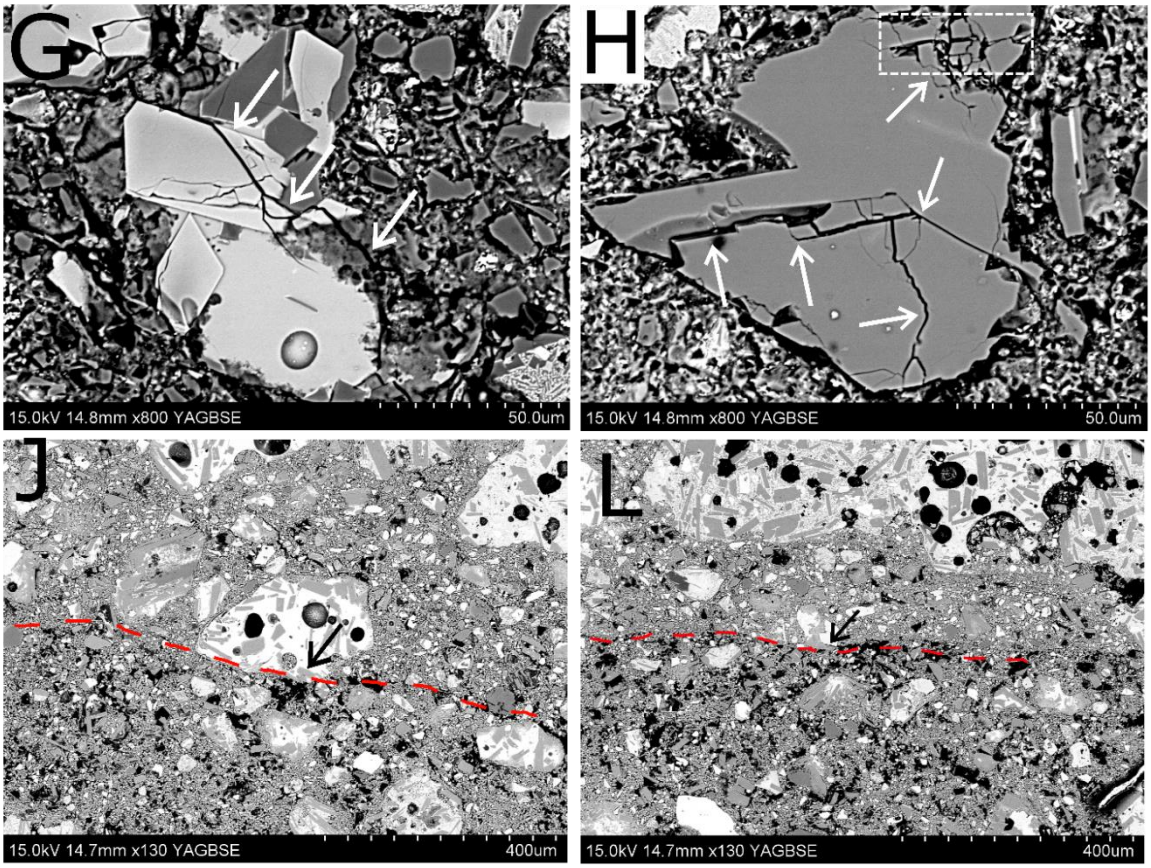

Figure 3.5 B, G, H) Arrows indicate jigsaw cracks on clasts, dashed box in H indicated where the boundary of the clast has started to disintegrate and migrate away from the parent clast, J,L) Red dashed lines indicate shear localisation along which clasts have been truncated, as indicated by black arrows.

3.2.4 Zones B and B': Low porosity, matrix-supported, sub-angular scoria

Zones B and B' exhibit evidence of relatively strong shearing. Zones B and B' are situated adjacent to the most sheared material of Zone A, the PSZ. Of the images analysed across Zone B and B', the average size of the 25 largest clasts is 113μm, with a maximum value of 535μm (see Table 3.1), and the clasts are overall poorly sorted (Figure 3.6, A-D). A higher proportion of matrix material, as fine as >1μm, which class as nanopartices (Figure 3.20), results in a visible decrease pore interconnectivity. Porosity lies between 15-22% with an average value of 19%. Most clasts >100μm are matrix-supported, and pockets of higher porosity are observed where finer material concentrates around the boundaries of larger clasts (Figure 3.6, B-E).

Scoria clasts and free plagioclase crystals are sub-angular to sub-rounded and vesicle-defined boundaries are present on some scoria clasts, but these are significantly dulled and rounded, with no thin spines (Figure 3.6, A). Some larger scoria

clasts exhibit intact internal vesicles, whcih have an average size of 25-40μm, thick vesicle walls, and very few of these vesicles are connected to one another (Figure 3.6, A-E). Circularity ranges between 0.6-0.64 with an average of 0.63 and solidity ranges between 0.87-0.91 with an average of 0.88. Jigsaw cracks are common on a range of clast sizes from ~60-300μm, with clasts showing varying stages of disintegration and offset along cracks, but no interstitial material between broken fragments (Figure 3.6, F-J). Sharp truncation of a free plagioclase clast is observed in Zone B' close to the boundary with Zone A and a change in porosity is observed either side of this boundary (Figure 3.6, K).

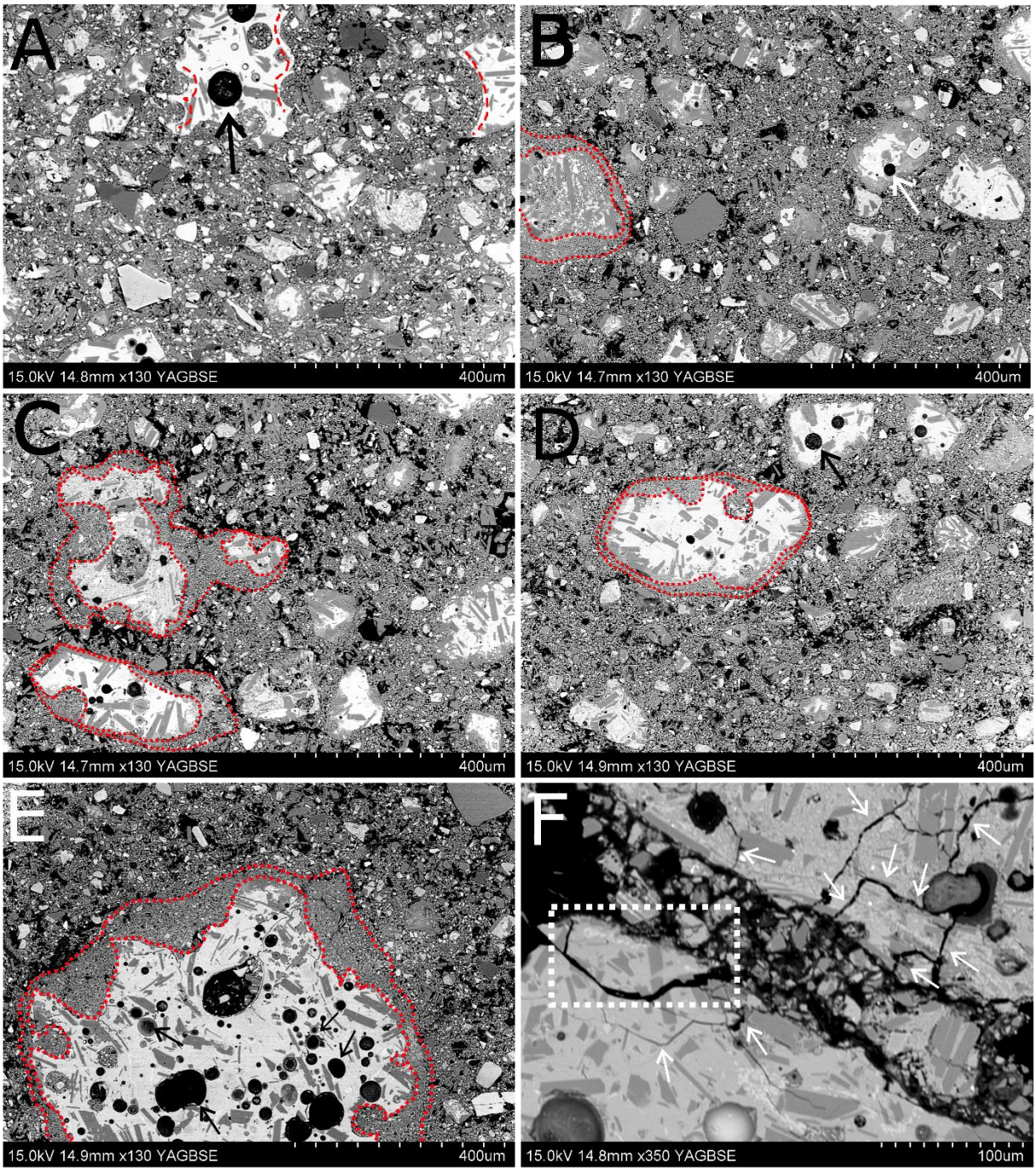

Figure 3.6 [A, B, D, G, H, I are from Zone B; C, E, F, J, K are from Zone B'] A-D) Images show overall microstructure of Zone B including a reduction in grain size and pore space, as well as increasing grain roundness, A, B, D, E) Arrows indicate internal vesicles in scoria clasts which are small with thick walls between vesicles, A) Red dashed lines indicate significantly dulled vesicle-defined boundaries with no thin spines, B-E) Red dashed lines indicate the outline of larger scoria clasts and the higher-density region of finer matrix material that surrounds them, creating localised pockets of higher porosity.

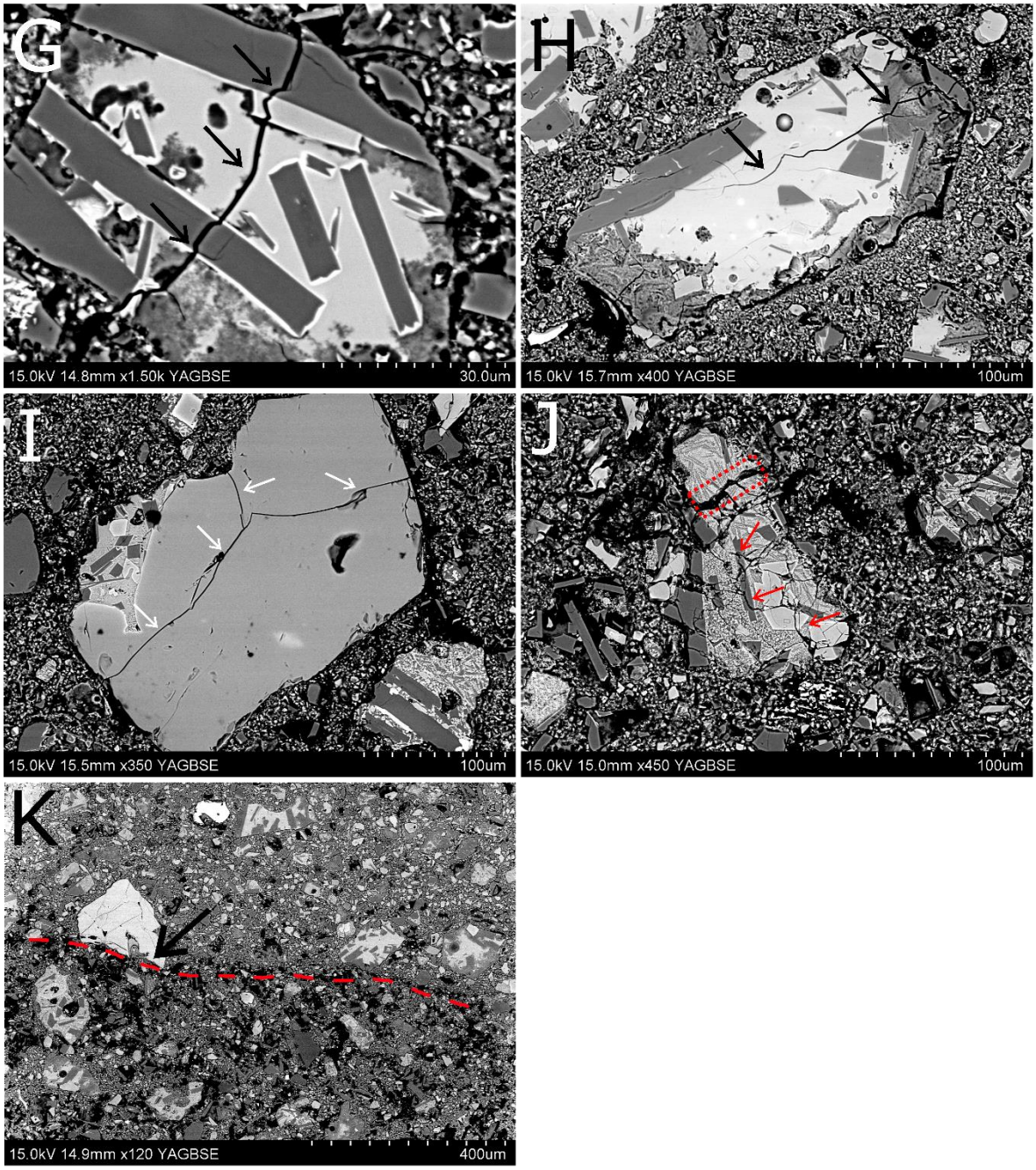

Figure 3.6 F-J) Arrows indicate jigsaw-fit cracks on clasts of various sizes, dashed boxes on F and J represent early stages of clast disintegration as broken fragments migrate away from each other, K) Red dashed line indicates shear localisation in Zone B' along which a plagioclase crystal, indicated by black arrow, has been sharply truncated.

3.2.5 Zone A: Very low porosity, matrix-supported, sub-rounded scoria

Zone A constitutes the most highly sheared and crushed scoria and plagioclase clasts at the centre of the shear zone. These physical properties and the data presented in Figure 3.1, specifically grain size and porosity distribution, suggest that Zone A is the PSZ, where most of the slip was accommodated during the collapse event.

Matrix material is as low as <1µm, classing as nanoparticles (Figure 3.20), and maximum clast diameter reaches 354µm. Of the images analysed across Zone A, the average size of the 25 largest clasts is 79µm (see Table 3.1). Clasts are poorly to moderately sorted as larger clasts are still present within the fine matrix. Clasts are fully matrix-supported (Figure 3.7, A-E). Matrix material is densely and uniformly distributed, rather than pockets of relatively high or low porosity. Pore interconnectivity appears very low owing to the high matrix to clast ratio. As such, porosity ranges between 8-17% with an average of 12%.

Scoria clasts and plagioclase crystals are sub- to well-rounded. There are very few clasts with vesicle-defined boundaries, those that remain are very poorly defined (Figure 3.8, C). There are very few scoria clasts containing vesicles; those that do have an average vesicle diameter of 5-30µm, thick vesicle walls, and interconnected vesicles within scoria clasts are infrequent (Figure 3.7, B,D). Jigsaw-fit clasts with interstitial material between fragments are present, as these fragments migrate away from parent clasts and voids are infilled with matrix during disintegration (Figure 3.7, E,F). Circularity values lie between 0.63-0.74 and solidity values between 0.87-0.93 with averages of 0.69 and 0.9 respectively.

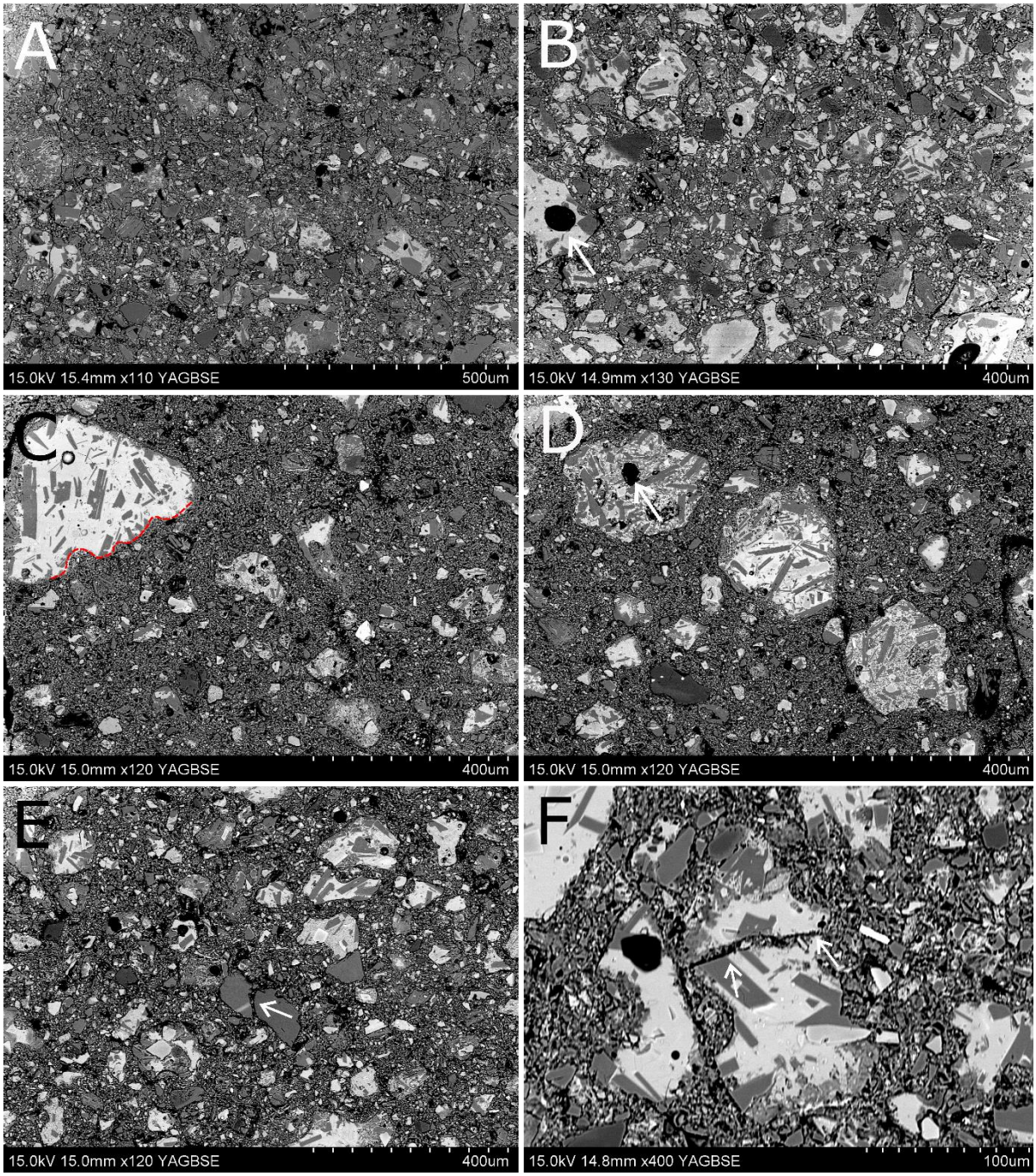

Figure 3.7 A-E) Images showing representative lithofacies of Zone A such as low porosity owing to a higher proportion of finer material, low average grain size compared to other zones, and well-rounded clasts, B,D) Yellow arrows indicate vesicles within scoria fragments, these are rare and are surrounded by thick walls, C) red dashed line shows a very dulled vesicle-defined boundary, E,F) Blue arrows indicate jigsaw-fit clasts, where interstitial material infills the gaps between fragments, most obvious in F.

3.3 Experimental Work

Mechanical data is presented for all experiments apart from LV2S, which was disrupted due to computer error. Microstructural data is presented for all experiments other than LV1R, which was too fragile to be retrieved and cast in resin.

3.3.1 Control Powder

1g of unsheared powdered Green Mountain scoria passed through a 90-125µm sieve mesh was used as a control powder (Figure 3.8, A). This represents the starting material for all subsequent experimental runs. There is no matrix material and clasts are wholly clast supported. Clasts larger and smaller than the mesh size still pass through, and as such the smallest clasts are ~25µm and the largest up to 170µm in diameter. Clasts range from sub-rounded to highly angular (Figure 3.8, B-C), with many exhibiting vesicle defined boundaries. There is a high level of porosity, and pore interconnectivity appears high. Clasts with larger internal vesicles measuring up to 70µm remain intact and there are no cracked clasts.

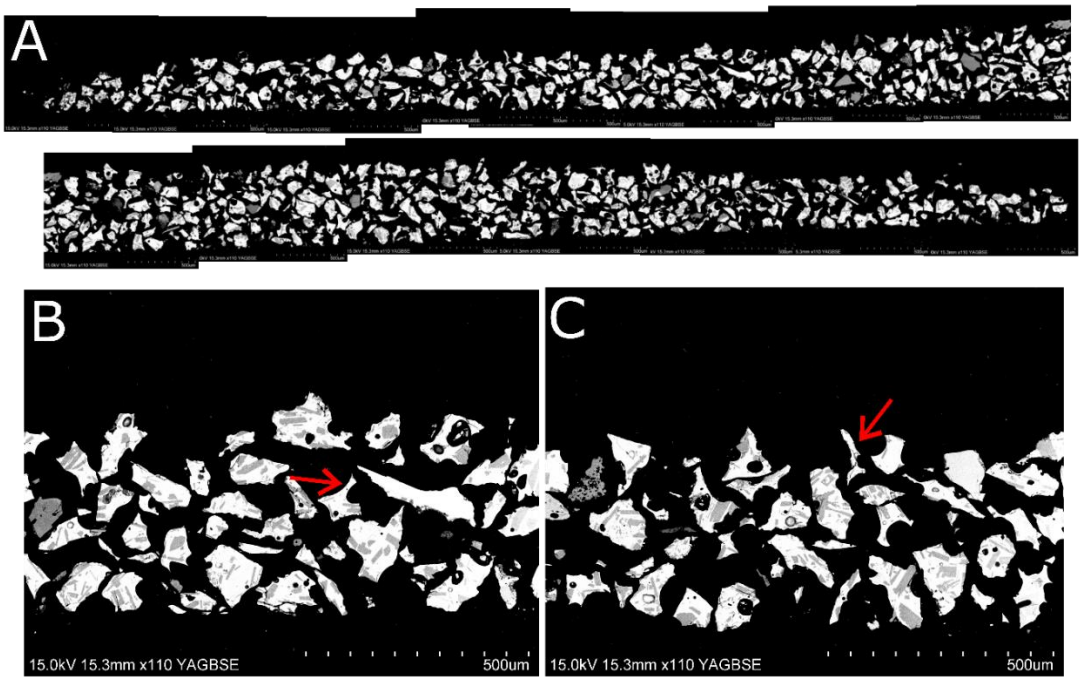

Figure 3.8 A) Unsheared, sieved Green Mountain scoria, B,C) Higher magnification images of the control powder, red arrows indicate highly angular clasts and a vesicle-defined boundary in image B.

3.4 Sub-Seismic (Low Velocity) Experiments – 13µm/s-130µm/s-1300µm/s

The following sections outline the mechanical and microstructural observations from the sub-seismic velocity experiments outlined in Chapter II.

3.5 Sub-Seismic Runs: Mechanical Data

Sub-seismic velocity experiments were designed to investigate slip nucleation. Data can indicate whether material is velocity weakening, a process by which friction decreases with increasing velocity (Scholz & Engelder, 1976; Maron et al., 1998; Bar-Sinai et al., 2015), or velocity strengthening, when frictional resistance increases with increasing sliding velocity.

Figure 3.9 A-C shows *a-b* values for all sub-seismic velocity experiments at each velocity step from which the plots in Figure 1 were made. The changes in shear stress at each velocity step correlate to changes in the friction coefficient values, which were used to calculate the *a-b* values. The friction data from the first velocity steps (from 1.3µm/s to 130µm/s) were disregarded as the frictional behaviour of the material is misrepresentative.

Figure 3.10 compares saturated and room humidity, or room dry, experiments at 1MPa. Most data for the saturated experiment have an *a-b* value >0. In contrast, the room humidity experiment shows a wider spread of data both above and below zero.

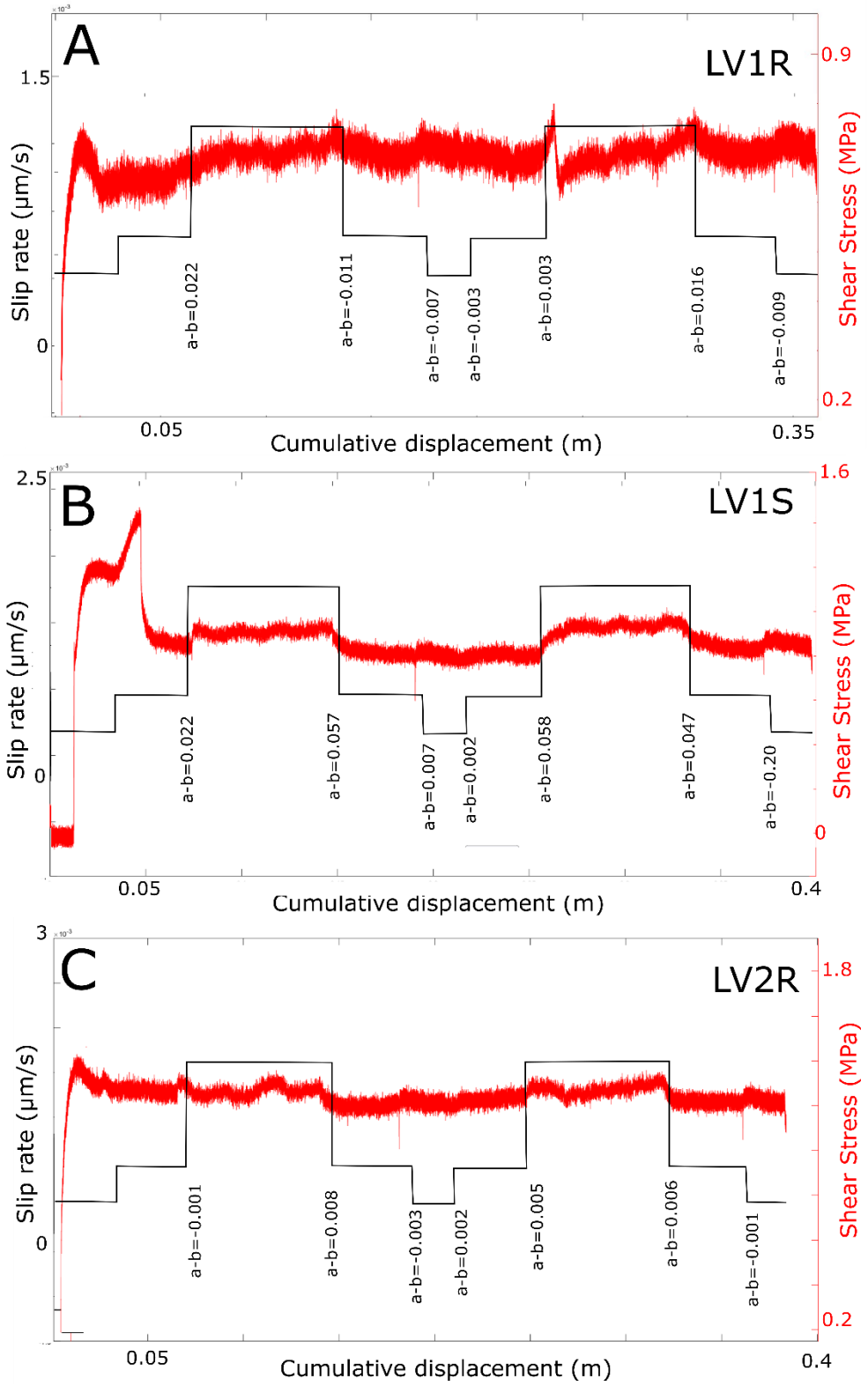

Figure 3.9 Slip rate (µm/s) and shear stress (MPa) plotted against cumulative displacement (m) and showing a-b values for each velocity step (black line) for A) LV1R, B) LV1S and C) LV2R.

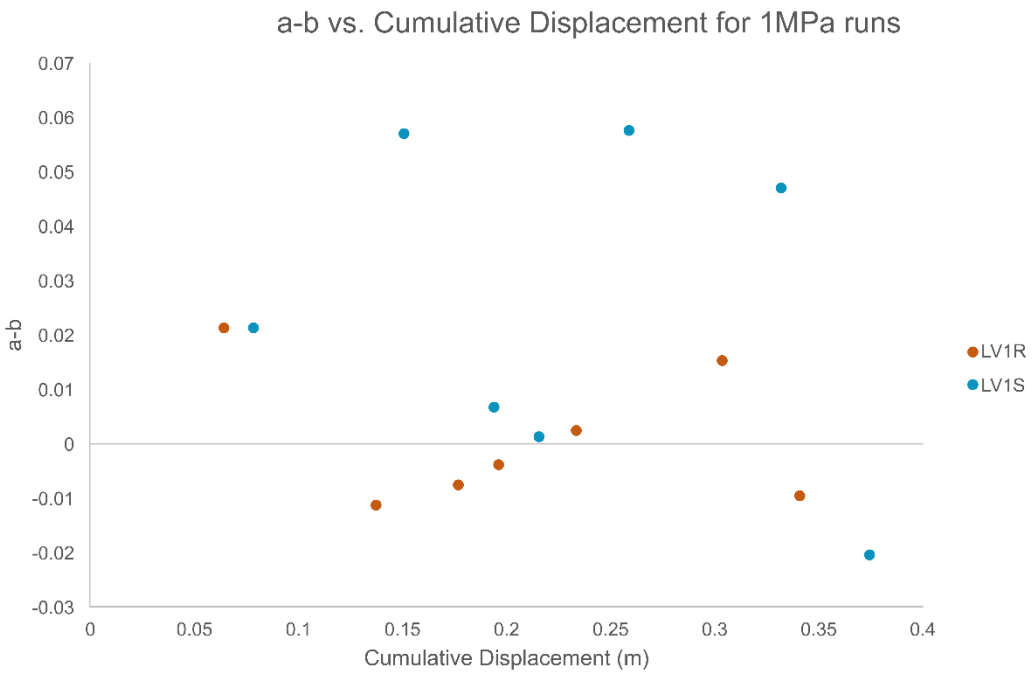

Figure 3.10 Plotted data showing calculated a-b values against cumulative displacement (m) for LV1R (room humidity) and LV1S (saturated).

3.6 Sub-Seismic Runs: Microstructural data

3.6.1 Experiment LV2S (2MPa normal load, saturated)

There is clear grain size reduction localised along a 200-400µm thick layer. The proportion of matrix increases towards the most highly sheared region in the centre, the PSZ) and clasts become more rounded. In the PSZ all clasts are sub-rounded to well rounded (Figure 3.11, A-B), in contrast to outside of the PSZ where sub-angular clasts and clasts with vesicle defined boundaries dominate. Within the PSZ, clasts are poorly sorted with matrix particles <<10µm, and clasts up to 120µm in diameter (Figure 3.11, B). Cracked clasts occur inside and outside of the PSZ, and some show the beginnings of clast disaggregation (Figure 3.11, C). Matrix becomes increasingly dense toward the centre, resulting in lower porosity. Clasts are overall matrix-supported within the innermost region of the PSZ.

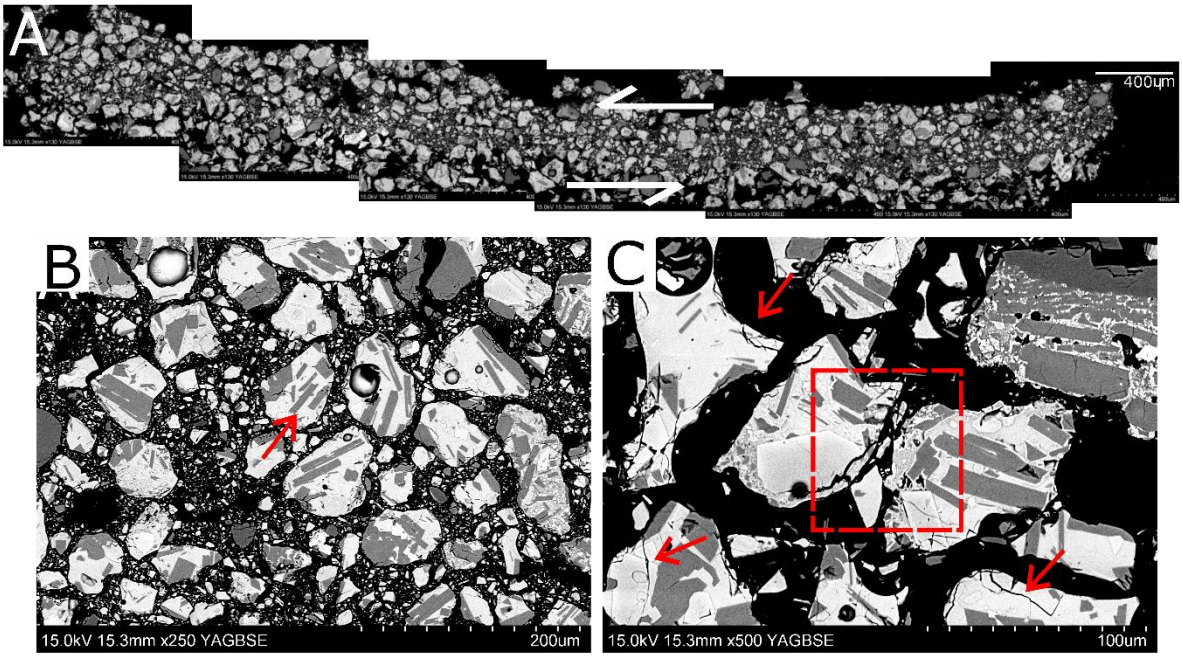

Figure 3.11 A) Sample exhibiting rounding of clasts towards centre of shear zone and an increase in matrix to clast ratio, B) Well-rounded clasts in a poorly sorted part of the shear zone, C) Red arrows indicate cracked clasts on the outer perimeter of the shear zone, red dashed box shows the beginning of clast disintegration.

3.6.2 Experiment LV1S (1MPa normal load, saturated)

Grain size reduction is localised within a 250-400µm thick region, which is less well defined than LV2S (Figure 3.12 A-B). Clasts are poorly sorted with matrix particles <10µm and clasts up to ~130µm in diameter. Compared with experiment LV2S, there is a lower proportion of matrix material, and pore interconnectivity appears visually greater. Within the most densely packed areas of the shear zone, there is still clear pore interconnectivity and the proportion of matrix to clast material appears significantly lower than the 2MPa experiment. Cracked clasts occur primarily near the boundaries of the shear zone (Figure 3.12, B). Some scoria clasts within the shear zone contain intact vesicles with an average diameter of ~30µm with thick vesicle

walls. Clast roundness increases slightly towards the centre of the PSZ, however angular clasts still occur in the centre of the shear zone.

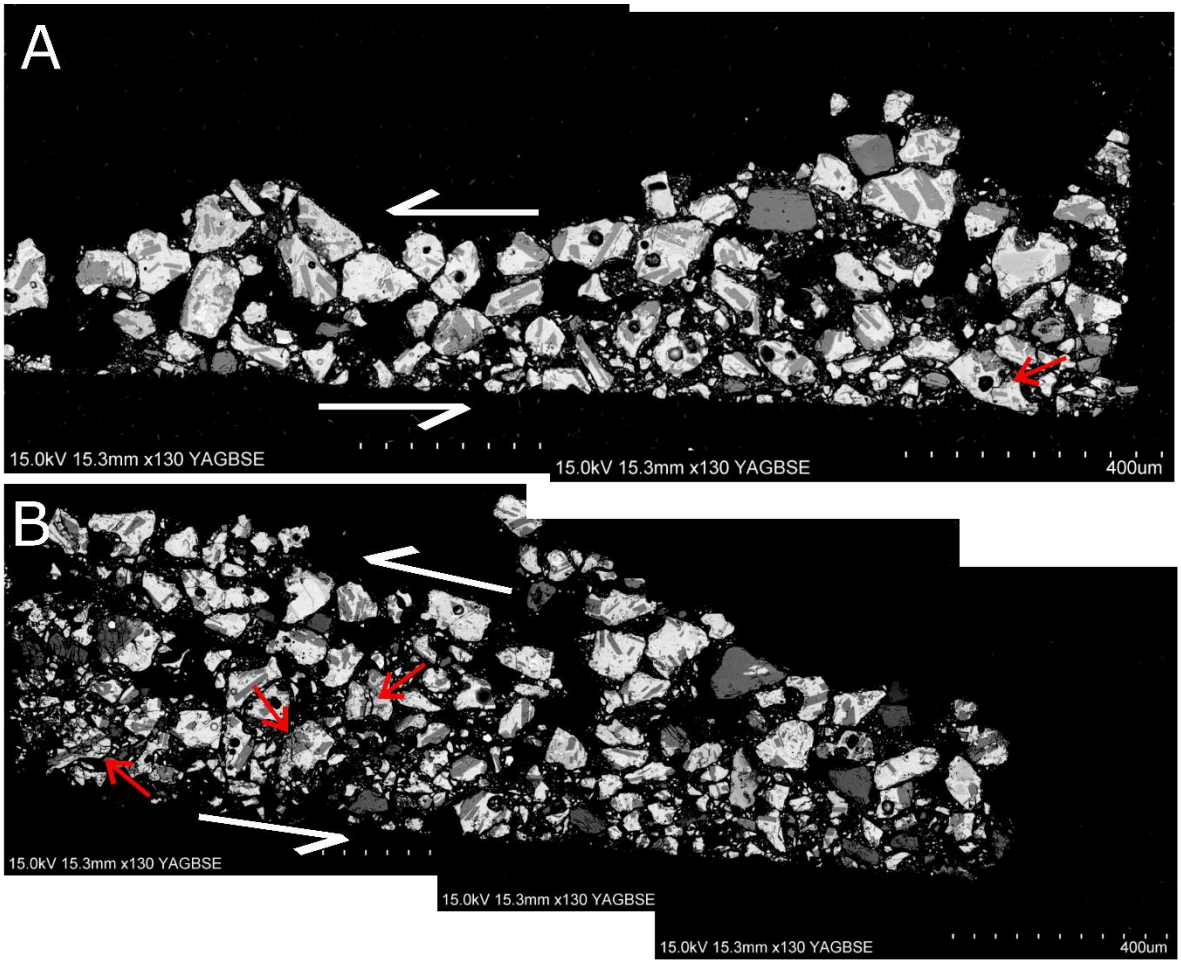

Figure 3.12 A) This run shows a lower proportion of matrix material when compared to its equivalent experiment at 2MPa, B) Red arrows indicate cracked clasts which have not started to disintegrate.

3.6.3 Experiment LV2R (2MPa normal load, room humidity)

In this experiment, much of the material remained preserved and unsheared (Figure 3.13, A). The ~200µm PSZ of highly sheared clasts shows sub-rounded to sub-angular clasts with clasts often exhibiting vesicle defined boundaries (Figure 3.13, A). Within the PSZ, clasts are poorly sorted, some matrix particles are <1µm (Figure 3.20) and clasts are up to 180µm in diameter. Material is poorly sorted, and areas of lower porosity are localised in bands (Figure 3.13, B-D). Clast roundness increases towards the centre of the shear zone, and some scoria fragments exhibit small internal vesicles, generally <25µm, with thick vesicle walls. There is clast truncation and

alignment along the PSZ boundary (Figure 3.13, B-D). There is evidence of clast cracking and varying levels of clast disintegration, the frequency of both increases towards the centre of the shear zone (Figure 3.13, E-G).

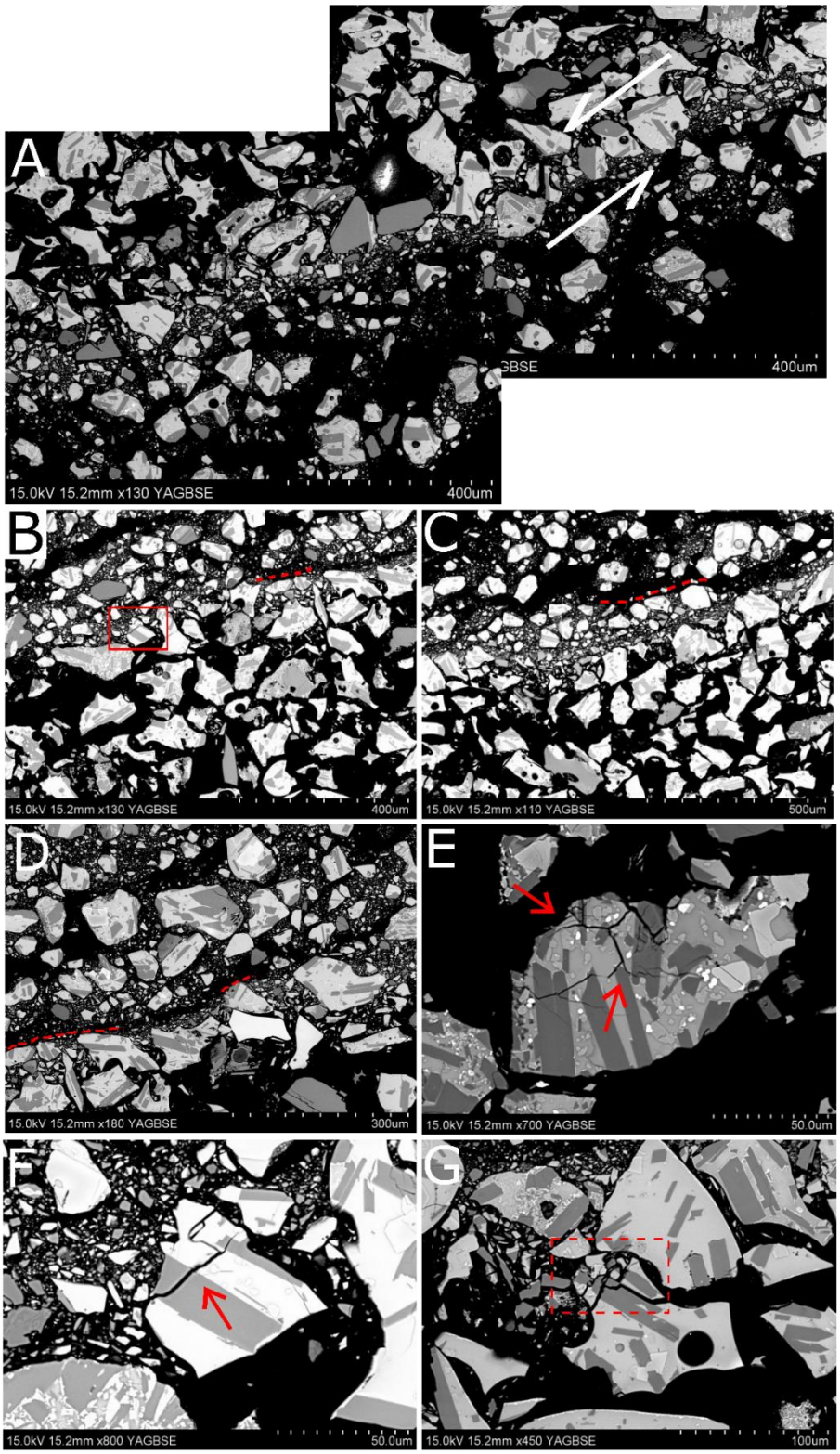

Figure 3.13 A) Sample shows a thin zone of grain size reduction compared to other samples and a higher proportion of unsheared material on the periphery, B) Red box indicated jigsaw crack clast shown in F, B-D) Red dashed lines indicate shear localisations along which clasts have been truncated, E, F) arrows indicate jigsaw cracks on clasts, G) Dashed red box indicates where a clast has started to disintegrate along a series of jigsaw cracks.

3.7 Seismic (High Velocity) Experiments – 1.3m/s

The following sections outline the mechanical and microstructural observations from the seismic velocity experiments outlined in Chapter II.

3.8 Seismic Runs: Mechanical data

Seismic velocity experiments were designed to simulate slip propagation and whether material is velocity strengthening or weakening during this phase.

Figure 3.14 and Table 3.2 demonstrate that saturated runs in both 1MPa and 2MPa experiments have lower peak friction and steady state friction coefficients than dry equivalents. Peak friction values dropped by 0.068 and 0.0561 between saturated and room humidity 2MPa and 1MPa experiments respectively. Steady state friction dropped by 0.0248 between the saturated and room humidity 2MPa experiment and by 0.2688 between the saturated and room humidity 1MPa experiments.

Similarly, both saturated runs have a lower slip weakening distance than their room humidity equivalents. Slip weakening distances dropped by 0.3373m and 0.2167m between the saturated and room humidity 2MPa and 1MPa experiments.

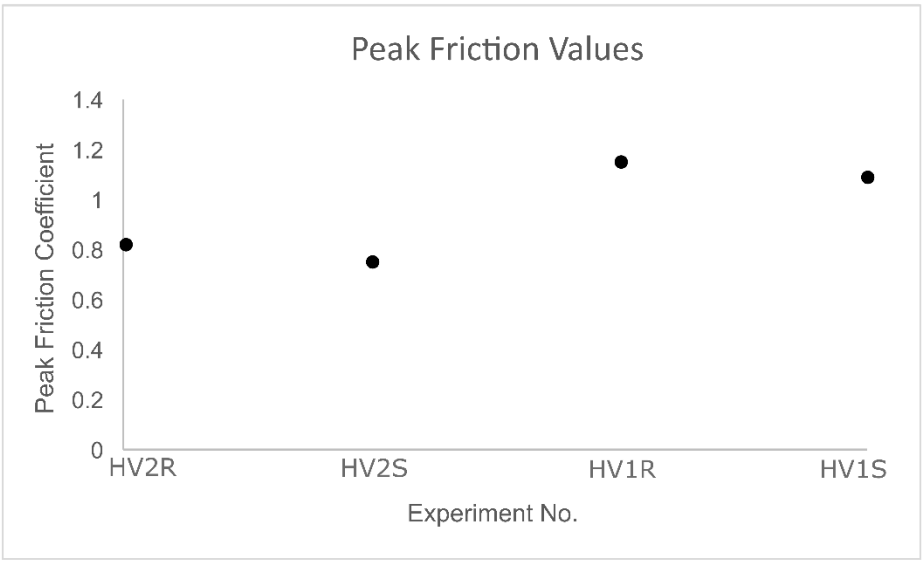

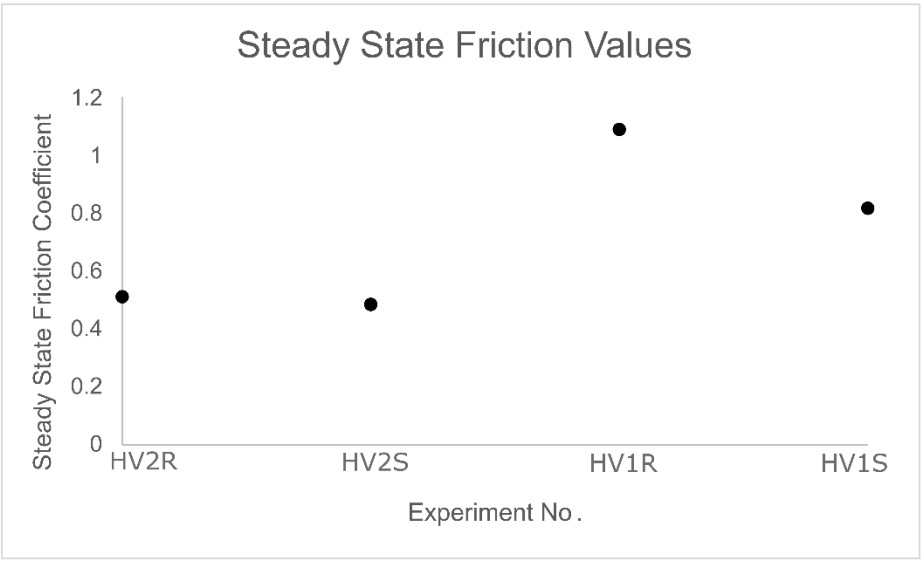

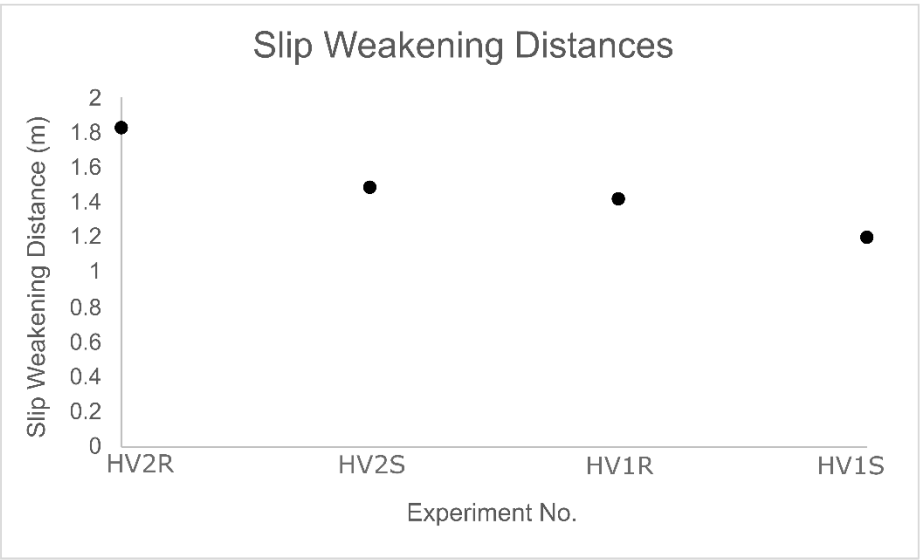

Figure 3.14 A) Peak friction, B) Steady state friction and, C) Slip weakening distances shown for each seismic velocity experiment.

Table 3.2 Tabulated data used in Figure 2

	Experiment	Peak Friction	Steady State Friction	Slip Weakening Distance (m)
Room Humidity	HV2R	0.83	0.51	1.82
	HV1R	1.16	1.09	1.42
Saturated	HV2S	0.76	0.48	1.49
	HV1S	1.1	0.82	1.2

3.9 Seismic Runs: Microstructural data

3.9.1 Experiment HV2S (2MPa, saturated)

This experiment produced a well-defined and consolidated shear zone with variable thickness averaging at 230µm (Figure 3.15, A-B). This is the most well consolidated experimental sample and material is densely packed and grain size reduction is well demonstrated (Figure 3.15, A-D). The shear zone is poorly sorted with fine matrix material <1µm (Figure 3.20) and clasts up to 110µm in diameter. Clasts become more rounded towards the centre of the shear zone. Vesicular clasts within the shear zone contain small vesicles (<30µm) with thick vesicle walls. Pore interconnectivity is low owing to a high matrix to clast ratio. The innermost parts of the shear zone are matrix-supported. There is evidence of clast ‘splintering’ (Figure 3.15, E-G) which was not observed in any other experimental sample or in the GMSZ. Splinters of scoria have broken off from a larger clast and curve around other clasts on the perimeter of the shear zone.

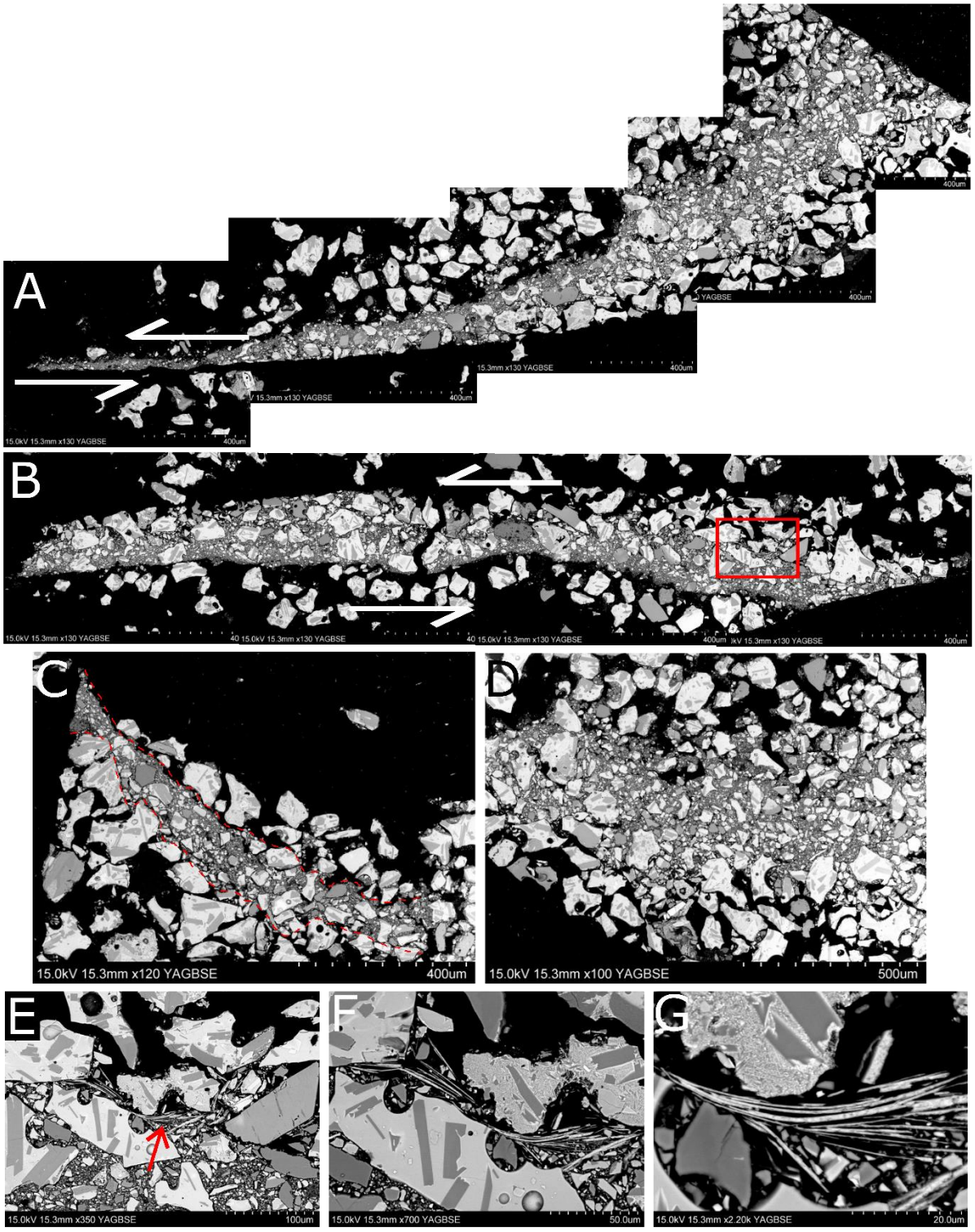

Figure 3.15 A) HV2S sample showing a well-consolidated shear zone of variable thickness, B) Another HV2S sample showing clear grain size reduction, red box indicates location of box E, C) Dashed red line indicates the sharp outer boundaries of the shear layer, D) close-up of matrix material, E-G) splintered scoria at various magnifications, identified on upper outer boundary of shear zone.

3.9.2 Experiment HV2R (2MPa, room humidity)

This experiment produced a PSZ marked by higher pore space and pore interconnectivity and a lower matrix-to-clast ratio than the satuarated experiment equivalent, HV2S (Figure 3.16, A-C). Shear zone thickness varies from 200-550µm and boundaries between sheared and unsheared material are gradational. Clasts are up to 150µm and the finer material >5µm. Clasts are sub-angular and increase in roundness toward the centre of the shear zone. Compared to the 2MPa seismic velocity wet run, this sample appears more clast supported in areas, and less well indurated. Jigsaw cracks are observed on clasts (Figure 3.16, C).

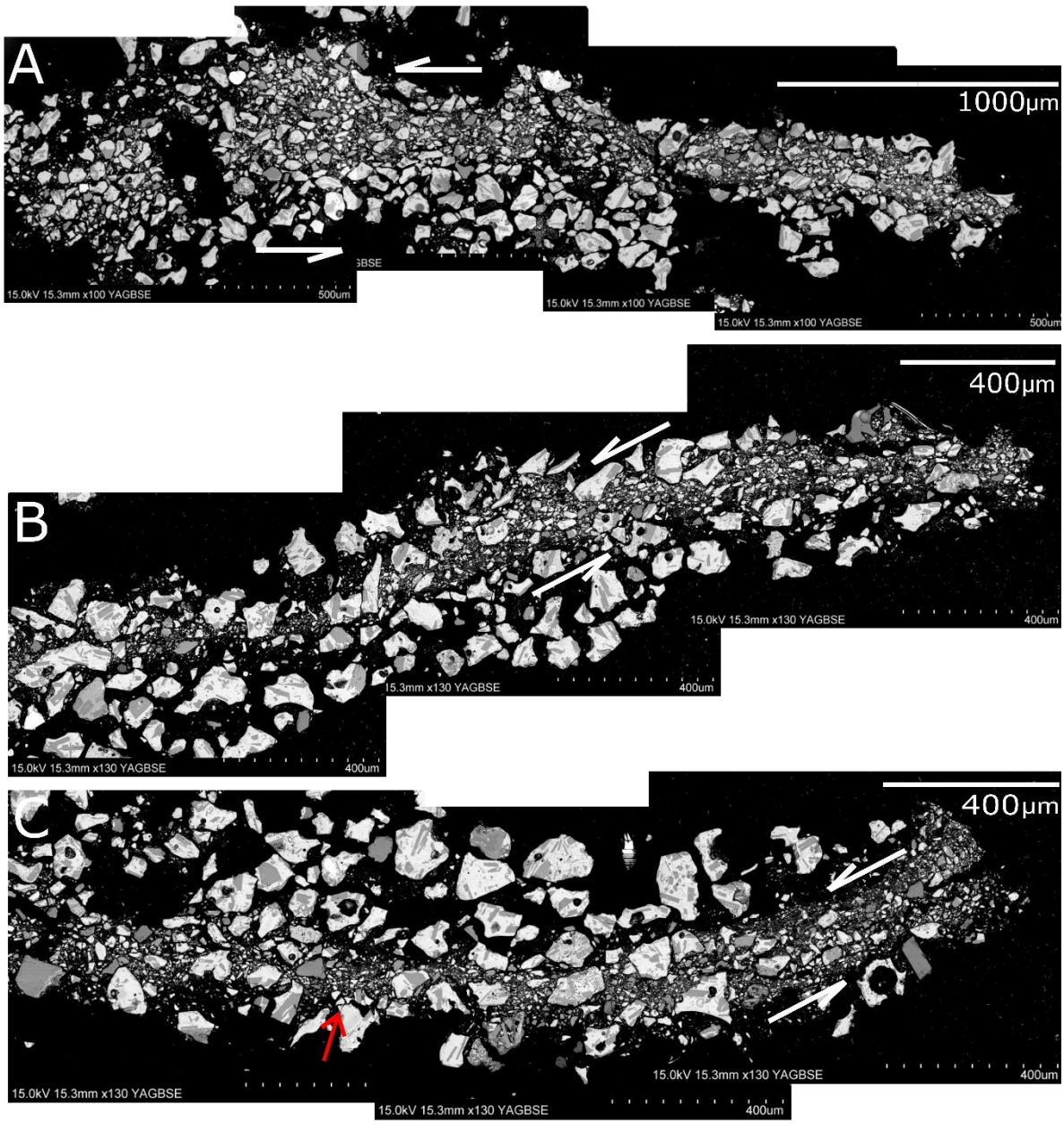

Figure 3.16 A-C) Sample shows clear grain size reduction but pore interconnectivity seems more apparent than in HV2S. Red arrow on C indicates jigsaw cracks.

3.9.3 Experiment HV1R (1MPa, room humidity)

This experiment produced a PSZ with a thickness of 150-200µm (Figure 3.17, A-B). Matrix is <1µm (Figure 3.20) and clasts are up to 100µm in diameter. Clasts are poorly sorted, although thinner (~50µm) disjointed bands of moderately sorted finer material occur throughout. Clasts increase in roundness towards the centre of the PSZ. The matrix to clast ratio is highest in the centre of the sample, where clasts are matrix-supported. Clasts become progressively more clast-supported away from the centre of the PSZ. Pore space and interconnectivity are lowest toward the centre of the shear

zone. Pockets of higher porosity within areas of higher matrix occur away from the PSZ. No large vesicular clasts are present within the centre of the PSZ. Jigsaw crack clasts occur throughout the shear zone (Figure 3.17, C).

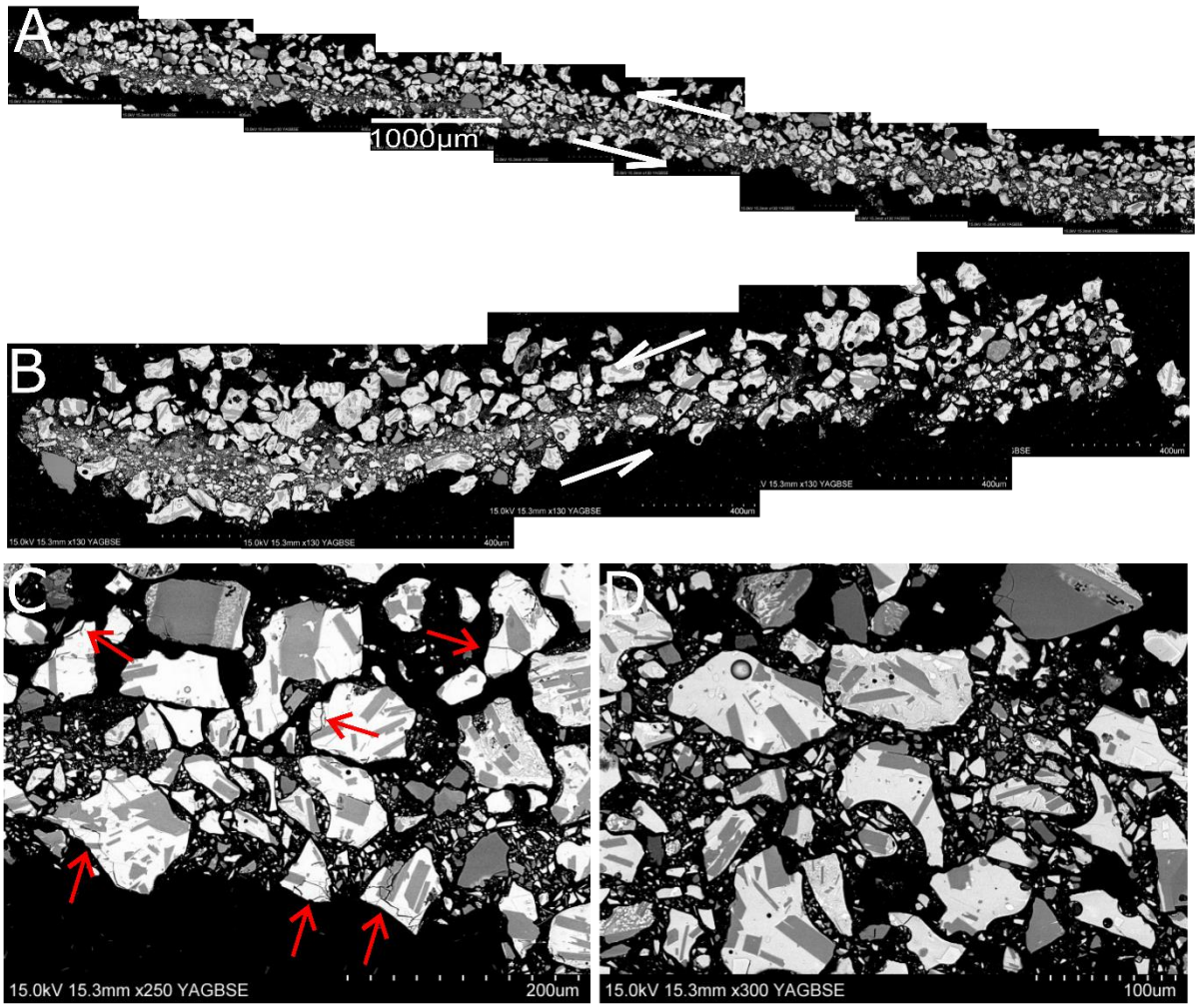

Figure 3.17 A-B) Experimental samples showing localised shear over 150-200µm thick region, C) Red arrows point to jigsaw cracks on clasts, D) Larger sub angular clasts in a finer matrix.

3.9.4 Experiment HV1S (1MPa, saturated)

Grain size reduction is localised to a 250-400µm layer (Figure 3.18, A-B). The smallest clasts are <5µm and clasts reach up to 100µm in diameter. Clasts are poorly sorted and the matrix to clast ratio is lower than experiment HV1R, with evident pore interconnectivity between finer material (Figure 3.18, C-D). Porosity is visibly reduced; however, matrix material is not localised to the same extent as other experimental samples, and instead is more widely and gradationally distributed throughout coarser material. Clasts become progressively less matrix supported with distance away from

the centre of the shear zone. There is evidence of clast disaggregation and jigsaw-cracks on clasts. Clasts become progressively more rounded towards the centre of the shear zone and no highly vesicular clasts are present along the PSZ.

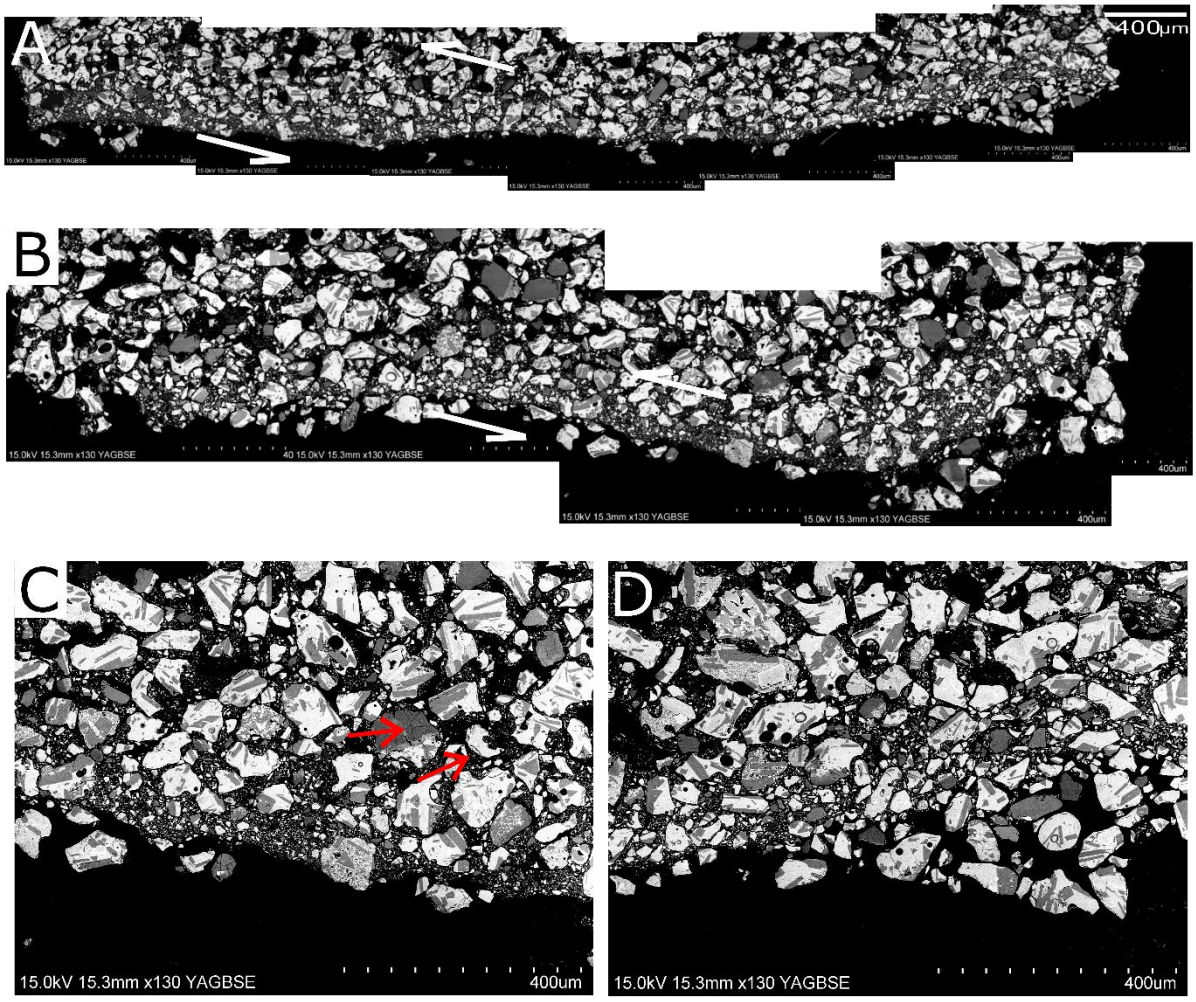

Figure 3.18 A-B) Shearing has produced a higher concentration of matrix material at the base of the shear zone, which becomes more dispersed toward the top C) Red arrows point to jigsaw crack clasts, D) Material becomes more rounded with distance to the base of the shear zone.

3.10 Experimental Shear Zones: General Observations

Each of the experimental runs show the development of a PSZ with a finite thickness between 150-550µm. Each experimental shear zone exhibits grain size reduction toward the PSZ and a resulting increase in matrix material, which reduces porosity. Evidence for cataclastic processes is observed, such as the presence of jigsaw fit and crack clasts and the migration of fragments away from parent clasts. Clasts increase in roundness toward the centre of the shear zones and highly vesicular scoria clasts are preferentially fragmented. Clast truncation along shear localisations is observed in some of the samples.

3.11 Grain Size Reduction Investigation

Investigation into grain size reduction pre- and post-shearing for 3g of powdered Green Mountain basaltic scoria for 2 seconds at 1.3m/s, under room dry conditions at 1MPa, (the same conditions as experiment HV1R) is presented in Figure 3.19 and Table 3.3. Data show a decrease from a mean particle size of 130 to 109µm after shearing. This is reflected in the median and modal values in Table 3.2 decreasing by 15µm and 12µm respectively. A skewness value of -0.53 shows that the data are skewed slightly to the left, towards finer values and the kurtosis value is <3, showing that the dataset has lighter tails than a normal distribution. The increase in standard deviation and in variance demonstrate that the data are more widely spread post-shearing. The D_{10} value decreases from 83 to 22µm, the D_{50} from 131 to 116µm and the D_{90} from 184 to 169µm. This grain size reduction resulted in the generation of nanoparticles in both the GMSZ and all the experimental runs, examples of which are shown in Figure 3.20.

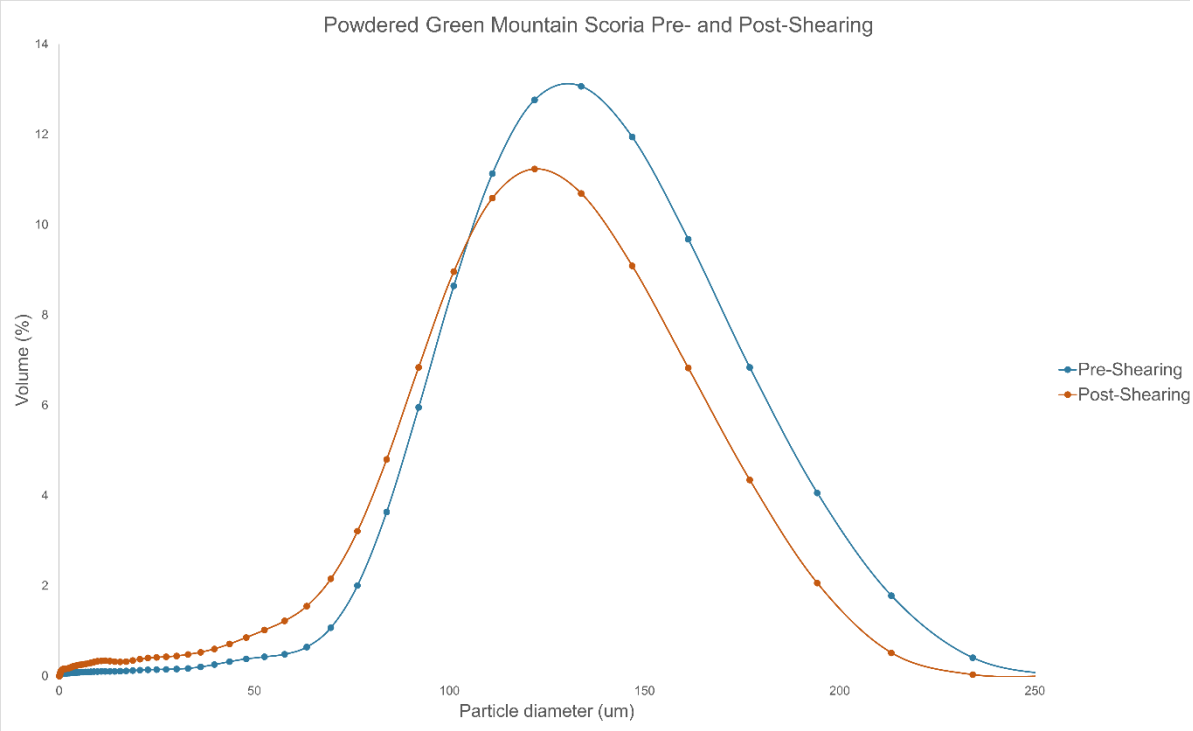

Figure 3.19 Particle diameter (µm) plotted against volume (%) between 3g of powdered Green Mountain scoria sieved through 90-125µm mesh before and after 2 seconds of shearing under 1MPa at 1.3m/s under room dry conditions.

Table 3.3 Key measured parameters of scoria gouge before and after shearing, analysed using a Beckman Coulter LS13 320 Laser Granulometer

Statistical Parameter	**Pre-Shearing**	**Post-Shearing**
Mean particle size (µm)	130	109
Median Particle size (µm)	131	116
Mean/ Median ratio	0.99	0.94
Mode (µm)	140	127
Variance	1929	2553
Standard Deviation	43	50
Skewness	-0.53	-0.52
Kurtosis	0.9	-0.2
D_{10}	83	22
D_{50}	131	116
D_{90}	184	169

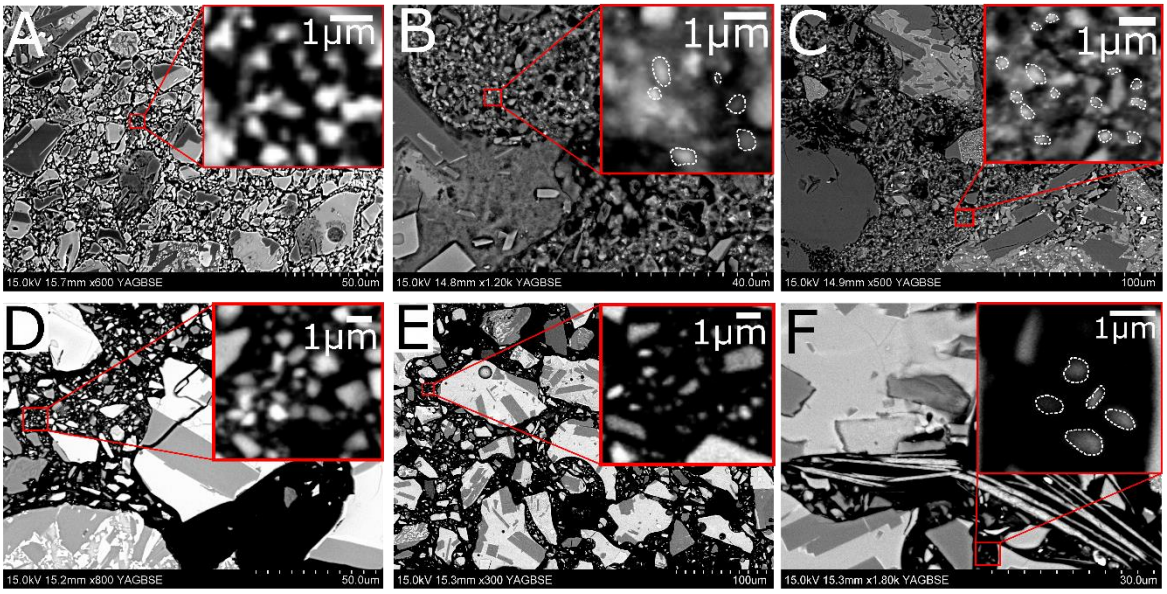

Figure 3.20 A-C The presence of nanoparticles (<1µm) in the Green Mountain VDAD shear zone and D-F) Nanoparticles generated from experiments LV2R, HV1R, and HV2S respectively.

Chapter IV: Discussion

4.1 Green Mountain Collapse Deposit: Classification

The Green Mountain eruption dated at 300kya (Preece et al., 2021) produced a scoria cone that forms the highest point of the island. This scoria fall deposit mantled the pre-existing steep slopes on the north of the island. Part of the flank of this scoria cone then collapsed and travelled ~2km down a 10° slope, from a starting elevation of ~550m above sea level and terminating at 190m above sea level against a lava dome.

The resulting ~4 x 10^6 m^3 deposit, as described in Chapter 1, has not yet been formally classified. Classification of such collapse deposits is useful to constrain flow behaviour based on deposit characteristics. The Green Mountain collapse deposit best fits the characteristics of a volcanic debris avalanche deposits, as discussed below.

4.2 Classification of Gravitational Collapse Deposits

There are no exhaustive set of criteria for different types of gravitational collapse deposits, and there is significant overlap in characteristics between deposit descriptions. The term *landslide* is general and nondescript, and it can be beneficial to better constrain deposit types based on physical attributes.

An often-cited metric is Heim's ratio, the height/length (H/L), ratio of a gravitational collapse deposit. The H/L ratio calculated for the Green Mountain collapse deposit is 0.18 with the horizontal *r*unout of this collapse being 5.5x that of the vertical drop height, making this a small deposit (see Figure 4.1), although the error on this calculation is high, ± 200m, as the detachment surface of the collapse is unclear, and the deposit was stopped at its base by a lava dome; runout may have been longer had this not been the case. Allowing for this error, the H/L value lies between 0.09-0.25.

4.2.1 Volcanic Debris Avalanche Deposits

VDADs are generally associated, in the field, with a detachment scarp, and a hummocky or ridged surface. Internal structures commonly include jigsaw-crack and jigsaw fit clasts, megaclasts that preserve original structures, internal faults and shear structures, material injections with fluidal contacts, and horst and graben structures (Siebert, 1984; Glicken, 1991, 1996; Ui et al., 2000; Van Wyk de Vries & Davies, 2015; Moreno-Alfonso et al., 2021). Notable volcanic debris avalanches include the 1980 Mt.

St. Helen's collapse, although some argue this was a sturzstom (Voight et al., 1980; Ward & Day, 2006).

The Green Mountain scoria cone and fall deposit has been partially eroded, meaning topographical features are difficult to identify, however a detachment surface has been identified but is highly weathered. Field investigation shows the deposit has a moderately hummocky surface, and a heavily fractured deposit toe. The emplacement and transport of the heterolithic lithology above the basal scoria requires further investigation, but abundant, large flame structures that dominate the lithology suggest a degree of fluidisation and the presence of water during emplacement. There characteristics could classify the deposit as a small VDAD (Figure 4.1).

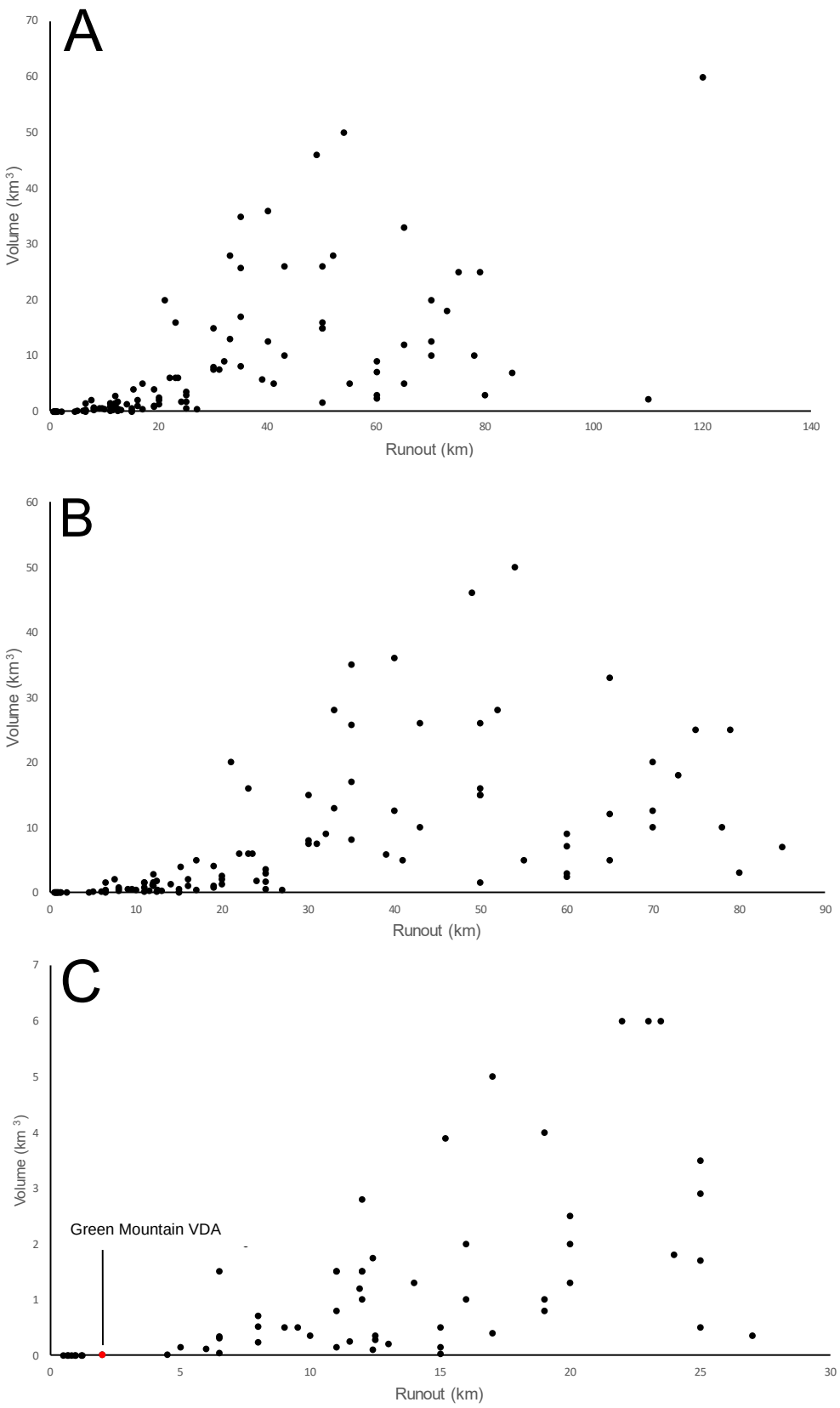

Figure 4.1 Volume (km^3) versus runout (km) for various documented subaerial VDADs for A) n=108, B) n=106, and C) n=62. Note that Figure C shows the Green Mountain VDAD. See Appendix 2 for raw data.

4.3 Localised vs. Diffuse Accommodation of Strain

There are instances of gravitational collapse deposits accommodating shear within localised bands (e.g., Belousov, 1999; Wang et al., 2010; Hughes et al., 2020), as is observed within the Green Mountain collapse, or over a more widely dispersed region within the collapsed material (e.g., Wang, 2017; Dufresne et al., 2017; Zhang & McSaveney, 2017). Localised failure refers to failure that takes place at the Mohr Coulomb strength envelope and occurs along a sliding surface, whereas diffuse failure occurs where instability and failure are observed at effective stresses below the Mohr Coulomb strength envelope (Labuz & Zhang, 2012; Pastor et al., 2010). Localised failure tends to occur in over-consolidated materials, whereas low density, compactible materials tend to favour diffuse strain accommodation (Pastor et al., 2010). Other proposed factors affecting strain accommodation are thought to include flow plasticity (Darve & Laouafa, 2000; Leroueil, 2001; Pastor et al., 2004; Cascini et al., 2013), deformation rate (Iverson et al., 1997), the presence of pore water (Dai et al., 1999; Wang et al., 2002;Chu et al., 2003; Olivares & Damiano, 2007), grain size (Wang & Sassa, 2003), and slope angle (Darve & Laouafa, 2000).

The shear forces of the Green Mountain collapse deposit have been localised along a shear zone with a finite thickness of 1-2cm, and further localised within the PSZ observed in Zone A, where porosity and grain size reach a minimum. This is similar to another shear zone generated by volcanic collapse from the Pichu Pichu volcanic complex in Peru, which is an intra-deposit shear zone hosted in andesitic lava flows (Hughes et al., 2020). The Pichu Pichu deposit shows evidence of frictional melting, with a combination of ultracataclasite and discontinuous pseudotachylite (Hughes et al., 2020). The Pichu Pichu collapse deposit has an area exceeding 20km^3, whereas the green Mountain deposit only has an area of ~0.004km^3. The Pichu Pichu shear zone (Figure 4.2, A,B) and the Green Mountain collapse shear zone (Figure 4.2, C-F) have several similarities. Both shear zones appear similar on outcrop-scale, presenting as a thin band within a single lithology, with no evidence of material adjacent to the shear zones being disturbed or strained. In the Pichu Pichu shear zone, pseudotachylite generation is highly localised in areas of extreme shear, explaining its discontinuous nature (Hughes et al., 2020); this is not observed in samples of the Green Mountain collapse shear zone. It is possible that the overburden was not

significant enough to produce melt, or that runout distance was not long enough to facilitate frictional melting.

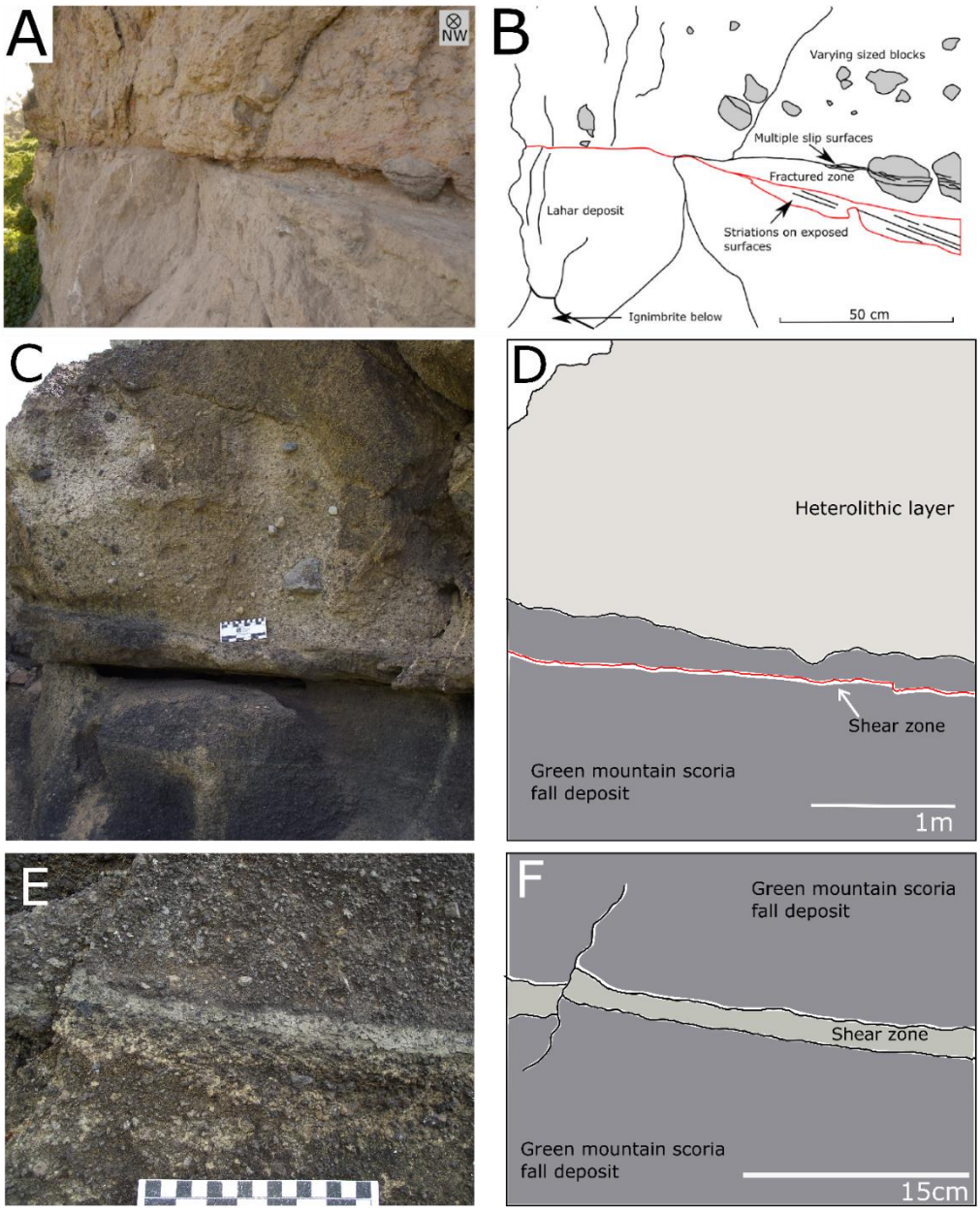

Figure 4.2 A,B) Slip zone showing intense cataclasis and striations on lower contact at the Pichu Pichu site (Hughes et al., 2020), C,D) Green Mountain collapse slip zone outcropping in cross-sectional view on Ascension Island, E,F) Close up of Green Mountain collapse shear zone showing thickness and appearance at outcrop scale. Green Mountain photos from Preece (2015).

4.4 Microstructural Observations

4.4.1 Green Mountain Shear Zone (GMSZ)

The key features of the GMSZ microstructral evolution with depth include (1) a sharp decrease in grain size from outside the shear zone to the material that characterises the shear zone itself, (2) a gradational decrease in grain size from the material at the periphery of the shear zone to that in the PSZ, (3) a concomitant gradient in porosity which decreases form the peripheries of the shear zone to the PSZ, and finally, (4) a clear increase in both circularity and solidity from the periphery to central regions of the shear zone. Taken together, these observations demonstrate that the shear zone is both different from the surrounding material, and internally gradationally variable from one edge to the other. These observations are best explained by shear zone related processes as discussed below.

4.4.2 Experimental Run Products

As with the GMSZ, each experimental shear zone demonstrates a decrease in grain size and porosity within the PSZ. All experimental shear zones also show evidence of evolving clast morphology, with clasts becoming more rounded and highly vesicular scoria clasts decreasing in frequency toward the PSZ. The presence of nanoparticles and clast truncation surfaces are also observed in the experimental runs. The experimental shear zones exhibit these characteristics to differing extents. Thicknesses of the experimental PSZs lie between 100-550μm, as shown in Table 4.1.

Table 4.1 Thickness variability within and between experimental shear zones

Experimental run	LV2S	LV2R	LV1S	HV2S	HV2R	HV1S	HV1R
PSZ thickness	200-400	200-250	250-400	100-470	200-550	250-400	150-200

Of the experimental samples, the most well-indurated with the highest proportion of matrix is HV2S, and conversely the sample which has the least amount of matrix Is LV1S. Experiment HV2S also produced clast splintering (Section 4.8) which is not observed in any other experimental shear zones. The distinct reduction in grain size from outside to inside the shear zones is evidence for the development of a principal

slip zone (PSZ), along which strain is accommodated. Comparison of the control powder to experimental shear zones illustrates this grain size distribution change, as the control powder is coarser grained, highly angular, clast supported and shows high porosity.

There are limitations to the experimental methods used. For example, the diameter of the Green Mountain scoria used in shearing experiments was restricted by equipment constraints. The natural scoria samples from the study site range in size from millimetre blocks to metre scale blocks, whereas the material used for experiments was sieved through a 90-125µm mesh. Therefore, this is not wholly representative of the natural material. The investigative work on the LG showed that this sieved material ranged from 1-256µm, showing human or equipment error in the sieving process. For example, if the long axis of a particle is greater than 125µm but the short axis is between 90-125µm, the particle will still fit through the mesh. Only 1g of this material could be used per experiment and the average thickness of powder within the cylinder pre-shearing was 1.33mm. These factors limited the extent to which the PSZs could develop spatially.

It is difficult to calculate what the normal load would have been when the natural shear zone was generated, as the overburden material, slope at the time of collapse and the acceleration of the avalanche are unknown. The normal pressures of 1 and 2MPa used in the experiments are likely slightly higher than what the shear zone would have formed under, however these were the lowest normal loads under which data could be reliably measured using the LHVR equipment.

Retrieved experimental samples were mostly composed of loose powder and small chips of better consolidated but still highly fragile material which constitutes the PSZ - these chips were impregnated with resin. For this reason, there is no sample for the low velocity, 1MPa normal load, room humidity run (LV1R) as the material was too fragile to be retrieved.

4.4.3 GMSZ vs. Experimental Run Products

There are key microstructural similarities between the GMSZ and the experimental shear zones. Both show the clear development of a PSZ of highly localised shear where most of the slip is accommodated. Both show grain size reduction and a resulting decrease in porosity toward the PSZ and similarities in grain breakage

patterns (Section 4.5), grain circularity and solidity increase and a decrease in the frequency of highly vesicular scoria clasts in more sheared regions (Section 4.6), where levels of clast fragmentation and crushing are highest. Clasts on the periphery of the shear zone have a higher average grain size, lower circularity, and lower solidity. Toward the centre of the shear zone, porosity decreases as the proportion of matrix material increases. This is proven quantitively in the natural shear zone and observed in the experimental shear zones. These changes are indicative of cataclastic flow processes (Sibson, 1977; Borradaile, 1981).

Other microstructural features also observed in both the experimental samples and GMSZ include the truncation of clasts along the PSZ (Section 4.7) and the presence of nanoparticles (<1µm). These structures suggest that strain is preferentially accommodated by destructive grain comminution and fragmentation processes rather than non-destructive processes such as grain rolling or sliding. A feature observed in one of the experimental samples not seen in the GMSZ is the splintering of clasts (Section 4.8).

Foliation fabrics are not observed in the natural or experimental shear zones. Although foliation can develop in sheared granular material, experimental work suggests that these develop only at high normal stresses (>25MPa) (Mair et al., 2002).

Overall, grain size is greater within the natural samples as the starting material was coarser. Additionally, the natural shear zone is thicker, averaging 1-2cm, as it was not constrained to the size of the equipment used for experiments, which produced shear zones ranging from 150-550µm in thickness.

4.5 Grain Size and Porosity Reduction & Clast Breakage

An increase in the matrix-to-clast ratio toward the most highly sheared regions of the shear zone is observed in both the natural and experimental samples. This is a result of grain size reduction which, in turn, drives a decrease in porosity.

The experimental work demonstrates that shearing results in grain size reduction, and that this is by the disaggregation of larger grains. This is shown firstly by the LG analysis, which shows that shearing scoria leads to a finer grain size distribution. Secondly, SEM images show that the control powder has no matrix material before shearing and, in contrast, all sheared experimental samples have a significant portion

of matrix and visible grain size reduction. This suggests that the presence of fine matrix material in the experimental shear zones must be due to grain size reduction by the comminution of larger grains, rather than the migration, reorganisation, and concentration of pre-existing finer material from other regions of the deposit along the shear zone.

Evidence of grain comminution processes can be observed in SEM images of the natural and experimental shear zones. The presence of cracked grains (Figure 4.3) which had begun to disaggregate and become infilled with matrix material are evidence for brittle failure and cataclastic processes (Blenkinsop, 1991; Tullis & Yund, 1987). The similarities in grain breakage patterns between the natural and experimental samples suggest that grain size reduction is facilitated by cataclasis in both natural and experimental shear zones. This is supported by evidence that at the base of shallow landslides with low-plasticity dry materials, deformation is usually brittle (Larue & Hudleston, 1987). There is likely a bias in the identification of jigsaw crack over jigsaw fit clasts as the more clasts disaggregate and fragments migrate from one another, the harder it is to prove that fragments originated from the same parent clast.

Rotary shear experiments show that increased shear strain and normal stress reduce grain size (Zhang & McSaveney, 2017). This is observed in rock avalanches, where the finest grain size distributions are found where normal stress and shear displacement are largest, as is observed with the shear localisation within the Green Mountain VDAD. Conversely, as normal stress and shear displacement decrease grain size distribution becomes coarser (Dunning, 2004; Cagnoli & Manga, 2004; Cagnoli & Romano, 2013; Zhang & McSaveney, 2017).

The disaggregation of clasts during rock avalanches and debris flow transport is proposed as a mechanism for facilitating high mobility (Davies & McSaveney, 2009; De Blasio & Crosta, 2014). Dynamic fragmentation of clasts is hypothesised to decrease effective stress in the system, by the finer matrix material dissipating load transfer between larger clasts. This is believed to reduce the friction coefficient and, in turn, facilitate longer run-out distances (Rait et al., 2012).

A decrease in porosity is quantitatively proven in the natural shear zone, and qualitative analysis of the experimental samples shows a visible decrease in porosity

within the PSZs of the experimental samples. Reduction in pore space is related closely to grain size reduction; a decrease in grain size reduces interconnected pore space and therefore permeability (Kimura et al., 2018). As with grain size reduction, pore diameter reduction in granular material is shown to be positively correlated with greater shear displacement and higher normal stress, resulting in a positive correlation between grain size reduction and reduction in permeability (Kimura et al., 2018).

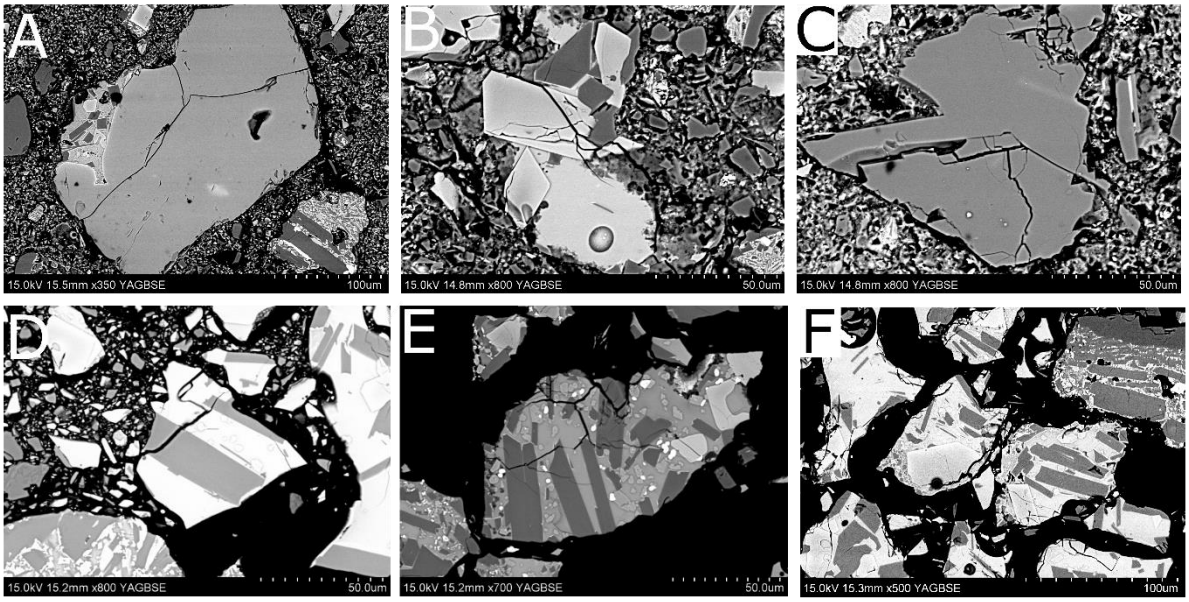

Figure 4.3 A-C) Cracked clasts from natural sample, A is from Zone B, B and C are from Zone C', D-F) Cracked clasts from experimental samples, D and E are from LV2R, F is from LV2S. All clasts are fractured but have not started to fully disaggregate.

4.6 Circularity, Solidity, and the Distribution of Vesicular Scoria Clasts

Both the circularity and solidity of clasts increase toward the centres of the natural and experimental shear zones. Highly angular clasts are preferentially eroded to become more rounded and the increase in grain roundness towards the centre of the shear zone is likely a result of abrasive syn-shearing processes (Mair & Abe, 2011).

The high angularity of clasts on the periphery of the shear zone is partially due to the higher frequency of clasts with vesicle defined boundaries, which have a low solidity and become better rounded with shearing. Similarly, the proportion of 2-7mm scoria clasts with in-tact internal vesicles decreases markedly towards the centre of the natural shear zone. The same is observed in the experimental shear zones. This can be explained by clasts with high vesicularity having lower compressive strength. It has

been shown that the uniaxial compressive strength of vesicular basalt decreases with increasing porosity (Kelsall et al., 1986; Al-Harthi et al., 1999) and that failure is preferentially accommodated along lines of vesicles (Murthy et al., 2020).

4.7 Clast Truncation

Truncated clasts are observed in the natural and experimental samples (Figure 4.4, A-D). Straighter truncations are associated with more mature slip surfaces, and act as evidence for high velocity slip (Smeraglia et al., 2017; Fondreist et al., 2015).

Truncated clasts such as those observed in the natural sample (Figure 4.4, A,B) are commonly observed along the boundaries of principal slip zones. Such clasts are observed on the Tre Monti principal fault, Italy along a sub-boundary (Figure 4.4, C,D) (Smeraglia, 2017) and these are understood to represent high strain rate and seismic-speed slip localisation.

As shear localisation continues and the shear zone matures, the truncation of clasts becomes flatter, and the alignment of the boundary becomes straighter. An immature shear boundary is more undulating, and clasts are often more jagged, such as that observed in the in the natural sample (Figure 4.4, A,B) and the curved truncation surface in experiment LV2R (Figure 4.4, B,C), these suggest that shearing stopped before the boundary could become smoother and straight, such as that observed at the Tre Monti principal fault (Figure 4.4, E,F). The truncations observed in Figure 4.4, A-D may suggest the development of a ‘proto-PSZ’, with slip surfaces beginning to evolve but at a primary stage of development, as not enough slip distance was yet accumulated to allow for a mature PSZ in both the natural and LV2R shear surfaces.

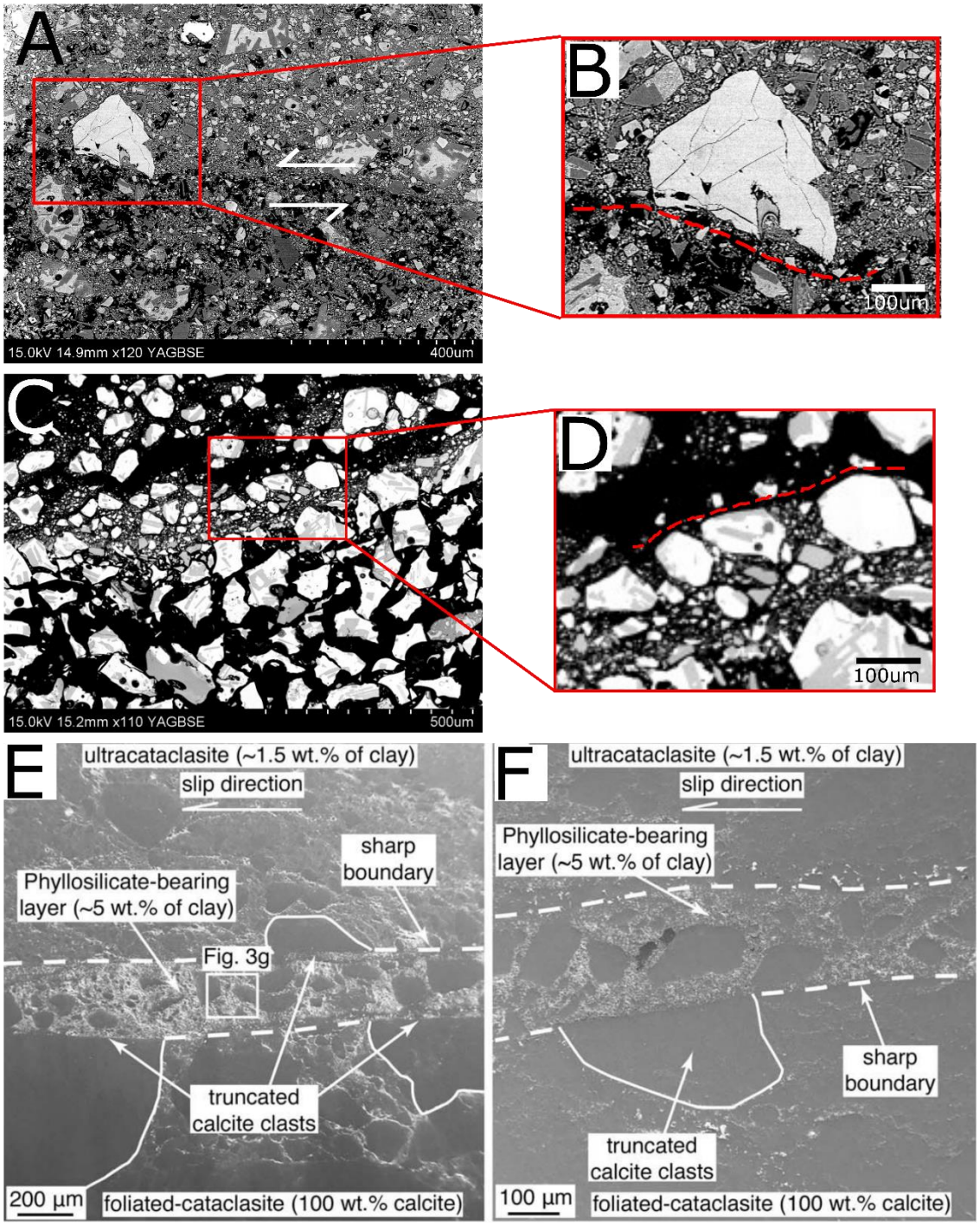

Figure 4.4 A-B) best example of a truncated clast, here a free plagioclase crystal, observed in the natural shear zone, red dashed line indicates truncation boundary, C-D) Truncated clasts identified in experimental sample LV2R, red dashed line indicates boundary along which truncation has occurred, E-F) Truncated calcite clasts along PSZ boundary (from Smeraglia, 2017).

4.8 Clast Splintering

The warping of splintered clast fragments as observed in experiment HV2S (Figure 4.5, A-D) are comparable to structures observed in shearing experiments by Wang (2017) conducted on basal soil facies of the Yigong rock avalanche under 1.47MPa at shear rates of 0.07 and 0.26m/s (Figure 4.5, E,F).

In both cases, these structures are found at the outer limit of the shear zone and show directional alignment of particles without fragmentation (Wang, 2017). This is suggested to represent strain accommodation under less stress, hence why these structures are not observed in the centre of shear zones. This is consistent with the periphery of the shear zone, where the proportion of matrix material visibly decreases and clasts are larger and more angular, being under less strain than the central regions. Such structures were not observed in the GMSZ samples. It is possible that these structures were present and simply not observed. If, however, clast splintering is absent from the GMSZ, this suggests that that any combination physical conditions including saturation, velocity, clast size and geometry and temperature conditions that allowed for clast splintering to occur in the experimental run HV2S and the basal facies of the Yigong rock avalanche were absent during the formation of the GMSZ. For example, the peripheries of the GMSZ may have been under great enough stress that lower stress-strain accommodation signatures, such as clast splintering, did not occur.

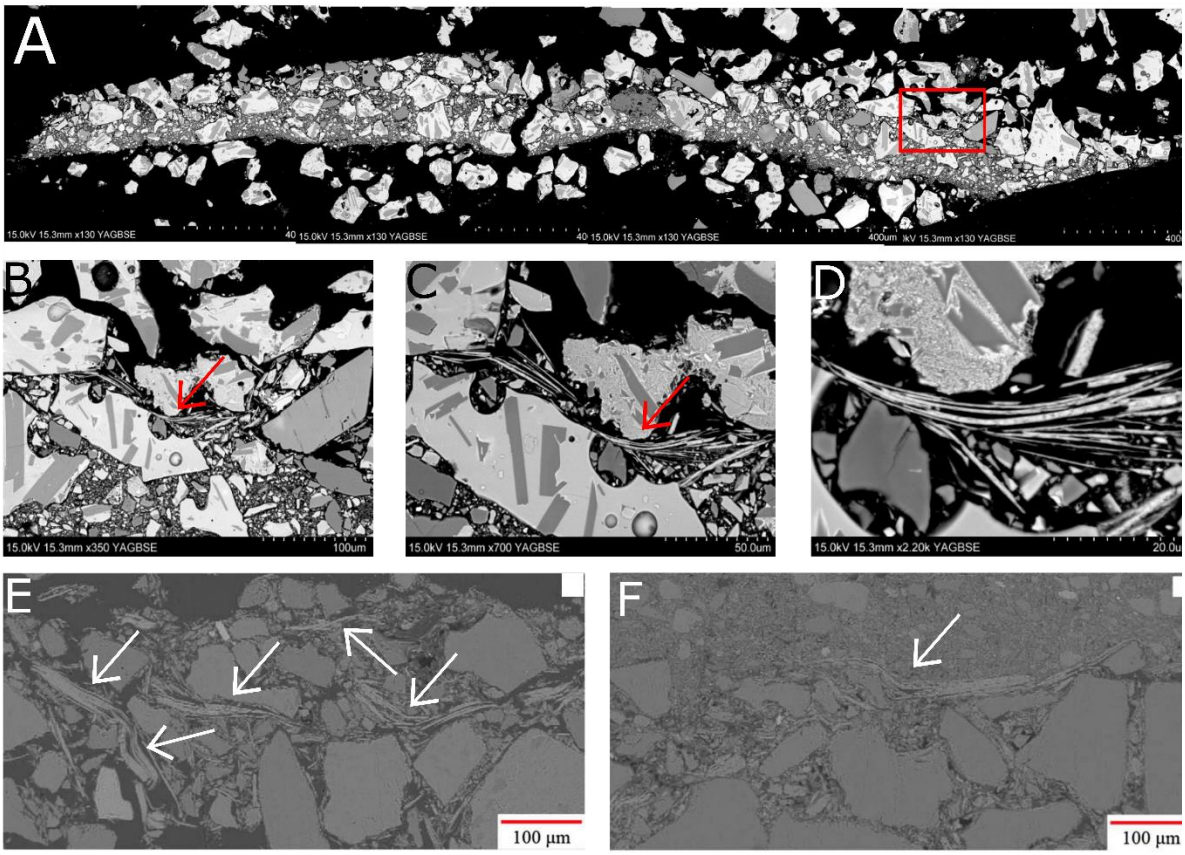

Figure 4.5 A) Sample from experiment HV2S, red box shows the location of the grain splintering B-D) Grain splintering feature shown at increasing scales, E-F) Samples from Wang, 2017 showing similar features, E is from an experiment run at 0.07m/s at 1.47MPa normal load and F is from an experiment run at 0.26m/s at 1.47MPa normal load.

4.9 Micromechanical Interpretations

4.9.1 Slip Nucleation & Sub-Seismic Velocity Experimental Data

Rate and state values of *a,* the direct effect, and *b,* the evolution effect, are parameters used to calculate *a-b*, which is a material property corresponding to velocity weakening or velocity strengthening behaviour. Potential unstable sliding occurs when *a-b* is < 0, when material is velocity weakening, and stable sliding when *a-b* is > 0, showing material is velocity strengthening (Marone, 1998).

Data from Chapter III suggest the material is more stable and velocity strengthening when saturated, suggesting frictional stability by slow sliding and creep behaviour. This implies that the addition of water into the system, for example meteoric water, would stabilise the system during slip nucleation. Conversely, dry conditions favour frictional instability during sliding. Similar findings from shearing experiments on powdered basalt suggest this may be attributed to a greater dilation effect on the

powder during wet experiments resulting in higher excess work against normal stress and greater frictional resistance as velocity increases (Giacomel et al., 2021; Marone et al., 1990).

4.9.2 Slip Propagation & Seismic Velocity Experimental Data

Data from Figures 3.14 A and B show that saturated conditions during slip propagation weaken the simulated gouges. Similarly, Figure 3.14 C shows that at seismic slip rates wet material weakens over a shorter distance than dry material. The same has been observed on similar rotary shear experiments on disaggregated ultracataclasite and in carbonate powders, showing that water leads to weakening behaviour as observed by greater friction coefficients on dry samples (Kitajima et al., 2010; Ferri et al., 2011).

These data provide evidence that water promotes a dynamic weakening mechanism within the material and that the addition of water would facilitate efficient sliding at higher speeds and accelerate sliding.

4.10 Implications of Mechanical Findings for Volcanic Edifice Collapse

The presence of water in the scoria gouge affects the mechanical behaviour of the material differently during the nucleation and propagation stages of slip. During slip nucleation, water would promote material strengthening and cohesion, whereas during slip propagation, water would aid weakening and favour faster sliding. Thus, the nucleation phase may have taken longer if the material was saturated to begin with, and slip may have started as slow creep. However, once sliding begun the presence of fluid would have facilitated and accelerated sliding.

The presence of shear localisation itself, which is observed by the development of a PSZ in both the GMSZ and experimental shear zones, is known to induce and exacerbate velocity weakening behaviour (Giacomel et al., 2021). Additionally, it is understood that friction decreases with landslide velocity. This velocity-dependent frictional weakening would further facilitate a drop in friction during slip propagation (Lucas et al., 2014). Velocity weakening during sliding may have occurred due to several factors and mechanisms, as discussed below.

4.10.1 Pore Fluid Pressurisation

One such mechanism is pore pressure fluidisation, which is promoted by enhancing pore fluid pressure in granular flows (Valverde & Scoia-Hoyo, 2015) and is considered a dominant process in facilitating the characteristically high mobility and velocity weakening behaviour of collapse flows such as pyroclastic density currents (Sparks; 1978; Roche et al., 2004; Rait et al., 2012; Monserrat et al., 2012; Rowley et al., 2014; Perinotto et al., 2015). Fluidisation occurs when granular material behaves as a low-viscosity fluid by grains being suspended in gas or pore water, reducing the effects of frictional forces (Cas et al., 2011). For pore pressure fluidisation to occur, it is necessary for fluids to be firstly, present, and secondly, trapped within the system (De Paola et al., 2011; Chen et al., 2013). In the experimental runs, the addition of water to the powder in the saturated runs provided the presence of fluid, and in the Green Mountain VDAD, the development of flame structures and incomplete mixing of the heterolithic layer (outlined in Chapter 1) could be evidence for the presence of water during the VDA. In both the GMSZ and the experimental shear zones, the reduction in grain size and porosity, as low as 8% in Zone A of the GMSZ, would reduce the ability of pore water to escape, trapping it in the system. It is widely observed that the generation of shear zones in granular lithologies can act as a fluid barrier due to a decrease in porosity and permeability (e.g., Underhill & Woodcock, 1987; Fowels & Burley, 1994; Antonelini & Aydin, 1994; El Bied et al., 2002; Saillet & Wibberby, 2010; Ferri et al., 2011). This could explain why the saturated seismic velocity experimental runs are weaker than the room humidity runs in the laboratory experiments and may be extrapolated to the GMSZ. In this case, pore fluid pressurisation would weaken the PSZ, favouring sliding as seismic slip rates and facilitating velocity weakening behaviour. The material showing velocity weakening behaviour during slip propagation, especially with the addition of water, is in line with other findings that velocity weakening behaviour defines potentially unstable basaltic volcanic flanks such as Hawaiian and Etnean volcanoes (Alparone et al., 2013; Denlinger & Morgan, 2014; Azzaro et al., 2017).

The presence of water during the transport and emplacement of the Green Mountain VDA and formation of the GMSZ must have been exogenic, as there are no hydrous phyllosilicates or other minerals that would become unstable. Additionally, the volume of water must be significant within the deposit to allow for the formation of the large-

scale flame structures observed. This suggests that any water in the Green Mountain VDA was likely of meteoric origin.

The thermal pressurisation of pore fluids also results in pore pressure fluidisation. This occurs when the thermal expansion of water volumetrically exceeds the thermal expansion of pore space, dilating granular material and lowering bulk friction (Garagash and Rudnicki, 2003; Rice, 2006; Segall et al., 2010). This is observed in shallow crustal faults comprising fluid-saturated granular material is widely accepted as the dominant weakening mechanism at slip rates >0.1m/s (Sibson, 1973; Lachenbruch, 1980; Lachenbruch, 1980; Andrews, 2002; Wibberley & Shimamoto, 2005; Bizarri & Cocco, 2000; Rice, 2006; Schmitt et al., 2011). This process may have occurred in the GMSZ and the experimental run, however more work is required to constrain whether conditions to allow for significant thermal expansion in these settings.

4.10.2 Nanoparticle Lubrication

Another mechanism proposed to explain velocity weakening behaviour during sliding is nanoparticle lubrication. Nanoparticles are defined as particles <1μm in diameter that are generated during grain fragmentation during shearing (Wang, 2017). Nanoparticle lubrication defines the process of this fine-grained matrix material locally reducing effective normal pressure on coarse grains, thus reducing bulk frictional resistance, and aiding in fluidisation of granular masses (Hsü, 1975). This mechanism has been proposed as a dynamic weakening mechanism at the base of large rockfalls and as a key mechanism in seismic fault dynamic weakening (Han et al., 2011). However, it has been proposed that nanoparticle lubrication alone may not be sufficient to facilitate weakening (Yao et al., 2016), and more likely works synchronously with other processes such as pore pressure fluidisation.

The presence of nanoparticles in the GMSZ is shown in Figure 3.20, A-C and three examples of nanoparticles from experimental runs are shown in Figure 3.20, D-F, suggesting this mechanism could have facilitated frictional weakening. Evidence of cataclastic processes resulting in grain size reduction would suggest that these nanoparticles originated from the cataclastic breakdown of larger clasts.

It is established that nanoparticles facilitate and exacerbate velocity weakening behaviour (Han et al., 2001). However, there is no established critical concentration of

nanoparticles which must be present in order for nanoparticles to act as a facilitator of velocity weakening behaviour. Therefore, it is possible that nanoparticles were not a dominant facilitator of velocity weakening behaviour during the formation of the GMSZ, but their presence may have further facilitated, rather than impeded, weakening in addition to more dominant mechanisms such as pore pressure fluidisation and shear localisation.

4.11 Conceptual Model for Velocity Weakening Behaviour and the Generation of the GMSZ

Based on the evidence presented and explored above, a conceptual model for the processes acting to generate the shear zone within the Green Mountain collapse can be proposed. Evidence from the experimental lab and field observations suggest that (1) shear during the Green Mountain VDA and in the experimental runs is preferentially accommodated within a highly localised slip layer, (2) in both the Green Mountain and experimental shear zones, a brittle cataclastic regime dominated to accommodate strain, resulting in grain size reduction, porosity reduction, and grain geometry evolution, (3) velocity weakening behaviour, as observed through experimental mechanical data, may be attributed to pore fluid pressurisation resulting from the presence of water, of which there is evidence in the Green Mountain VDA, shown by the presence of flame structures and incomplete mixing of the heterolithic lithology, (4) nanoparticle lubrication, in addition to pore fluid pressurisation, is a further proposed mechanism to facilitate mechanical weakening, with the presence of nanoparticles observed in both the GMSZ and experimental shear zones. This proposed model is presented in Figure 4.6.

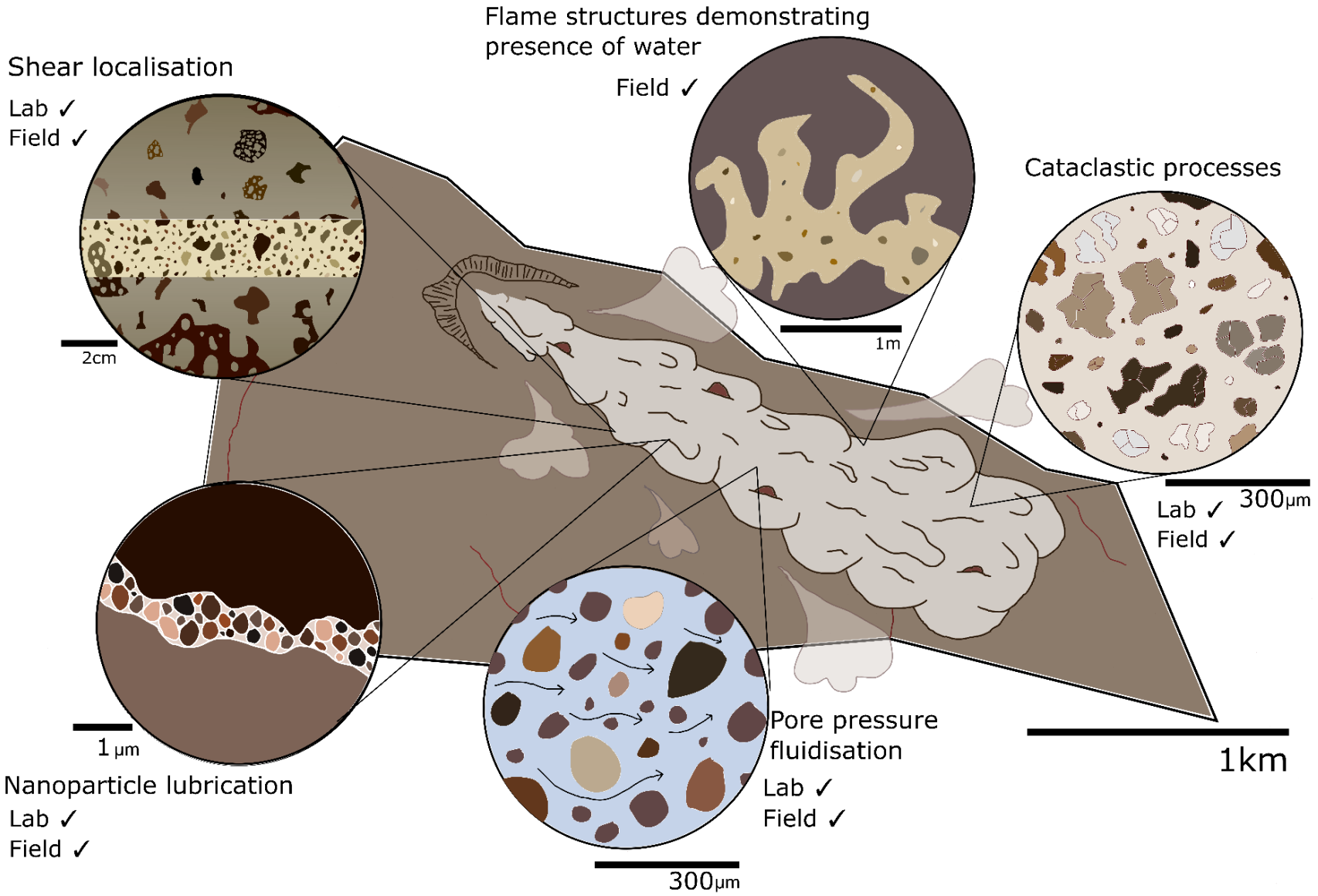

Figure 4.6 Proposed mechanisms of shear zone generation and frictional weakening during the Green Mountain volcanic debris avalanche, pulling together field and laboratory evidence.

Chapter V

5.1 Scope for Further Work

The work and findings described in this thesis could be used as a foundation for further research into the Green Mountain shear zone and its formation. Recommended work that was outside the scope of this project or that was limited by time constraints includes:

1) Conducting repeats of existing experimental work and conducting further experimental work, over a wider range of normal load pressures, velocities, and saturation states to investigate further the impacts on mechanical and microstructural outputs,
2) Image analysis using Fiji on the experimental shear zones; this would allow for better quantitative comparison between the GMSZ and experimental shear zones in terms of grain size distribution, porosity, circularity, and solidity,
3) Further on-site field work to better constrain the spatial extent of the shear zone, detachment surface of the VDAD and extent of the collapse deposit.

5.2 Conclusions

Based on the evidence and observations presented in this thesis, several conclusions may be reached:

1) During the Green Mountain VDA, shear was highly localised along a 1-2cm sliding layer, and even more so along the PSZ in the centre. Resultingly, the GMSZ exhibits markedly different physical characteristics to the rest of the deposit, as well as clear microstructural evolution with depth. From the peripheries of the GMSZ towards the PSZ, or Zone A, quantitative image analysis reveals a decrease in grain size and porosity, and an increase in circularity and solidity of clasts. The above changes, as well as the presence of truncated clasts, are indicative of a brittle cataclastic regime during shear.
2) Microstructural analysis of experimental shear zones generated under differing normal stress, saturation, and velocity conditions on the LHVR reveal the development of a PSZ to accommodate strain. All of the experimental shear zones show, as with the GMSZ, a decrease in grain size, porosity, and increasing clast roundness and sphericity within the PSZ.

3) Micromechanical analysis from shearing experiments on Green Mountain scoria reveal that at sub-seismic velocities, replicating the slip nucleation phase, material saturation promotes velocity strengthening behaviour and cohesion. Conversely, at seismic velocities, replicating slip propagation, material saturation promotes velocity weakening behaviour, facilitating and favouring faster sliding.
4) Based on evidence from laboratory experiments and the field, a model for velocity weakening facilitation by pore pressure fluidisation and nanoparticle lubrication during the Green Mountain VDA is proposed. Firstly, there is evidence for the presence of water within the VDAD as shown by the incomplete mixing of the heterolithic layer and flame structures. Grain size and porosity reduction within the GMSZ and experimental shear zones would allow for the retention of water, preventing it from escaping the system, which may have facilitated pore pressure fluidisation. Secondly, the presence of nanoparticles is observed in both the GMSZ and experimental shear zones, allowing for nanoparticle lubrication working synchronously with pore pressure fluidisation to facilitate velocity weakening behaviour.

Overall, the work in this thesis has expanded upon investigation into shear dynamics during volcanic edifice collapse flows, specifically into those acting to generate a shear zone during a volcanic debris avalanche on Ascension Island. The quantitative analysis of this shear zone helps to constrain the ways in which strain localisation is translated into microstructural organisation. The experimental work conducted has provided information on possible micromechanical and microstructural processes transpiring during the shearing of Green Mountain scoria and, importantly, its behaviour under saturated and room humidity states. Put together, evidence and observations from these micro-scale structural and mechanical findings can be used to build a more comprehensive proposal of the dynamics during the Green Mountain volcanic debris avalanche. More widely, this work contributes to the understanding of internal shear processes acting within gravitational collapse flows, the comprehension of which is crucial to constrain physical behaviour and mitigate associated risks.

Appendix

Appendix 1: Raw Data of Clast Parameters within GMSZ Zones from Image Analysis Using Fiji

	Zone A				
	Image 1	Image 2	Image 3	Image 4	Image 5
Diameter of 25 largest clasts (µm)	83	222	38	106	186
	100	138	96	52	354
	42	109	82	55	179
	48	120	42	82	136
	44	134	64	49	77
	57	91	109	125	124
	120	54	102	54	138
	98	57	71	41	82
	106	77	52	46	73
	43	105	51	47	76
	72	69	89	218	63
	83	96	91	65	101
	80	68	74	45	82
	56	115	52	80	86
	53	40	42	74	65
	73	56	84	105	51
	90	68	74	47	53
	42	76	59	86	52
	84	100	55	70	60
	40	87	36	42	48
	83	88	100	83	56
	60	91	69	67	46
	103	39	60	70	47
	68	45	77	150	35
	54	60	48	81	54
Mean clast diameter (µm)	72	89.375	69.5417	77.4583	94.5833
Maximum clast diameter (µm)	72.5	89.5	70	66	76.5
Porosity (%)	17.48	12.67	8.45	10.2	11.2
Circularity	0.721	0.631	0.703	0.738	0.665
Solidity	0.926	0.874	0.902	0.923	0.891

	Zone B'			Zone B		
	Image 1	Image 2	Image 3	Image 1	Image 2	Image 3
Diameter of 25 largest clasts (µm)	56	154	336	155	280	535
	122	119	135	107	161	149
	48	59	75	70	152	67
	72	43	26	108	94	65
	40	55	44	48	107	85
	355	126	315	125	92	90
	67	73	186	116	102	85
	52	64	55	87	194	69
	80	50	30	88	122	102
	41	67	28	35	81	63
	307	97	104	138	97	59
	49	110	117	82	74	67
	50	61	62	108	81	127
	171	62	32	65	111	129
	90	72	27	45	96	104
	54	144	97	209	135	105
	67	79	58	159	54	131
	78	97	39	72	96	151
	115	44	38	70	68	142
	39	74	26	38	76	53
	53	90	137	139	88	81
	117	109	53	185	65	62
	70	128	43	103	70	85
	93	60	62	52	71	73
	103	45	28	32	73	56
Mean clast diameter (µm)	95.25	84.875	88.5417	100.167	106.958	111.625
Maximum clast diameter (µm)	67	73.5	56.5	97.5	96	87.5
Porosity (%)	20.8	18.19	22.5	15.59	22.87	19.49
Circularity	0.648	0.606	0.623	0.648	0.657	0.629
Solidity	0.889	0.872	0.873	0.896	0.905	0.874

	Zone C'			Zone C		
	Image 1	Image 2	Image 3	Image 1	Image 2	Image 3
Diameter of 25 largest clasts (µm)	244	336	196	167	312	362
	239	190	112	144	176	81
	213	61	83	140	89	101
	203	103	115	98	135	100
	170	240	35	97	75	126
	161	80	142	97	93	161
	158	74	59	246	113	122
	150	109	90	117	95	147
	150	119	69	146	82	80
	137	188	47	124	71	82
	133	97	131	216	64	94
	117	76	90	133	84	95
	98	182	71	89	88	67
	96	104	59	82	112	123
	95	70	36	57	93	138
	91	81	159	98	99	67
	91	115	60	59	151	96
	90	116	85	74	100	126
	87	107	54	90	60	106
	79	76	42	52	102	203
	78	86	97	60	62	88
	70	78	57	88	68	133
	63	63	72	68	85	124
	60	27	60	892	53	82
	55	60	44	57	50	114
Mean clast diameter (µm)	128.042	115.75	84.2083	139.64	100.48	120.72
Maximum clast diameter (µm)	244	336	196	892	312	362
Porosity (%)	31.04	26.93	30.11	21.673	32.27	27.16
Circularity	0.553	0.562	0.629	0.591	0.683	0.661
Solidity	0.848	0.839	0.869	0.854	0.919	0.903

	Zone D'				Zone D			
	Image 1	Image 2	Image 3	Image 4	Image 1	Image 2	Image 3	Image 4
Diameter of 25 largest clasts (µm)	458	231	269	448	170	457	139	186
	305	356	191	271	79	141	111	152
	361	207	210	185	102	179	90	150
	146	105	222	153	139	107	124	77
	111	141	243	203	79	169	162	127
	411	102	247	205	244	157	151	146
	422	61	218	123	78	126	227	187
	447	76	189	104	64	115	177	123
	185	70	166	148	45	90	146	121
	100	79	149	93	68	96	85	69
	239	67	235	92	205	124	200	143
	207	77	128	129	136	118	89	148
	145	7	91	124	50	69	139	104
	101	98	88	97	171	103	132	64
	87	109	273	69	138	61	101	62
	173	75	233	85	176	71	180	85
	122	78	208	98	52	80	108	86
	177	52	197	102	173	76	429	142
	117	79	99	94	180	62	112	82
	78	73	178	84	53	70	88	66
	234	56	155	70	93	62	124	141
	401	51	124	70	76	61	72	142
	155	65	92	54	112	117	114	117
	109	33	80	89	200	68	128	59
	71	41	112	78	138	59	104	65
Mean clast diameter (µm)	214.48	95.56	175.88	130.72	120.84	113.52	141.28	113.76
Maximum clast diameter (µm)	458	356	273	448	244	457	429	187
Porosity (%)	47	40.8	63.2	30.12	45.241	52.77	39.9	48.9
Circularity	0.344	0.498	0.351	0.477	0.411	0.376	0.395	
Solidity	0.663	0.641	0.7	0.792	0.758	0.749	0.762	

	Zone E'			
	Slide 1	Slide 2	Slide 3	Slide 4
Diameter	6500	5200	5000	3100
	7000	5300	4500	2000
	5500	6000	3400	2500
	2000	3100	2300	2100
	2000	3400	5700	1600
	1500	4200	3200	3400
Diameter	Zone E			
	Slide 1	Slide 2	Slide 3	Slide 4
	2800	5100	4000	8700
	7200	4300	3500	4500
	3800	3700	3200	3100
	2300	2400	2500	3400
	3900	2100	5000	2000
	2200	6000	3000	2500

Appendix 2: Raw Data of Volume vs Runout and corresponding references used in Figure 4.1

Volcano (alphabetical)	Runout (km)	Volume (km^3)	Reference
Acatenango	41.0	5	Vallance et al. (1995)
Akagi	19.0	4	Hayashi & Self (1992)
Akagi (Nashigi)	23.5	6	Yoshida et al. (2012)
Antuco	30.0	15	Moreno (1991)
Asakusa	6.5	0.04	Hayashi & Self (1992)
Asama	20.0	2	Hayashi & Self (1992)
Augustine	10.0	0.35	Beget & Kienle (1992)
Avachinsky	30.0	8	Melekestsev et al. (1992)
Bandai-san	11.0	1.5	Hayashi & Self (1992)
Bezymianny	8	0	Bogoiavlenskaia (1962)
Callaqui	15.0	0.15	Hayashi & Self (1992)
Canlaon	33.0	13	Geronimo-Cantane (1997)
Chaos Crags	5.0	0.15	Hayashi & Self (1992)
Chimborazo	35.0	8.1	Hayashi & Self (1992)
Chokai	25.0	3.5	Hayashi & Self (1992)
Citlaltépetl (Jamapa)	75.0	25	Carrasco-Nuñez et al. (2006)
Citlaltépetl (Teteltzingo)	110.0	2.2	Carrasco-Nuñez et al. (2006)
Colima	40.0	12.5	Hayashi & Self (1992)
Colima (La Lumbre-Los Ganchos)	25.0	1.7	Cortés et al. (2010)
Colima (Paleofuego)	70.0	10	Luhr & Prestegaard (1985)
Colima (San Marcos)	20.0	1.3	Roverato et al. (2011)
Drum	85.0	7	Richter et al. (1979)
Egmont	39.0	5.8	Palmer et al. (1991)
Egmont (Opua)	27.0	0.35	Hayashi & Self (1992)
Egmont (Pungarehu)	31.0	7.5	Palmer et al. (1991)
Fuego	50.0	15	e.g., Vallance et al. (1995)
Fuji (Gotemba)	24.0	1.8	Yoshida et al. (2012)
Galunggung	25.0	2.9	Hayashi & Self (1992)
Galunggung	23.0	16	Bronto (1989)
Green Mountain	2	0	
Hanang	15.2	0	Delcamp et al., (2016)
Iizuna	17.0	5	Kawachi & Hayatsu (1994)
Iriga	11.0	1.5	Hayashi & Self (1992)
Iwaki	14.0	1.3	Hayashi & Self (1992)
Jocotitlán	12.0	2.8	Siebert et al. (1992)
Kerimasi	15	0	Delcamp et al., (2016)
Kibo	65	0	Delcamp et al., (2016)

Komagatake (Onuma)	11.5	0.25	Hayashi & Self (1992)
Kurohime	6.0	0.12	Hayashi & Self (1992)
Las Cumbres	120.0	60	Carrasco-Nuñez et al. (2006)
Mawenzi	60.0	7.1	Hayashi & Self (1992)
Mawenzi	54	0	Siebert (1984)
Meru	50.0	15	Hayashi & Self (1992)
Mombacho (El Crater)	12.4	1.75	Shea et al. (2008)
Mombacho (Las Isletas)	11.9	1.2	Shea et al. (2008)
Momella	52	0	Siebert (1984)
Monbacho	12.0	1	Hayashi & Self (1992)
Mt Iriga	12.0	1.5	Paguican et al. (2012)
Mt Iriga	16.0	2	Paguican et al. (2012)
Mt Shasta	43	26	Crandell et al., (1984)
Mt St Helens	20	0	Glicken (1996)
Mt St Helens 20 000 BP	16.0	1	Siebert (1984)
Myoko (Sekikawa)	19.0	0.8	Hayashi & Self (1992)
Myoko (Taguchi)	8.0	0.23	Hayashi & Self (1992)
Nasu (Nashigi)	19.0	1	Yoshida et al. (2012)
Nevado de Colima	65	33	Luhr & Prestegaard (1988)
Nevado de Toluca	8.0	0.52	Capra et al. (2012)
Ovalnaya Zimina	17.0	0.4	Hayashi & Self (1992)
Papandayan	11.0	0.14	Hayashi & Self (1992)
Parinacota	22.0	6	Clavero et al. (2002)
Picchu Picchu	21	0	Hughes et al.,(2020)
Pico de Orizaba	70.0	20	Carrasco-Nunez et al. (1997)
Planchon-Peteroa	78.0	10	Naeanjo et al. (1997)
Popa	11.0	0.8	Hayashi & Self (1992)
Popocatepetl	60.0	9	Siebert et al. (1995)
Popocatepetl	33.0	28	Hayashi & Self (1992)
Pouakai (Maitahi)	30.0	7.5	Gaylord & Neall (2012)
Raung	79.0	25	Siebert et al. (1996)
Ruapehu	60	2.9	Tost et al., (2014)
Ruapehu	80	3	Tost et al., (2014)
Ruapehu	50	1.56	Tost et al., (2014)
Ruapehu	60	2.4	Hodgeson1(993)
Ruapehu (Murimotu)	13.0	0.2	Palmer & Neall (1989)
Santa Ana (Acajutla)	50.0	16	Siebert et al. (2004)
Saxicun	1.2	0	Gao et al., (2004)
Shasta	50.0	26	Hayashi & Self (1992)
Shasta	49.0	46	Crandell (1989)
Shiribetsu (Rusutsu)	7.5	2	Yoshida et al. (2012)
Shiveluch	12.0	1.5	Hayashi & Self (1992)
Shiveluch	35.0	35	Belousov et al. (1999)

Sierra Veluda	25.0	0.5	Hayashi & Self (1992)
Socompa	35.0	17	Hayashi & Self (1992)
Socompa	35.0	25.7	Wadge et al. (1995)
Socompa	40	36	Le Corvec (2005)
Soufriere	9	0	Boudon et al., (1987)
Soufrière	9.5	0.5	Siebert (1984)
Soufrière Hills	4.5	0.005	Voight et al. (2002)
Tancitaro	73.0	18	Morelli et al. (2010)
Tashirodake	12.4	0.1	Takarada et al. (1999)
Tata Sabaya	23.0	6	Godoy et al. (2012)
Tateshina	12.5	0.35	Hayashi & Self (1992)
Toluca	55.0	5	Arce & Marcias (2003)
Tongariro (Te Whaiau)	15.0	0.5	Lecointre et al. (2001)
Unzen	6.5	0.34	Hayashi & Self (1992)
Usu	6.5	0.3	Hayashi & Self (1992)
Usu (Zenkoji)	6.5	1.5	Yoshida et al. (2012)
Vesuvius	0.6	0.0002	Hazlett et al. (1991)
Vesuvius	0.9	0.0009	Hazlett et al. (1991)
Vesuvius	0.5	0.0006	Hazlett et al. (1991)
Vesuvius	1.0	0.0008	Hazlett et al. (1991)
Vesuvius	1.2	0.001	Hazlett et al. (1991)
Vesuvius	0.7	0.0011	Hazlett et al. (1991)
Vesuvius	0.8	0.0012	Hazlett et al. (1991)
Volcán de Colima	65.0	12	Stoopes & Sheridan (1992)
Volcan de Colima	43	10	Stoops & Sheridan (1992)
Wrangell	70.0	12.6	Yehle & Nichols (1980)
Yatsugatake (Nirasaki)	32.0	9	Hayashi & Self (1992)
Yatsugatake (Otsukigawa)	12.5	0.27	Hayashi & Self (1992)

References

Acocella, V., Puglisi, G., 2010. Hazard mitigation of unstable volcanic edifices. EOS Trans 91. https://doi.org/10.1029/2010EO400002.

Alparone, S., Cocina, O., Gambino, S., Mostaccio, A., Spampinato, S., Tuvè, T. and Ursino, A., 2013. Seismological features of the Pernicana–Provenzana Fault System (Mt. Etna, Italy) and implications for the dynamics of northeastern flank of the volcano. Journal of volcanology and geothermal research, 251, pp.16-26.

Al-Harthi, A.A., Al-Amri, R.M. and Shehata, W.M., 1999. The porosity and engineering properties of vesicular basalt in Saudi Arabia. Engineering Geology, 54(3-4), pp.313-320.

Alloway B, McComb P, Neall V, Vucetich C, Gibb J, Sherburn A, Stirling M (2005) Stratigraphy, age, and correlation of voluminous debris-avalanche events from ancestral Egmont Volcano: implications for coastal plain construction and regional hazard assessment. J Royal Soc New Zealand 35(1–2):299–267

Andrews, D., 2002. A fault constitutive relation accounting for thermal pressurization of pore fluid. J. Geophys. Res. 107 (B12), 2363. http://dx.doi.org/10.1029/2002JB001942

Anthony JL, Marone C (2005) Influence of particle characteristics on granular friction. J Geophys Res 110:B08409

Antonellini, M. and Aydin, A., 1994. Effect of faulting on fluid flow in porous sandstones: petrophysical properties. AAPG bulletin, 78(3), pp.355-377.

Arce, J.L., Macías, J.L. and Vázquez-Selem, L., 2003. The 10.5 ka Plinian eruption of Nevado de Toluca volcano, Mexico: Stratigraphy and hazard implications. Geological Society of America Bulletin, 115(2), pp.230-248.

Atkins, F. B., P. E. Baker, J. D. Bell, and D. G. W. Smith, 1964, Oxford expedition to Ascension Island, Nature, 204, 722 – 724

Auker MR, Sparks RSJ, Siebert L, Crosweller HS, Ewert J (2013) A statistical analysis of the global historical volcanic fatalities record. J Appl

Azzaro, R., D'Amico, S., Peruzza, L. and Tuvè, T., 2013. Probabilistic seismic hazard at Mt. Etna (Italy): the contribution of local fault activity in mid-term assessment. Journal of volcanology and geothermal research, 251, pp.158-169.

Bar-Sinai, Y., Spatschek, R., Brener, E. et al., 2015. Velocity-strengthening friction significantly affects interfacial dynamics, strength and dissipation. Sci Rep 5, 7841 https://doi.org/10.1038/srep07841

Begét, J.E. and Kienle, J., 1992. Cyclic formation of debris avalanches at Mount St Augustine volcano. Nature, 356(6371), pp.701-704.

Belousov AB, Belousova MG, Voight B, 1999. Multiple edifice failures, debris avalanches and associated eruptions in the Holocene history of Shiveluch volcano, Kamchatka, Russia. Bull Volcanol 61:324– 342

Bernard B, van Wyk de Vries B, Leyrit H, 2009, Distinguishing volcanic debris avalanche deposits from their reworked products: the perrier sequence (French Massif Central). Bull Volc 71:1041–1056

Bernard K, Thouret J-C, van Wyk de Vries B (2017) Emplacement and transformations of volcanic debris avalanches—a case study at El Misti volcano, Peru. J Volcanol Geotherm Res 340:68–91

Bernard K, van Wyk de Vries B, Thouret J.-C. (2019) Fault textures in volcanic debris-avalanche deposits and transformations into lahars: the Pichu Pichu thrust lobes in south Peru compared to worldwide avalanche deposits. J Volcanol Geotherm Res 371:116–136

Bernard, B., Takarada, S., Andrade, S.D. and Dufresne, A., 2021. Terminology and strategy to describe large volcanic landslides and debris avalanches. In Volcanic Debris Avalanches (pp. 51-73). Springer, Cham.

Billi A (2005) Grain size distribution and thickness of breccia and gouge zones from thin (< 1 m) strike-slip fault cores in limestone. J Struct Geol 27(10):1823– 1837

Blenkinsop, T.G., 1991. Cataclasis and processes of particle size reduction. pure and applied geophysics, 136(1), pp.59-86.

Bogoiavlenskaia, G.E., 1962. Agglomerate flow Bezymianny volcano. Bulletin Volcanologique, 24(1), pp.203-210.

Bonforte, A., Guglielmino, F. and Puglisi, G., 2019. Large dyke intrusion and small eruption: The December 24, 2018 Mt. Etna eruption imaged by Sentinel-1 data. *Terra Nova*, *31*(4), pp.405-412.

Boudon, G., Semet, M.P. and Vincent, P.M., 1987. Magma and hydrothermally driven sector collapses: The 3100 and 11,500 y. BP eruptions of la Grande Decouverte (la Soufriere) volcano, Guadeloupe, French West Indies. Journal of Volcanology and Geothermal Research, 33(4), pp.317-323.

Borradaile, G.J., 1981. Particulate flow of rock and the formation of cleavage. Tectonophysics, 72(3-4), pp.305-321.

Braitseva, O.A., Melekestsev, I.V., Ponomareva, V.V., Kirianov, V.Y., Litasova, S.N. and Sulerzhitsky, L.D., 1992. Tephra of the largest prehistoric Holocene volcanic eruptions in Kamchatka. Quaternary International, 13, pp.177-180.

Brideau M-A, Procter JN (2005) Discontinuity orientation in jigsaw clasts from volcanic debris avalanche deposits and implications for emplacement mechanism. GEOQuébec, 8p

Bronto, S., 1989. Volcanic geology of Galunggung, west java, Indonesia.

Brunet M, Moretti L, Le Friant A, Mangeney A, Fernandez-Nieto ED, Bouchut F (2017) Numerical simulation of the 30–45 ka debris avalanche flow of Montagne Pelée volcano, Martinique: from volcano flank collapse to submarine emplacement. Nat Haz 87 (2):1189–1222

Caballero L, Capra L (2011) Textural analysis of particles from El Zaguán debris avalanche deposit, Nevado de Toluca volcano, Mexico: evidence of flow behavior during emplacement. J Volcanol Geotherm Res 200:75–82

Cagnoli, B. and Manga, M., 2004. Granular mass flows and Coulomb's friction in shear cell experiments: Implications for geophysical flows. Journal of Geophysical Research: Earth Surface, 109(F4).

Cagnoli, B. and Romano, G.P., 2013. Vertical segregations in flows of angular rock fragments: Experimental simulations of the agitation gradient within dense geophysical flows. Journal of volcanology and geothermal research, 265, pp.52-59.

Calder, E.S., Luckett, R., Sparks, R.S.J., Voight, B., 2002. Mechanisms of lava dome instability and generation of rockfalls and pyroclastic flows at Soufri`ere Hills Volcano, Montserrat. Geol Soc, London, Memoirs 21, 173–190. https://doi.org/ 10.1144/GSL.MEM.2002.021.01.08.

Campbell, C.S., Cleary, P.W., Hopkins, M., 1995. Large-scale landslide simulations: global deformation, velocities and basal friction. J. Geophys. Res.: Solid Earth 100, 8267–8283. https://doi.org/10.1029/94JB00937.

Carrasco-Núñez, G., Díaz-Castellón, R., Siebert, L., Hubbard, B., Sheridan, M.F. and Rodríguez, S.R., 2006. Multiple edifice-collapse events in the Eastern Mexican Volcanic Belt: the role of sloping substrate and implications for hazard assessment. Journal of Volcanology and Geothermal Research, 158(1-2), pp.151-176.

Cas, R. A. F., H. M. N. Wright, C. B. Folkes, C. Lesti, M. Porreca, G. Giordano, and J. G. Viramonte (2011), The flow dynamics of an extremelylarge volume pyroclastic flow, the 2.08-Ma Cerro Galán Ignimbrite, NW argentina, and comparison with other flow types,Bull. Volcanol.,73(10), 1583–1609

Cascini, L., Cuomo, S., Pastor, M. and Sacco, C., 2013. Modelling the post-failure stage of rainfall-induced landslides of the flow type. Canadian Geotechnical Journal, 50(9), pp.924-934.

Cecchi, E., van Wyk de Vries, B., Lavest, J.-M., 2004. Flank spreading and collapse of weak-cored volcanoes. Bull. Volcanol. 67, 72–91. https://doi.org/10.1007/s00445- 004-0369-3

Chen, J., Yang, X., Duan, Q., Shimamoto, T., Spiers, C.J., 2013. Importance of thermochemical pressurization in the dynamic weakening of the Longmenshan Fault during the 2008 Wenchuan earthquake: inferences from experiments and modeling.

Chen, J., Dai, F., Xu, L., Chen, S., Wang, P., Long, W. and Shen, N., 2014. Properties and microstructure of a natural slip zone in loose deposits of red beds, southwestern China. *Engineering Geology*, *183*, pp.53-64.

Chester, D.K., Degg, M., Duncan, A.M. and Guest, J.E., 2000. The increasing exposure of cities to the effects of volcanic eruptions: a global survey. *Global Environmental Change Part B: Environmental Hazards*, *2*(3), pp.89-103.

Chu J., Leroueil S., and Leong W.K. 2003. Unstable behaviour of sand and its implication for slope instability. Canadian Geotechnical Journal, 40(5): 873–885.

Clavero J, Sparks R, Huppert H, Dade W (2002) Geological constraints on the emplacement mechanism of the Parinacota debris avalanche, Northern Chile. Bull Volcanol 64:40–54. https://doi.org/10. 1007/s00445-001-0183-0

Clavero JE, Sparks RSJ, Pringle MS, Polanco E, Gardeweg MC (2004) Evolution and volcanic hazards of Taapaca volcanic complex, Central Andes of Northern Chile. J Geol Soc 161:603–618. https://doi. org/10.1144/0016-764902-065

Cortés, A., Garduño, V.H., Macías, J.L., Navarro-Ochoa, C., Komorowski, J.C., Saucedo, R. and Gavilanes, J.C., 2010. Geologic mapping of the Colima volcanic complex (Mexico) and implications for hazard assessment. Stratigraphy and Geology of Volcanic Areas, 464, pp.249-264.

Crandell, D.R., Miller, C.D., Glicken, H.X., Christiansen, R.L. and Newhall, C.G., 1984. Catastrophic debris avalanche from ancestral Mount Shasta volcano, California. Geology, 12(3), pp.143-146.

Crandell DR (1989) Gigantic Debris avalanche of Pleistocene age from Ancestral Mount Shasta Volcano, California, and Debris-Avalanche Hazard Zonation: U.S. Geol Surv Bull 1861:29

Dai, F., Lee, C.F., Wang, S. and Feng, Y., 1999. Stress–strain behaviour of a loosely compacted volcanic-derived soil and its significance to rainfall-induced fill slope failures. Engineering Geology, 53(3-4), pp.359-370.

Darve, F. and Laouafa, F., 2000. Instabilities in granular materials and application to landslides. Mechanics of Cohesive-frictional Materials: An International Journal on Experiments, Modelling and Computation of Materials and Structures, 5(8), pp.627-652.

Davies, T.R., McSaveney, M.J. and Beetham, R.D., 2006. Rapid block glides: slide-surface fragmentation in New Zealand's Waikaremoana landslide. Quarterly Journal of Engineering Geology and Hydrogeology, 39(2), pp.115-129.

Davies, T.R. and McSaveney, M.J., 2009. The role of rock fragmentation in the motion of large landslides. Engineering Geology, 109(1-2), pp.67-79.

Davies, T., McSaveney, M. and Kelfoun, K., 2010. Runout of the Socompa volcanic debris avalanche, Chile: a mechanical explanation for low basal shear resistance. *Bulletin of Volcanology*, *72*(8), pp.933-944.

Dawood, F., 2021. Data Processing Script for Experiments In Rotary Apparatus, Rock Mechanics Laboratory, Durham Univserity. MatLab R.2022a.

De Blasio, F.V. and Crosta, G.B., 2014. Simple physical model for the fragmentation of rock avalanches. Acta Mechanica, 225(1), pp.243-252.De Blasio, F.V. and Elverhøi, A., 2008. A model for frictional melt production beneath large rock avalanches. Journal of Geophysical Research: Earth Surface, 113(F2).

De Blasio, F.V., 2011. Landslides in Valles Marineris (Mars): a possible role of basal lubrication by sub-surface ice. Planet. Space Sci. 59, 1384–1392. https://doi.org/ 10.1016/J.PSS.2011.04.015.

De Paola, N., Hirose, T., Mitchell, T., Di Toro, G., Viti, C., Shimamoto, T., 2011. Fault lubrication and earthquake propagation in thermally unstable rocks. Geology 39 (1), 35e38. http://dx.doi.org/10.1130/G31398.1.

De Paola, N., Holdsworth, R.E., Viti, C., Collettini, C. and Bullock, R., 2015. Can grain size sensitive flow lubricate faults during the initial stages of earthquake propagation?. *Earth and Planetary Science Letters*, *431*, pp.48-58.

Delcamp, A., Delvaux, D., Kwelwa, S., Macheyeki, A. and Kervyn, M., 2016. Sector collapse events at volcanoes in the North Tanzanian divergence zone and their implications for regional tectonics. *Bulletin*, *128*(1-2), pp.169-186.

Denlinger, R.P. and Morgan, J.K., 2014. Instability of Hawaiian volcanoes. Characteristics of Hawaiian volcanoes, 1801, pp.149-176.

Di Toro G, Goldsby DL, Tullis TE (2004) Friction falls towards zero in quartz rock as slip velocity approaches seismic rates. Nature 427:436–439

Di Toro, G., Han, R., Hirose, T., De Paola, N., Nielsen, S., Mizoguchi, K., Ferri, F., Cocco, M. and Shimamoto, T., 2011. Fault lubrication during earthquakes. Nature, 471(7339), pp.494-498.

Donnadieu, F., Merle, O. and Besson, J.C., 2001. Volcanic edifice stability during cryptodome intrusion. Bulletin of Volcanology, 63(1), pp.61-72.

Dufresne, A., C. Prager, and A. S. Bösmeier (2015), Insights into rock avalanche emplacement processes by detailed morpho-lithologicalstudies of the Tschirgant deposit (Tyrol Austria),Earth Surf. Processes Landforms,41(5), 587–602.

Dufresne, A., Zernack, A., Bernard, K., Thouret, J.C. and Roverato, M., 2021. Sedimentology of volcanic debris avalanche deposits. In Volcanic Debris Avalanches (pp. 175-210). Springer, Cham.

Dunning, S. A., 2004. Rock avalanches in high mountains—A sedimentological approach, PhD thesis, Univ. of Luton, U. K

El Bied, A., Sulem, J. and Martineau, F., 2002. Microstructure of shear zones in Fontainebleau sandstone. International Journal of Rock Mechanics and Mining Sciences, 39(7), pp.917-932.

Engelder, T. (1987). Cataclastic rocks . In: Structural Geology and Tectonics. Encyclopedia of Earth Science. Springer, Berlin, Heidelberg. https://doi.org/10.1007/3-540-31080-0_9

Erismann, T., Abele, G., 2001. Dynamics of rockslides and rockfalls. https://doi.org/10. 1007/978-3-662-04639-5.

Ferri, F., Di Toro, G., Hirose, T., Han, R., Noda, H., Shimamoto, T., Quaresimin, M., de Rossi, N., 2011. Low- to high-velocity frictional properties of the clay-rich gouges from the slipping zone of the 1963 Vaiont slide, northern Italy. J. Geophys. Res.: Solid Earth 116. https://doi.org/10.1029/2011JB008338

Fondriest, M., S. Aretusini, G. Di Toro, and S. A. Smith (2015), Fracturing and rock pulverization along an exhumed seismogenic fault zone indolostones: The Foiana Fault Zone (Southern Alps, Italy),Tectonophysics,654,56–74

Fowles, J. and Burley, S., 1994. Textural and permeability characteristics of faulted, high porosity sandstones. Marine and Petroleum Geology, 11(5), pp.608-623.

Fukuoka, H., Sassa, K., Wang, G. and Sasaki, R., 2006. Observation of shear zone development in ring-shear apparatus with a transparent shear box. *Landslides*, *3*(3), pp.239-251.

Gao, Y., Yin, Y., Li, B., Feng, Z., Wang, W., Zhang, N. and Xing, A., 2017. Characteristics and numerical runout modeling of the heavy rainfall-induced catastrophic landslide–debris flow at Sanxicun, Dujiangyan, China, following the Wenchuan Ms 8.0 earthquake. Landslides, 14(4), pp.1361-1374.

Garagash, D.I. and Rudnicki, J.W., 2003. Shear heating of a fluid-saturated slip-weakening dilatant fault zone 1. Limiting regimes. Journal of Geophysical Research: Solid Earth, 108(B2).

Gaylord, D.R., and Neal, V.E., 2012, Subedifi ce collapse of an andesitic stratovolcano: The Maitahi Formation, Taranaki Peninsula, New Zealand: Geological Society of America Bulletin, v. 124, p. 181–199, doi: 10 .1130 /B30141 .1 .

Giacomel, P., Ruggieri, R., Scuderi, M.M., Spagnuolo, E., Di Toro, G. and Collettini, C., 2021. Frictional properties of basalt experimental faults and implications for volcano-tectonic settings and geo-energy sites. Tectonophysics, 811, p.228883.

Giardino, M. (2013). Debris Avalanche. In: Bobrowsky, P.T. (eds) Encyclopedia of Natural Hazards. Encyclopedia of Earth Sciences Series. Springer, Dordrecht. https://doi.org/10.1007/978-1-4020-4399-4_84

Glicken, H., 1986. *Rockslide-debris avalanche of May 18, 1980, Mount St. Helens volcano, Washington* (Doctoral dissertation, University of California, Santa Barbara.).

Glicken, H., 1991. Sedimentary architecture of large volcanic-debris avalanches.

Glicken H (1996) Rockslide-debris avalanche of May 18, 1980, Mount St. Helens volcano, Washington. US geological survey, open file report, vol 96–677, 90p

Godoy, B., Clavero, J., Rojas, C. and Godoy, E., 2012. Facies volcánicas del depósito de avalancha de detritos del volcán Tata Sabaya, Andes Centrales. Andean geology, 39(3), pp.394-406.

Google Earth (2021), available online at https://earth.google.com/web/ accessed 27.11.2021

Google Earth, 2022, available online at https://earth.google.com/web/, accessed 13.09.2022

Google Maps (2021), available online at https://www.google.com/maps/ accessed 28.12.2021

Han, R., T. Hirose, T. Shimamoto, Y. Lee, and J. I. Ando. 2011. Granular nanoparticles lubricate faults during seismic slip,Geology,39(6), 599–602

Haines, S.H., Kaproth, B., Marone, C., Saffer, D. and Van der Pluijm, B., 2013. Shear zones in clay-rich fault gouge: A laboratory study of fabric development and evolution. *Journal of Structural Geology*, *51*, pp.206-225.

Harris, C., Bell, J.D. and Atkins, F.B., 1982. Isotopic composition of lead and strontium in lavas and coarse-grained blocks from Ascension Island, South Atlantic. Earth and Planetary Science Letters, 60(1), pp.79-85.

Hayashi, J.N. and Self, S., 1992. A comparison of pyroclastic flow and debris avalanche mobility. Journal of Geophysical Research: Solid Earth, 97(B6), pp.9063-9071.

Hazlett, R.W., Buesch, D., Anderson, J.L., Elan, R. and Scandone, R., 1991. Geology, failure conditions, and implications of seismogenic avalanches of the 1944 eruption at Vesuvius, Italy. Journal of Volcanology and Geothermal Research, 47(3-4), pp.249-264.

Hermanns, R., 2013 ,"Rock Avalanche (Sturzstrom)", Encyclopedia of Natural Hazards, Encyclopedia of Earth Sciences Series, p. 875,

Hodgson KA (1993) Late quaternary lahars from Mount Ruapehu in the Whangaehu River valley, North Island, New Zealand. PhD thesis, Massey University, Palmerston North

Hsü, K. J. (1975), Catastrophic debris streams (sturzstroms) generated by rockfalls,Bull. Geol. Soc. Am.,86(1), 225–256

Hu, W., Huang, R., McSaveney, M., Yao, L., Xu, Q., Feng, M. and Zhang, X., 2019. Superheated steam, hot CO2 and dynamic recrystallization from frictional heat jointly lubricated a giant landslide: field and experimental evidence. Earth and Planetary Science Letters, 510, pp.85-93.coarse-grained blocks from Ascension Island, South Atlantic, Earth Planet. Sci. Lett., 60, 79 – 85

Hu, W. and McSaveney, M.J., 2018. A polished and striated pavement formed by a rock avalanche in under 90 s mimics a glacially striated pavement. Geomorphology, 320, pp.154-161.

Hughes, A., Kendrick, J.E., Salas, G., Wallace, P.A., Legros, F., Di Toro, G. and Lavallee, Y., 2020. Shear localisation, strain partitioning and frictional melting in a debris avalanche generated by volcanic flank collapse. Journal of Structural Geology, 140, p.104132.

Hunt, J.E., Cassidy, M., Talling, P.J., 2018. Multi-stage volcanic island flank collapses with coeval explosive caldera-forming eruptions. Sci. Rep. 8, 1146. https://doi.org/ 10.1038/s41598-018-19285-2.

Innocenzi, F., Ronca, S., Agostini, S., Brandano, M., Caracausi, A. and Lustrino, M., 2021. The pyroclastic breccias from Cabezo Negro de Tallante (SE Spain): Is there any relation with carbonatitic magmatism?. *Lithos*, *392*, p.106140

Iverson, R.M., Reid, M.E. and LaHusen, R.G., 1997. Debris-flow mobilization from landslides. Annual Review of Earth and Planetary Sciences, 25(1), pp.85-138.

Jiang, D. and White, J.C., 1995. Kinematics of rock flow and the interpretation of geological structures, with particular reference to shear zones. *Journal of Structural Geology*, *17*(9), pp.1249-1265.

Johnson, B.C., Campbell, C.S., Melosh, H.J., 2016. The reduction of friction in long runout landslides as an emergent phenomenon. J. Geophys. Res.: Earth Surface 121, 881–889. https://doi.org/10.1002/2015JF003751.

Kandel, M.E., Sridharan, S., Liang, J., Luo, Z., Han, K., Macias, V., Shah, A., Patel, R., Tangella, K., Kajdacsy-Balla, A. and Guzman, G., 2017. Label-free tissue

scanner for colorectal cancer screening. Journal of biomedical optics, 22(6), p.066016.

Kawachi, S. and Hayatsu, K., 1994. Debris avalanche and lahar deposits in the Yatsugatake Volcanic chain and Myoko Volcanic Group, Central Japan, Journal of natural disaster science, 16(1), pp.55-69.

Kerle N, van Wyk de Vries B, (2001) The 1998 debris avalanche at Casita volcano, Nicaragua investigation of structural deformation as the cause of slope instability using remote sensing. J Volcanol Geotherm Res 105:49–63

Kelsall, P.C., Watters, R.J. and Franzone, J.G., 1986, June. Engineering characterization of fissured, weathered dolerite and vesicular basalt. In The 27th US Symposium on Rock Mechanics (USRMS). OnePetro.

Kim, M.J. and Lee, H.K., 2016. Internal structure and movement history of the Keumwang fault. *The Journal of the Petrological Society of Korea*, *25*(3), pp.211-230. (DERIVED FROM BIOTITE GRANITE)

Kimura, S., Kaneko, H., Noda, S., Ito, T. and Minagawa, H., 2018. Shear-induced permeability reduction and shear-zone development of sand under high vertical stress. Engineering Geology, 238, pp.86-98.

Kitajima, H., Chester, J.S., Chester, F.M. and Shimamoto, T., 2010. High-speed friction of disaggregated ultracataclasite in rotary shear: Characterization of frictional heating, mechanical behavior, and microstructure evolution. Journal of Geophysical Research: Solid Earth, 115(B8).

Komorowski JC, Glicken HX, Sheridan MF (1991) Secondary electron imagery of microcracks and hackly fracture surfaces in sand-size clasts from the 1980 Mount St. Helens debris-avalanche deposit: implications for particle-particle interactions. Geology 19(3):261–264

Labuz, J.F. and Zang, A., 2012. Mohr–Coulomb failure criterion. *Rock mechanics and rock engineering*, *45*(6), pp.975-979.

Lachenbruch, A.H., 1980. Frictional heating, fluid pressure, and the resistance to fault motion. Journal of Geophysical Research: Solid Earth, 85(B11), pp.6097-6112.

Larue, D.K., Hudleston, P.J., 1987. Foliated breccias in the active Portuguese Bend landslide complex, California: bearing on malange genesis J.Geol.95, 407-422.

Le Corvec N., 2005, Socompa volcano destabilisation (Chile) and fragmentation of debris avalanches. MSc thesis, Université Blaise Pascal, Clermont-Ferrand, France, p 67

Legros F, Cantagrel J-M, Devouard B (2000) Pseudotachylyte (frictionite) at the base of the Arequipa volcanic landslide deposit (Peru): implications for emplacement mechanisms. J Geol 108:601–611. https://doi.org/10.1086/314421

Legros, F., 2002. The mobility of long-runout landslides. Eng. Geol. 63, 301–331. https:// doi.org/10.1016/S0013-7952(01)00090-4

Leroueil, S., 2001. Natural slopes and cuts: movement and failure mechanisms. Géotechnique, 51(3), pp.197-243.

Lucas, A., Mangeney, A. and Ampuero, J.P., 2014. Frictional velocity-weakening in landslides on Earth and on other planetary bodies. Nature communications, 5(1), pp.1-9.

Luhr, J.F., and Prestegaard, K.L., 1988, Caldera formation at Volcán Colima, Mexico, by a large Hoiocene volcanic debris avalanche: Journal of Volcanology and Geothermal Research, v. 35, p. 335-348.

Ma, S., Shimamoto, T., Yao, L., Togo, T. and Kitajima, H., 2014. A rotary-shear low to high-velocity friction apparatus in Beijing to study rock friction at plate to seismic slip rates. Earthquake Science, 27(5), pp.469-497.

Mair, K. and Marone, C., 1999. Friction of simulated fault gouge for a wide range of velocities and normal stresses. *Journal of Geophysical Research: Solid Earth*, *104*(B12), pp.28899-28914.

Mair, K., Frye, K.M. and Marone, C., 2002. Influence of grain characteristics on the friction of granular shear zones. Journal of Geophysical Research: Solid Earth, 107(B10), pp.ECV-4.

Mair, K. and Abe, S., 2011. Breaking up: comminution mechanisms in sheared simulated fault gouge. Pure and Applied Geophysics, 168(12), pp.2277-2288.Geophys. Res. Solid Earth 118

Marone, C. and Scholz, C.H., 1989. Particle-size distribution and microstructures within simulated fault gouge. *Journal of Structural Geology*, *11*(7), pp.799-814.

Marone, C., Raleigh, C.B. and Scholz, C.H., 1990. Frictional behavior and constitutive modeling of simulated fault gouge. Journal of Geophysical Research: Solid Earth, 95(B5), pp.7007-7025.

Marone, C., 1998. Laboratory-derived friction laws and their application to seismic faulting. Annual Review of Earth and Planetary Sciences, 26(1), pp.643-696.

Minshull, T. A., and J. M. Brozena, 1997,Gravity anomalies and flexure of the lithosphere at Ascension Island, Geophys. J. Int., 131, 347 – 360

Mitchell, N.C., 2003. Susceptibility of mid-ocean ridge volcanic islands and seamounts to large-scale landsliding. Journal of Geophysical Research: Solid Earth, 108(B8).

Montserrat, S., A. Tamburrino, O. Roche, and Y. Niño (2012), Pore fluid pressure diffusion in defluidizing granular columns,J. Geophys. Res.,117, F02034, doi:10.1029/2011JF002164

Moore, J. G., D. A. Clague, R. T. Holcomb, P. W. Lipman, W. R. Normark, and M. E. Torresan, Prodigious submarine landslides on the Hawaiian Ridge, J. 1989, Geophys. Res., 94, 17,465 – 17,484

Morelli, S., Monroy, V.H.G., Gigli, G., Falorni, G., Rocha, E.A. and Casagli, N., 2010. The Tancitaro debris avalanche: characterization, propagation and modeling. Journal of Volcanology and Geothermal Research, 193(1-2), pp.93-105.

Moreno, H. and Fuentealba, G., 1994. The May 17-19 1994 Llaima volcano eruption, southern Andes 38° 42'8-71° 44'W. Andean Geology, 21(1), pp.167-171.

Moreno-Alfonso, S.C., Sánchez, J.J. and Murcia, H., 2021. Evidences of an unknown debris avalanche event (< 0.58 Ma), in the active azufral volcano (Nariño, Colombia). Journal of South American Earth Sciences, 107, p.103138.

Morrow, C.A., Shi, L.Q. and Byerlee, J.D., 1984. Permeability of fault gouge under confining pressure and shear stress. *Journal of Geophysical Research: Solid Earth*, *89*(B5), pp.3193-3200.

Murthy, P.S.K., Singh, S. and Gupta, S.L., 2020. Influence of Texture on Mechanical Behaviour of Basalts. In Advances in Sustainable Construction Materials and Geotechnical Engineering (pp. 249-259). Springer, Singapore.

Naranjo, P. and Mideros, R. eds., 1997. Etnomedicina: progresos ítalo-latinoamericanos: memorias del IV Congreso Italo-Latinoamericano de Etnomedicina" Felice Fontana", Quito, 6-9 de noviembre de 1995 (Vol. 1). Editorial Abya Yala.

Neall VE (1976) Lahars as major geological hazards. Bull Int Assoc Eng Geol 14:233–240

Nielson, D.L. and Sibbett, B.S., 1996. Geology of Ascension Island, South Atlantic Ocean. Geothermics, 25(4-5), pp.427-448.

Norini G, Bustos E, Arnosio M, Baez W, Zuluaga MC, Roverato M (2020) Unusual volcanic instability and sector collapse configuration at Chimpa volcano, central Andes. J Volc Geoth Res 393:106808

Olivares L. and Damiano E. 2007. Postfailure mechanics of landslides: laboratory investigation of flowslides in pyroclastic soils. Journal of Geotechnical and Geoenvironmental Engineering, 133(1): 51–62.

Paguican, E.M., Roverato, M. and Yoshida, H., 2021. Volcanic Debris Avalanche Transport and Emplacement Mechanisms. In Volcanic Debris Avalanches (pp. 143-173). Springer, Cham.

Palmer BA, Alloway BV, Neall VE (1991) Volcanic debris-avalanche deposits in New Zealand—Lithofacies organization in unconfi ned, wet avalanche flows. In: Fisher RV,

Palmer, B.A. and Neall, V.E., 1991. Contrasting lithofacies architecture in ring-plain deposits related to edifice construction and destruction, the Quaternary Stratford

and Opunake Formations, Egmont Volcano, New Zealand. Sedimentary Geology, 74(1-4), pp.71-88.

Pastor, M., Quecedo, M., Gonzalez, E., Herreros, M.I., Merodo, J.A. and Mira, P., 2004. Modelling of landslides:(II) propagation. In Degradations and Instabilities in Geomaterials (pp. 319-367). Springer, Vienna.

Pastor, M., Manzanal, D., Fernandez Merodo, J.A., Mira, P., Blanc, T., Drempetic, V., Pastor, M.J., Haddad, B. and Sanchez, M., 2010. From solids to fluidized soils: diffuse failure mechanisms in geostructures with applications to fast catastrophic landslides. *Granular Matter*, *12*(3), pp.211-228.

Perinotto, H., Schneider, J.L., Bachèlery, P., Le Bourdonnec, F.X., Famin, V. and Michon, L., 2015. The extreme mobility of debris avalanches: A new model of transport mechanism. Journal of Geophysical Research: Solid Earth, 120(12), pp.8110-8119.

Pollet, N. and Schneider, J.L., 2004. Dynamic disintegration processes accompanying transport of the Holocene Flims sturzstrom (Swiss Alps). Earth and Planetary Science Letters, 221(1-4), pp.433-448.

Pozzi, G., De Paola, N., Nielsen, S.B., Holdsworth, R.E., Tesei, T., Thieme, M. and Demouchy, S., 2021. Coseismic fault lubrication by viscous deformation. Nature Geoscience, 14(6), pp.437-442.

Preece, K. Photographs from expedition to Ascension Island.

Preece, K., Mark, D.F., Barclay, J., Cohen, B.E., Chamberlain, K.J., Jowitt, C., Vye-Brown, C., Brown, R.J. and Hamilton, S., 2018. Bridging the gap: 40Ar/39Ar dating of volcanic eruptions from the 'Age of Discovery'. *Geology*, *46*(12), pp.1035-1038.

Preece, K., Barclay, J., Brown, R.J., Chamberlain, K.J. and Mark, D.F., 2021. Explosive felsic eruptions on ocean islands: a case study from Ascension Island (South Atlantic). *Journal of Volcanology and Geothermal Research*, *416*, p.107284.

Procter, J.N., Zernack, A.V. and Cronin, S.J., 2021. Computer simulation of a volcanic debris avalanche from Mt. Taranaki, New Zealand. In *Volcanic Debris Avalanches* (pp. 281-310). Springer, Cham.

Rait, K.L., Bowman, E.T. and Lambert, C., 2012. Dynamic fragmentation of rock clasts under normal compression in sturzstrom. Géotechnique Letters, 2(3), pp.167-172.

Ramsay, J., 1980. Shear zone geometry: a review. Journal of structural geology, 2(1-2), pp.83-99.

Rice, J.R., 2006. Heating and weakening of faults during earthquake slip. Journal of Geophysical Research: Solid Earth, 111(B5).

Robertson, R., 2021. (unpublished) Schematic diagram of low to high velocity rotary shear apparatus, Rock Mechanics lab, Durham University

Roche, O., M. A. Gilbertson, J. C. Phillips, and R. S. J. Sparks (2004), Experimental study of gas-fluidized granular flows with implications forpyroclastic flow emplacement,J. Geophys. Res.,109, B10201, doi:10.1029/2003JB002916.

Roverato M, Capra L (2013) Características microtexturales como indicadores del transporte emplazamiento de dos depósitos de avalancha de escombros del volcán de Colima. Rev Mex Ciencias Geol 30:512–525

Roverato, M., Cronin, S., Procter, J. and Capra, L., 2015. Textural features as indicators of debris avalanche transport and emplacement, Taranaki volcano. Bulletin, 127(1-2), pp.3-18.

Roverato, M., Dufresne, A., and Procter, J., 2021. Volcanic Debris Avalanches: From Collapse to Hazard., Springer.

Rowley, P. J., O. Roche, T. H. Druitt, and R. Cas (2014), Experimental study of dense pyroclastic density currents using sustained, gas-fluidizedgranular flows,Bull. Volcanol.,76(9), 855

Saillet, E. and Wibberley, C.A., 2010. Evolution of cataclastic faulting in high-porosity sandstone, Bassin du Sud-Est, Provence, France. Journal of Structural Geology, 32(11), pp.1590-1608.

Sawai, M., Hirose, T. and Kameda, J., 2014. Frictional properties of incoming pelagic sediments at the Japan Trench: implications for large slip at a shallow plate boundary during the 2011 Tohoku earthquake. *Earth, Planets and Space*, *66*(1), pp.1-8.

Scholz CH, Engelder JT. 1976. The role of asperity indentation and ploughing in rock friction: I. Asperity creep and stick slip. Int. J. Rock Mech. Mining Sci. 13:149–54

Schmitt, S.V., Segall, P. and Matsuzawa, T., 2011. Shear heating-induced thermal pressurization during earthquake nucleation. Journal of Geophysical Research: Solid Earth, 116(B6).

Schneider, J.L. and Fisher, R.V., 1998. Transport and emplacement mechanisms of large volcanic debris avalanches: evidence from the northwest sector of Cantal Volcano (France). Journal of Volcanology and Geothermal Research, 83(1-2), pp.141-165.

Schneider, J.L., Pollet, N., Chapron, E., Wessels, M. and Wassmer, P., 2004. Signature of Rhine Valley sturzstrom dam failures in Holocene sediments of Lake Constance, Germany. Sedimentary Geology, 169(1-2), pp.75-91.

Scholz, C.H., 1998. Earthquakes and friction laws. *Nature*, *391*(6662), pp.37-42.

Scott KM, Macias JL, Vallance JW, Naranjo JA, Rodríguez S, McGeehin JP (2001) Catastrophic Debris flows transformed from landslides in volcanic terrains: mobility, hazard assessment, and mitigating strategies. U.S. Geological Survey Professional Paper 1630, p 59

Scuderi, M.M., Collettini, C., Viti, C., Tinti, E. and Marone, C., 2017. Evolution of shear fabric in granular fault gouge from stable sliding to stick slip and implications for fault slip mode. *Geology*, *45*(8), pp.731-734.

Segall, P., Rubin, A.M., Bradley, A.M. and Rice, J.R., 2010. Dilatant strengthening as a mechanism for slow slip events. Journal of Geophysical Research: Solid Earth, 115(B12).

Shea, T., van Wyk de Vries, B., 2008. Structural analysis and analogue modeling of the kinematics and dynamics of rockslide avalanchesShea and van Wyk de Vries. Geosphere 4, 657–686. https://doi.org/10.1130/GES00131.1.

Shreve, R.L., 1968. The blackhawk landslide. In: Shreve, R.L. (Ed.), The Blackhawk Landslide. Geological Society of America. https://doi.org/10.1130/SPE108-p1

Sibson, R.H., 1973. Interactions between temperature and pore-fluid pressure during earthquake faulting and a mechanism for partial or total stress relief. Nature Physical Science, 243(126), pp.66-68.

Sibson, R.H., 1977. Fault rocks and fault mechanisms. Journal of the Geological Society, 133(3), pp.191-213.

Siebe C, Salinas S, Arana-Salinas L, Macías JL, Gardner J, Bonasia R (2017) The 23,500 yr 14C BP, White Pumice Plinian eruption and associated debris avalanche and Tochimilco lava flow of Popocatépetl volcano, México. J Volcanol Geotherm Res 333– 334:66–95

Siebert L (1984) Large volcanic debris avalanches: Characteristics of source area, deposits, and associated eruptions. J Volcanol Geoth Res 22:163–197

Siebert L, Glicken H, Ui T (1987) Volcanic hazard from Bezymianny and Bandai type eruption. Bull Volcanol 49:435–459

Siebert, L., Cottrell, E., Venzke, E., and Andrews, B., 2015, Earth's volcanoes and their eruptions: An overview, in Sigurdsson, H., ed., The Encyclopedia of Volcanoes, (2nd edition): London, Elsevier, Academic Press, p. 239–255

Sigurdsson, H., Houghton, B., McNutt, S., Rymer, H. and Stix, J. eds., 2015. The encyclopedia of volcanoes. Elsevier.

Smeraglia, L., Bettucci, A., Billi, A., Carminati, E., Cavallo, A., Di Toro, G., Natali, M., Passeri, D., Rossi, M. and Spagnuolo, E., 2017. Microstructural evidence for seismic and aseismic slips along clay-bearing, carbonate faults. Journal of Geophysical Research: Solid Earth, 122(5), pp.3895-3915.

Smith GA (eds) Sedimentation in volcanic settings: society for sedimentary geology (SEPM) special publication, vol 45, pp 89–98

Song, S.J., Choo, C.O., Chang, C.J., Chang, T.W. and Jang, Y.D., 2012. Mineral composition and grain size distribution of fault rock from Yangbuk-myeon, Gyeongju city, Korea. *Economic and Environmental Geology*, *45*(5), pp.487-502.

Sørensen, S.A. and Bauer, B., 2003. On the dynamics of the Köfels sturzstrom. Geomorphology, 54(1-2), pp.11-19.

Sosio, R., Crosta, G.B. and Hungr, O., 2012. Numerical modeling of debris avalanche propagation from collapse of volcanic edifices. *Landslides*, *9*(3), pp.315-334.

Sparks, R. S. J. (1978), Gas release rates from pyroclastic flows: A assessment of the role of fluidisation in their emplacement,Bull. Volcanol.,41(1), 1–9

Strekeisen, A. (2020), Rocks in thin section, available online at ALEX STREKEISEN

Stoopes, G.R. and Sheridan, M.F., 1992. Giant debris avalanches from the Colima Volcanic Complex, Mexico: Implications for long-runout landslides (> 100 km) and hazard assessment. Geology, 20(4), pp.299-302.

Takarada, S., Ui, T. and Yamamoto, Y., 1999. Depositional features and transportation mechanism of valley-filling Iwasegawa and Kaida debris avalanches, Japan. Bulletin of Volcanology, 60, pp.508-522.

Togo, T. and Shimamoto, T., 2012. Energy partition for grain crushing in quartz gouge during subseismic to seismic fault motion: An experimental study. *Journal of Structural Geology*, *38*, pp.139-155.

Tost, M., Cronin, S.J. and Procter, J.N., 2014. Transport and emplacement mechanisms of channelised long-runout debris avalanches, Ruapehu volcano, New Zealand. Bulletin of Volcanology, 76, pp.1-14.

Tullis, J. and Yund, R.A., 1987. Transition from cataclastic flow to dislocation creep of feldspar: Mechanisms and microstructures. Geology, 15(7), pp.606-609.

Ui T (1983) Volcanic dry avalanche deposits: identifications and comparison with nonvolcanic debris stream deposits. J Volcanol Geoth Res 18:135–150

Ui T, Glicken H (1986) Internal structural variations in a debris-avalanche deposit from ancestral Mount Shasta, California, USA. Bull Volcanol 48:189–194. https://doi.org/10.1007/BF01087673

Ui, T., Yamamoto, H., and Suzuki-Kamata, K., 1986, Characterization of debris avalanche deposits in Japan: Journal of Volcanology and Geothermal Research, v. 29, p. 231–243, doi: 10 .1016 /0377 -0273 (86)90046 -6 .

Ui T, Takarada S, Yoshimoto M (2000) Debris avalanches. In: Sigurdsson H, Houghton B, McNutt SR, Rymer H, Stix J (eds) Encyclopaedia of volcanoes. Academic Press, pp 617–626

Unak, P., Budiyo, R.C., Horsnzky, A., Yasakci, V., Pearce, G., Russell, S., Aras, O., Akin, O. and Wong, J., 2021. Effects of fluorodeoxyglucose magnetic nanoparticles on NCIH727 and SH-SY5Y cancer cells. Asian Journal of Nanoscience and Materials, 4, pp.53-66.

Underhill, J.R. and Woodcock, N.H., 1987. Faulting mechanisms in high-porosity sandstones; new red sandstone, Arran, Scotland. Geological Society, London, Special Publications, 29(1), pp.91-105.

Vallance, J.W., Siebert, L., Rose Jr, W.I., Girón, J.R. and Banks, N.G., 1995. Edifice collapse and related hazards in Guatemala. Journal of Volcanology and Geothermal Research, 66(1-4), pp.337-355.

Vallance JW, Scott KM (1997) The Osceola mudfl ow from Mount Rainier: Sedimentology and hazard implication of a huge clay-rich debris flow. GSA Bull 109:143–163

Valverde, J.M. and Soria-Hoyo, C., 2015. Vibration-induced dynamical weakening of pyroclastic flows: Insights from rotating drum experiments. Journal of Geophysical Research: Solid Earth, 120(9), pp.6182-6190.

Varnes, D. J., 1978 Slope movement types and processes, in Landslides, Analysis and Control, Spec. Rep. 176, edited by R. L. Schuster and R. J. Krizek, pp. 11 – 33, Natl. Acad. of Sci., Washington, D. C.,

van Wyk de Vries B, Self S, Francis PW, Keszthelyi L (2001) A gravitational spreading origin for the Socompa debris avalanche. J Volcanol Geotherm Res 105:225–247

van Wyk De Vries, B.V.W. and Delcamp, A., 2015. Volcanic debris avalanches. In *Landslide hazards, risks, and disasters* (pp. 131-157). Academic Press.

van Wyk de Vries B, Davies T (2015) Landslides, debris avalanches, and volcanic gravitational deformation. In: The encyclopedia of volcanoes. Academic Press, pp 665–685

Venzke, E., ed., 2013, Volcanoes of the World, v. 4.5.0: Washington, D.C., Smithsonian Institution Global Volcanism Program, https:// doi .org /10 .5479 /si.GVP .VOTW4 - 2013

Verberne, B.A., Niemeijer, A.R., De Bresser, J.H. and Spiers, C.J., 2015. Mechanical behavior and microstructure of simulated calcite fault gouge sheared at 20–600 C: Implications for natural faults in limestones. *Journal of Geophysical Research: Solid Earth*, *120*(12), pp.8169-8196.

Verberne, B.A., Plümper, O. and Spiers, C.J., 2019. Nanocrystalline principal slip zones and their role in controlling crustal fault rheology. *Minerals*, *9*(6), p.328.

Voight, B., Janda, R.J., Glicken, H. and Douglass, P.M., 1985. Discussion: nature and mechanics of the Mount St Helens rockslide-avalanche of 18 May 1980. Geotechnique, 35(3), pp.357-368.

Voight, B., 2000. Structural stability of andesite volcanoes and lava domes. Phil. Trans. Roy. Soc. Lond. 358, 1663–1703.

Wadge, G., Francis, P.W. and Ramirez, C.F., 1995. The Socompa collapse and avalanche event. Journal of Volcanology and Geothermal Research, 66(1-4), pp.309-336.

Waitt, R.B. (2013). Lahar. In: Bobrowsky, P.T. (eds) Encyclopedia of Natural Hazards. Encyclopedia of Earth Sciences Series. Springer, Dordrecht. https://doi.org/10.1007/978-1-4020-4399-4_206

Wang F.W., Sassa K., and Wang G. 2002. Mechanism of a long-runout landslide triggered by the August 1998 heavy rainfall in Fukushima Prefecture, Japan. Engineering Geology, 63: 169–185.

Wang G. and Sassa K. 2001. Factors affecting rainfall-induced landslides in laboratory flume tests. Géotechnique, 51: 587–600.

Wang, G., Suemine, A. and Schulz, W.H., 2010. Shear-rate-dependent strength control on the dynamics of rainfall-triggered landslides, Tokushima Prefecture, Japan. Earth Surface Processes and Landforms, 35(4), pp.407-416.

Wang, Y.F., Dong, J.J. and Cheng, Q.G., 2017. Velocity-dependent frictional weakening of large rock avalanche basal facies: Implications for rock avalanche hypermobility?. Journal of Geophysical Research: Solid Earth, 122(3), pp.1648-1676.

Ward, S.N. and Day, S., 2006. Particulate kinematic simulations of debris avalanches: interpretation of deposits and landslide seismic signals of Mount Saint Helens, 1980 May 18. Geophysical Journal International, 167(2), pp.991-1004.

Weaver, B., Kar, A., Davidson, J. and Colucci, M., 1996. Geochemical characteristics of volcanic rocks from Ascension Island, south Atlantic Ocean. *Geothermics*, *25*(4-5), pp.449-470.

Wibberley, C.A. and Shimamoto, T., 2005. Earthquake slip weakening and asperities explained by thermal pressurization. Nature, 436(7051), pp.689-692.

Woodcock, N.H. and Mort, K., 2008. Classification of fault breccias and related fault rocks. *Geological Magazine*, *145*(3), pp.435-440.

Yoshida, H., Sugai, T. and Ohmori, H., 2012. Size–distance relationships for hummocks on volcanic rockslide-debris avalanche deposits in Japan. Geomorphology, 136(1), pp.76-87.

Yao, L., Ma, S., Platt, J.D., Niemeijer, A.R. and Shimamoto, T., 2016. The crucial role of temperature in high-velocity weakening of faults: Experiments on gouge using host blocks with different thermal conductivities. Geology, 44(1), pp.63-66.

Yehle, L.A. and Nichols, D.R., 1980. Reconnaissance map and description of the Chetaslina volcanic debris flow (new name), southeastern Copper River basin and adjacent areas, south-central Alaska (No. 1209).

Zernack, A.V., Procter, J.N., and Cronin, S.J., 2009, Sedimentary signatures of cyclic growth and destruction of stratovolcanoes: A case study from Mt. Taranaki, NZ: Sedimentary Geology, v. 220, p. 288–305, doi: 10 .1016 /j .sedgeo .2009 .04 .024

Zhang, M. and McSaveney, M.J., 2017. Rock avalanche deposits store quantitative evidence on internal shear during runout. Geophysical Research Letters, 44(17), pp.8814-8821.